Forschungszentrum Karlsruhe
in der Helmholtz-Gemeinschaft

Wissenschaftliche Berichte
FZKA 6947
SAM-COLOSS-P074

Simultaneous Dissolution of UO_2 and ZrO_2 by Molten Zircaloy New Experiments and Modelling

K. Müller, A.V. Goryachev, V.P. Smirnov, A.M. Svyatkin, J. Stuckert, M.S. Veshchunov, A.V. Berdyshev

Institut für Materialforschung
Programm Nukleare Sicherheitsforschung

Januar 2004

Impressum der Print-Ausgabe:

Als Manuskript gedruckt

Forschungszentrum Karlsruhe GmbH
Postfach 3640, 76021 Karlsruhe

Mitglied der Hermann von Helmholtz-Gemeinschaft
Deutscher Forschungszentren (HGF)

ISSN 0947-8620

Forschungszentrum Karlsruhe
in der Helmholtz-Gemeinschaft

Wissenschaftliche Berichte
FZKA 6947
SAM-COLOSS-P074

Simultaneous Dissolution of UO_2 and ZrO_2 by Molten Zircaloy New Experiments and Modelling

K. Müller [a], A.V. Goryachev [b], V.P. Smirnov [b], A.M. Svyatkin [b], J. Stuckert, M.S. Veshchunov [c], A.V. Berdyshev [c]

Institut für Materialforschung
Programm Nukleare Sicherheitsforschung

[a] JRC/IE, Joint Research Centre, Institute for Energy, Petten, The Netherlands
[b] RIAR, State Scientific Centre, Research Institute of Atomic Reactors Dimitrovgrad, Russian Federation
[c] IBRAE, Nuclear Safety Institute, Russian Academy of Sciences, Moscow, Russian Federation

Forschungszentrum Karlsruhe GmbH, Karlsruhe
2004

Impressum der Print-Ausgabe:

Als Manuskript gedruckt

Forschungszentrum Karlsruhe GmbH
Postfach 3640, 76021 Karlsruhe

Mitglied der Hermann von Helmholtz-Gemeinschaft
Deutscher Forschungszentren (HGF)

ISSN 0947-8620

Abstract

This report summarises the Tasks WP2.1 and WP7.3 of the COLOSS Project (Core Loss during Severe Accident) within the 5th Framework Programme of EU. The experimental Task WP2.1 was performed during 2000-2002 at the RIAR (Dimitrovgrad, Russia) in collaboration with Forschungszentrum Karlsruhe. Whereas RIAR acted as a subcontractor to JRC/IE (Joint Research Centre, Petten). The analytical Task WP7.3 was performed at the Nuclear Safety Institute (IBRAE) of Russian Academy of Sciences (RAS), with IBRAE acting as a subcontractor to JRC.

The main objective of the Task WP2.1 was to extend the experimental work packages on dissolution of UO_2 and ZrO_2 by molten Zry, started within the framework of the CIT Project (4th FP of EU) at Forschungszentrum Karlsruhe and AECL (Canada). The main objective of the Task WP7.3 was to develop a model for the code SVECHA (mechanistic code to study a single rod behaviour) for analytical treatment of these phenomena.

Final interpretation of the experimental results was performed jointly by JRC Petten, Forschungszentrum Karlsruhe, RIAR Dimitrovgrad and IBRAE Moscow.

Simultanauflösung von UO_2 und ZrO_2 durch geschmolzenes Zirkaloy. Neue Experimente und Modellieren

Zusammenfassung

Dieser Bericht fasst die Aufgaben WP2.1 und WP7.3 des Projektes COLOSS (Core Loss during Severe Accident, 5. Rahmenprogramm der EU) zusammen. Die experimentelle Aufgabe WP2.1 wurde während der Zeitperiode 2000-2002 am RIAR (Dimitrovgrad, Russland) in Zusammenarbeit mit dem Forschungszentrum Karlsruhe durchgeführt. RIAR trat dabei als Unterauftragnehmer von JRC/IE (Joint Research Centre, Petten) auf. Die analytische Aufgabe WP7.3 wurde am Institut für Reaktorsicherheit (IBRAE) der russischen Akademie der Wissenschaft durchgeführt. Dabei diente IBRAE als Unterauftragnehmer von JRC.

Die Hauptzielsetzung der Aufgabe WP2.1 war, die experimentellen Arbeiten zur Untersuchung der Auflösung von UO_2 und ZrO_2 durch geschmolzenes Zirkaloy fortzusetzen, die im Rahmen des 4. Rahmenprogramms der EU im Forschungszentrum Karlsruhe und bei AECL (Kanada) begonnen wurden. Die Hauptzielsetzung der Aufgabe WP7.3 war, ein Modell für den Code SVECHA (mechanistischer Code zur Simulation von Abschreckversuchen) für eine analytische Beschreibung dieser Phänomene zu entwickeln.

Die abschließende Interpretierung der experimentellen Ergebnisse wurde gemeinsam von JRC Petten, Forschungszentrum Karlsruhe, RIAR Dimitrovgrad und IBRAE Moscow durchgeführt.

Content

List of Tables

List of Figures

Part I. Results of crucible tests on simultaneous dissolution of UO_2 and ZrO_2 by molten Zry

1. Introduction

This report summarizes the experimental part of work package WP2.1 of the Core Loss during Severe Accident program which was performed by RIAR (Dimitrovgrad, Russia) in collaboration with FZK (Karlsruhe), with RIAR acting as a subcontractor to JRC/IE.

The objective of the work package WP2.1 was to extend the experimental works on study of UO_2 and ZrO_2 dissolution by molten Zry, started in the framework of the CIT program at FZK and AECL [1] .

The results obtained in previous tests allowed estimation of the kinetics of UO_2 and ZrO_2 dissolution as separate processes. However, the first scooping tests on the simultaneous dissolution of UO_2 and ZrO_2 by molten Zry carried out at 2100 ^{0}C have shown, that the kinetics of a simultaneous dissolution could not be treated as a simple superposition of the UO_2 - Zry and ZrO_2 - Zry dissolution processes.

To resolve this problem and extend the existing experimental data base, the additional experiments on simultaneous dissolution UO_2 and ZrO_2 by molten Zry were planned within the framework of the COLOSS project. Altogether 12 tests were planned at temperatures of 2100 and 2200 ^{0}C. Two of these tests should be calibrating ones, in order to establish the consistency of experimental conditions and results with the earlier tests on separate UO_2 dissolution [1].

The analysis of results and the analytical support of experiments were carried out by IBRAE.

After realization of the first series of experiments at 2100 °C according to the initial plan, the test matrix was changed, because at test temperature 2200 ^{0}C and holding times ~ 200 s the through-wall penetration of the crucibles by the melt occurred.

Another task of the second test series was a more precise definition of the temperature conditions of the tests, in particular, checking of potential influence of the temperature difference between the walls of uranium crucible and the melt on the dissolution rate. For this purpose the heat insulation of the crucibles by a zirconia fiber material was used that has allowed to exclude a temperature gradient occurring due to thermal radiation from the melt surface. The revised test matrix is given in Table 1.

This report describes procedure and results of the executed tests and also gives the description of methods used for examination of the samples.

2. Experimental

2.1. Materials

The UO_2 crucibles (Fig. I - 1) used for the tests were made by pressing and sintering of fine uranium dioxide powder. The ~5 mm deep holes in the crucible bottom for installation of the central ZrO_2 rods were drilled by a diamond borer. The geometrical density of the crucibles was 10.1 g/cm³.

The Ca-stabilized ZrO_2 rods (with density of 5.3 g/cm³) and the 2.2-mm thick Y_2O_3 disks used for the crucible bottom insulation were supplied by FZK. In the tests that have been carried out at 2100 °C, the ZrO_2 rods with diameter of 7.4 mm were used. In the tests at 2200 °C the ZrO_2 rods with diameter of 8.4 mm were used. The content of Ca in the rod material was 2.7 wt%. A Zry-4 rings were produced from a bar supplied by FZK (chemical composition in wt%: 98% of Zr, 1.525% of Sn, 0.221% of Fe, 0.105% of Cr, 0.14% of O).

Before testing, dimensions and weights of all used specimens were measured. The dimensions of Zry charge were selected, so that in calibrating tests the UO_2/Zry weight ratio was 11.8, in the tests at 2100 °C was 13.0 and at 2200 °C was 18.0. The data on weight and dimensions of the used components are listed in Table 2 - Table 4.

2.2. Test rig

The schematic diagram of the test rig is shown in Fig. I - 1 and Fig. I - 2.

Specimens were located in the central part of the resistance furnace on the tungsten support. Temperature of a specimen during the test was measured by two thermocouples installed at 1 mm depth in the crucible sidewall and by two-beam pyrometers focused on the surface of Zry charge. Recording of thermocouples and pyrometer indications during the test was provided by the computer based data acquisition system with an interval 0.5 s. To maintain the given heating/cooling rate and stable temperature at isothermal stage of the test, the feedback between the pyrometer indications and regulating voltage on the furnace heater was used.

Before the test, the furnace was evacuated to pressure of 10^{-4} Pa. After specimen was slowly heated at rate of about 1 K /s up to temperature of 1700 °C (according to the pyrometer indications), the furnace was filled with pure argon. For exclusion of air leakage the tests were carried out at argon pressure slightly above (by 0.03 MPa) the atmospheric one. After equalization of specimen temperature during 30 min it was heated up to given temperature at rate of about 6 K/s. Specimen cooling (after holding at test temperature) was carried out in two stages: fast cooling down to temperature of 1500 °C and slow cooling during 1.5 h down to room temperature.

Prior to the beginning of the planned test series, two special tests on measurement of temperature gradient along the UO_2 crucible sidewall and comparison of the thermocouples and pyrometer indications were carried out. For the measurement of temperature gradient along the crucible sidewall 6 holes at 1mm depth with a step of 4 mm were drilled along the outer sidewall surface.

The indications of two thermocouples installed in various holes were compared. In all the cases discrepancy in the thermocouple indications did not exceed 1% that testified uniform heating of the crucible surface during the test (Fig. I - 3).

The second test was carried out for comparison of the thermocouple and pyrometer temperature readings. In this test pyrometer was focused on the tungsten ingot

located at the crucible bottom. Simultaneously temperature of the ingot was tested by thermocouple installed in the hole in the center of the ingot. The scheme of this test is shown in Fig. I - 4. Discrepancy of the thermocouple and pyrometer indications was within the limits of an instrumental error and did not exceed 1.5%.

2.3. Sample preparation

After the test an external diameter and a height of each crucible were measured, then the crucibles were cut along its cylinder-axis by a diamond disk.

One half of a specimen was used further for optical microscopy. Samples for the chemical analysis of the uranium, zirconium and oxygen contents in the melt were cut out from the second half. The scheme of specimen sectioning for the chemical analysis is shown in Fig. I - 5.

Crucible bottom and sidewall edges above the level of the melt were cut out by the diamond disk. After that sidewall remnants and central zirconia rod were separated by cuts parallel to the crucible cylinder-axis. Three cut out slices of the melt represented a sample used further for the chemical analysis.

2.4. Chemical analysis

The samples for the chemical analysis were weighed and calcinated in the platinum crucible in air at temperature of 800 – 1000 ^{o}C till the termination of weight increase. In the course of this calcination process all metallic components of the melt form stochiometric oxides: U_3O_8, ZrO_2, Fe_2O_3, CaO, Y_2O_3, SnO_2, Cr_2O_3. After calcination the produced oxides were weighed and carefully mixed up. A part of this mixture of about 100 mg was sampled for definition of the Fe, Ca, Y, Sn contents by spectrographic analysis. The rest of the oxide mixture was weighed and filled with 8 mol/l nitric acid for dissolution of U_3O_8. The oxides Fe_2O_3, CaO, Y_2O_3. ZrO_2, SnO_2 and Cr_2O_3 appeared as sediment after dissolution. The sediment was dried and weighted.

The content of components in the oxide mixture was calculated as follows:

$$M_{U3O8} = M_1 - M_2 - M_{Fe2O3,\,CaO,\,Y2O3};$$
$$M_U = 0.848\, M_{U3O8} = 0.848\, (M_1 - M_2 - M_{Fe2O3,\,CaO,\,Y2O3});$$
$$M_{ZrO2} = M_2 - M_{SnO2,\,Cr2O3};$$
$$M_{Zr} = 0.740\, (M_2 - M_{Fe2O3,\,CaO,\,Y2O3});$$
$$M_O = M_{sample} - M_U - M_{Zr} - M_{Fe,\,Ca,\,Y,\,Sn,\,Cr},$$

where M_{sample} is weight of the sample used for the analysis;
M_1 – weight of the sample after oxidation in air;
M_2 – weight of the sediment.

2.5. Image analysis

For definition of the dissolved volumes of the crucible wall and central rod by the quantitative image analysis method, photographs of longitudinal sections of samples were used. The scheme of measurements is shown in Fig. I - 6.

Dissolved volume of a crucible was calculated, as the half-sum of volumes V_1 and V_2 of two revolution bodies formed by the rotation of the dissolved sidewall areas at longitudinal sections around the crucible axis:

$$V = v \cdot \pi \cdot \sum_i r_i\,, \qquad (1)$$

where v is the volume of one pixel; i numerates pixels in the dissolved sidewall areas; r_i is a pixel distance from the element to the rotation axis..

Dissolved volume of the zirconia rod was calculated as a difference of volumes of the initial rod and its remnants.

Volume of each rod fragment was calculated, as average volume of the body of revolution formed by rotation of the remnant image around its axis according to the above-described algorithm.

Weight of each element dissolved from crucible and central rod was calculated as:

$$M_{1,2} = V_{1,2} \cdot \rho_{1,2} \ , \qquad (2)$$

where $V_{1,2}$ is the dissolved volume of crucible and central rod, $\rho_1 = 10.1$ g/cm³ - density of the UO_2-crucible, $\rho_2 =$ 5.33 g/cm³ - density of the central ZrO_2-rod.

Weight of the melt was calculated as the sum of weights of initial Zircaloy charge and weights of dissolved elements.

3. Results of the first test series

3.1. Tests conditions

The main test parameters for the both test series are listed in Table 5. In Fig. I - 7 - Fig. I - 16 appearance and cross-sections of the tested specimens are shown along with corresponding time/temperature traces. A point on the time/temperature trace that exhibited a thermal arrest was considered as commencement of the Zircaloy melt. However this temperature in all tests was higher than Zircaloy melting point (1760 ^{o}C) that may be attributed to the temperature lag across the charge. This effect is similar to the one obtained in AECL experiments [1]. “Total time molten” was calculated as time from the temperature arrest point to the beginning of the rapid cooling. Such form of representation is convenient for comparison of the obtained results with ones received earlier.

In all the tests some discrepancy of sample temperature measured by pyrometer and thermocouples was observed. At the heat up stage this discrepancy attains ~ 100 ^{o}C.

The higher temperature readings of the thermocouples at the crucible sidewall were explained by a temperature gradient caused by thermal radiation from the melt surface.

In calibrating test at 2200 ^{o}C and holding time of 600 s as well in the simultaneous dissolution test at 2200 ^{o}C and holding time of 260 s, melt penetration in the crucible sidewall was detected. In other tests such penetration was not observed.

3.2. Melt structure

Examination of the melt structure was carried out, in order to estimate the crucible sidewall and central rod dissolution and to reveal possible concentration gradients of melt components along the crucible radius.

The images of melt structures are shown in Fig. I - 17 - Fig. I - 32. The melt has dendritic structure with uniform distribution of phases in the bulk of the formed ingot. The melt is separated from the crucible walls by cracks formed as a result of thermal shrinkage of the melt at cooling. Contraction cavities are observed mainly in the

center of the ingot bottom part at position of the dissolved zirconia rod. As a whole, the structure of the formed melt is similar to the structure observed in the earlier tests.

For estimation of uniformity of uranium and zirconium distribution in the melt bulk, scanning of the specimen cross-sections across the melt using WDX analyzer was carried out. The distribution of uranium and zirconium concentration across the specimens is shown in Fig. I - 33 - Fig. I - 40.

4. The second series of tests

After execution of the first test series, the test matrix was changed. The basic reasons for modification of the planned program of experiments were the following:

- The planned series of tests at temperatures of 2200 ^{o}C and times longer than 200 s could not be carried out owing to the through-wall penetration of the crucible walls by the melt.

- It was necessary to test out a real value of the temperature gradient between the crucible wall and the melt. In particular, the discrepancy of the measured and calculated data on the dissolved material in a number of the carried out experiments was preliminary explained by existence of such a temperature gradient.

For estimation of influence of temperature gradient across the specimen on the dissolution rate, the crucibles in this series were additionally insulated by zirconia fiber plates mounted on the crucible top. Heat insulation allows reduction of heat losses due to radiation from the melt surface and suppression of a temperature gradient between the crucible wall and the melt caused by this phenomenon.

The melt temperature was evaluated by the thermocouple deepened in the crucible wall. In order to reduce a risk of a contact between the thermocouple and the melt, the inlet for the "deep" thermocouple was drilled at a level of the yttria disk, where according to the previous test observations, the dissolution of the crucible wall was minimal. The second thermocouple was placed on the external crucible wall surface, which provided an opportunity to estimate the temperature gradient in the wall during experiment (Fig. I - 41, Fig. I - 42).

For estimation of the heat insulation influence on the temperature gradient, an additional experiment without heat insulation with measurement of the melt temperature by the "deep" thermocouple and pyrometer was carried out (Fig. I - 43).

4.1. Results of second series of tests

The main test parameters and results are listed in Table 5 - Table 7. The post-test examination procedures in this series were perfectly the same as in the previous one, and include:

- Post-test specimens appearance control (Fig. I - 42- Fig. I - 46)
- Metallography of cross-sections (Fig. I - 47 - Fig. I - 56).

- Measurement of uranium and zirconium concentration distribution across the specimens (Fig. I - 57 - Fig. I - 61).

5. Discussion

5.1. Temperature measurements

From the results of the second test series one can see that the difference in indications of the thermocouples installed on the crucible wall surface and near to the melt disappears approximately within first hundred seconds of isothermal stage of the test, irrespective to whether the thermal isolation is installed or not.

These observations result in a conclusion that the temperature gradient across the specimen is small during experiment and difference of the temperatures measured by the pyrometer and thermocouples is a consequence of the non-excluded systematic error. In some tests the divergence between the thermocouple and pyrometer indications exceeds the total instrumental error, which is estimated as 50 K for the pyrometer, and 25 K for thermocouples.

A possible source of the error in the pyrometer measurements may be variation of the melt composition and formation of particles of the second phase during experiment, leading to alteration of the melt reflectance. Another possible reason for the error may be heating of the crucible wall in the area of pyrometer vision (in the case of its displacement during the tests) as well as the influence of the top part of the central rod (if it falls down into the melt). Hence, the uncertainty in the pyrometer temperature measurement in some cases can exceed 100 ^{o}C.

An additional systematic error in the temperature measured by thermocouples may be caused by their various thermal contacts with the crucible walls, and also by thermal conductivity of the thermocouple shroud. The systematic error caused by these reasons should result in overestimation of temperatures measured by the thermocouples. However, a good coincidence of temperatures measured by two thermocouples in all the tests and the lack of a considerable temperature gradient across the crucible sidewall allows a conclusion that the temperatures measured by the thermocouples are more reliable and, therefore, should be used in the analysis of experimental results (rather than the pyrometer readings).

5.2. Measurements of dissolved materials

In Table 8 and Table 9 a comparison of the values obtained by the methods of chemical analysis and quantitative image analysis is shown. As a whole, the results of the two independent methods show a good coincidence. However, local divergence of the results can exceed errors of these methods.

In the case of image analysis method the main source of error is associated with the procedure of dissolved volume reconstruction using the cross-section image. In the case of asymmetrical shape of the dissolved volumes, the algorithm used for the volume reconstruction may lead to a substantial error. Besides, in case of significant dissolution of the central rod, undissolved remnants of this rod observed in the melt complicate image analysis.

On the other hand, sample cuts for the chemical analysis rather well represent the mean melt bulk composition. The SEM provided additional control of element distributions across the melt for each sample. The obtained diagrams reflect a relative distribution of these elements and allow a conclusion about the lack of the

uranium and zirconium concentration gradients in the melt. Zones of the sharp change of the uranium and zirconium concentration adjoined to the crucible walls and central zirconia rod are small in thickness (~ 70 μm). Therefore, the loss of these layers during sampling does not result in an essential error in definition of average value of element content in the melt.

6. Conclusions

Two series of crucible experiments on simultaneous dissolution of UO_2 and ZrO_2 by molten Zry at 2100 and 2200 °C have been carried out successfully. The UO_2 crucibles with ZrO_2 cylinder installed in the crucible centre with Zry charge were used in the tests. The kinetics of the material interactions in the tests with duration of isothermal annealing at target temperatures from 100 to 600 s was measured.

Lack of a considerable temperature gradient across the crucible wall during annealing stage of the tests has been revealed by implementation of a thermocouple deepened in the crucible sidewall (in addition to the surface thermocouple). Possible error sources in the pyrometer measurements were reconciled. This allows a conclusion that the surface thermocouple data fairly determine temperature conditions of melt in both (1^{st} and 2^{nd}) test series and should be used in analysis of the test measurements.

The frozen melts in each specimen contained three major phases: a dendritic ceramic $(U,Zr)O_{2-x}$ phase with a zoned microstructure, a Zr(O) alloy matrix phase that also occurred as inclusions between the ceramic zones, and a U(O) phase that occurred in low concentrations as inclusions in the ceramic and Zr(O)-matrix phases.

The WDX and phase-area analyses showed no statistically significant variation in the phase compositions or distributions at different locations within each specimen, indicating that the melts were reasonably homogeneous at the test temperature before cooling. This confirms strong convective stirring of the melt in the tests and enhances accuracy of the chemical analysis of the melt mean composition.

The results of melt composition measurement by two different methods of the quantitative image analysis and chemical analysis are in good correspondence. This confirms validity of the quantitative image analysis method, which allows independent determination of dissolution kinetics of each solid material (UO_2 and ZrO_2) during their simultaneous interactions with molten Zry. These data allow development and thorough validation of a new analytical model.

Acknowledgements

The experimental and theoretical works described in this report was co-financed by the European Comission under the EURATOM 5^{th} Framework Programme on Nuclear Fission safety 1998-2002.

The authors thank Mrs. E. Zvir for the conduct of the image analysis, Mr. V. Yakovlev for the conduct of the SEM/WDX analysis, Mr. V. Mishenev and Mr. Tikhomirov for the conduct of the chemical analysis.

Table 1. Test matrix

Test temperature [°C]	2100						2100			
Holding time [s]	600 (c)	100	200	300	400	500	600 (c, t)	200 (d)	200 (t)	400 (t)
Test temperature [°C]	2200						2200			
Holding time [s]	600 (c)		100	180	260		180 (t)			

c – calibrating test (without central rod)
t - test with heat-insulated crucible
d – melt temperature control by “deep” thermocouple.

Table 2. Initial parameters of the Zry charge

Test	Zry charge			
	Outer diameter, mm	Inner diameter, mm	Height, mm	Weight, g
2100_600 (calibrating)	11.80	-	14.30	10.03
2100_100	16.50	7.50	8.20	8.91
2100_200	16.52	7.48	8.21	8.91
2100_300	16.49	7.51	8.20	8.91
2100_400	16.52	7.49	8.22	8.93
2100_500	16.50	7.50	8.20	8.91
2200_600 (calibrating)	11.82	-	14.28	10.04
2200_100	16.45	8.50	6.35	6.41
2200_180	16.50	8.50	6.33	6.43
2200_260	16.46	8.50	6.36	6.41
2100_600 (calibrating) heat-insulation	11.70	-	14.26	9.91
2100_200 “deep” thermocouple	16.49	7.46	8.20	8.99
2100_200 heat-insulation	16.48	7.48	8.22	9.05
2100_400 heat-insulation	16.49	7.49	8.22	9.04
2200_180 heat-insulation	16.50	8.50	6.36	6.45

Table 3. Initial parameters of UO_2-crucibles

Test	Nr.	UO_2 crucible (Fig.1)					
		D, mm	d, mm	H, mm	h, mm	Weight, g	M(UO_2)/M(Zry)
2100_600(calibrating)	1	26.47	16.48	27.78	16.48	118.46	11.8
2100_100	3	26.48	16.47	27.75	16.49	115.61	13.0
2100_200	4	26.46	16.49	27.76	16.48	115.94	13.0
2100_300	5	26.49	16.50	27.77	16.47	116.17	13.0
2100_400	6	26.45	16.46	27.76	16.49	115.88	13.0
2100_500	15	26.45	16.42	27.76	16.49	115.91	13.0
2200_600(calibrating)	2	26.49	16.52	27.76	16.53	118.44	11.8
2200_100	11	26.50	16.58	27.78	16.45	115.64	18.1
2200_180	16	26.49	16.48	27.74	16.45	115.04	17.9
2200_260	14	26.52	16.51	27.78	16.51	116.16	18.1
2100_600(calibrating) heat-insulation	18	26.49	16.48	27.75	16.55	118.48	12.0
2100_200 “deep” thermocouple	17	26.44	16.48	27.75	16.43	115.26	12.8
2100_200 heat-insulation	20	26.49	16.48	27.76	16.52	115.83	12.8
2100_400 heat-insulation	19	26.50	16.49	27.74	16.47	115.94	12.8
2200_180 heat-insulation	13	26.47	16.49	27.78	16.50	114.47	17.7

Table 4. Initial parameters of ZrO_2-rods

Test	ZrO_2 rod			
	Diameter, mm	Height, mm	Volume, mm^3	Weight, g
2100_100	7.38	23.01	984.28	5.23
2100_200	7.41	23.00	991.87	5.26
2100_300	7.39	22.99	986.09	5.25
2100_400	7.40	22.99	988.76	5.29
2100_500	7.40	23.00	989.19	5.21
2200_100	8.41	23.05	1280.42	6.79
2200_180	8.36	23.01	1263.05	6.74
2200_260	8.41	23.02	1278.75	6.78
2100_200 “deep” TC	7.40	23.01	989.62	5.29
2100_200 heat-insulation	7.40	22.99	988.76	5.27
2100_400 heat-insulation	7.40	23.00	989.19	5.31
2200_180 heat-insulation	8.39	23.04	1273.79	6.85

Table 5. Test parameters

Test	Effective melting temperature °C	Heating rate °C/s	Time in a liquid state s	Duration of isothermal stage s	Temperature at isothermal stage(°C)±2SD		
					Pyrometer	TC1	TC2*
2100_600(calibrating)	1920	9.4	616	591	2057±26	2080±23	2079±20
2100_100	1940	6.5	139	101	2096±27	2189±25	2184±23
2100_200	1908	3.6	250	200	2096±37	2200±55	2195±53
2100_300	1942	8.3	328	303	2107±27	2191±93	2187±89
2100_400	1965	6.8	434	396	2109±15	2180±30	2177±30
2100_500	1982	6.5	539	521	2101±29	2163±49	-
2200_600(calibrating)	1901	4.7	659	579	2206±31	-	-
2200_100	1986	7.9	156	108	2215±20	2245±6	-
2200_180	1994	9.3	245	185	2215±22	2263±9	2259±9
2200_260	1994	5.7	317	287	2203±46	2305±51	-
2100_600(calibrating) heat-insulation	-	6.3	-	620	-	2105±11	2103±3
2100_200 "deep" thermocouple	1955	4.6	258	217	2103±11	2163±30	2153±17
2100_200 heat-insulation	-	6.4	-	209	-	2120±35	2111±17
2100_400 heat-insulation	-	6.1	-	410	-	2120±24	2112±10
2200_180 heat-insulation	-	4.9	-	168	-	2212±16	2203±6

* - "deep" TC (second series of tests)

Table 6. Results of the chemical analysis

Test	Element content in the melt, wt %							
	Zr	U	O	Fe	Cr	Sn	Ca	Y
2100_600(calibrating)	58.91	32.13	7.36	0.24	0.07	1.12	0.05	0.12
2100_100	47.83	42.08	8.63	0.18	0.06	0.95	0.18	0.09
2100_200	38.57	48.79	11.54	0.08	0.04	0.55	0.33	0.10
2100_300	35.77	50.90	12.32	0.09	0.09	0.44	0.22	0.17
2100_400	44.07	43.74	11.52	0.03	0.002	0.34	0.06	0.22
2100_500	45.43	42.63	10.49	0.11	0.09	0.45	0.23	0.57
2200_100	50.72	37.62	10.63	0.11	0.06	0.63	0.11	0.12
2200_180	27.82	59.32	12.31	0.03	0.002	0.23	0.16	0.11
2100_600(calibrating) heat-insulation	58.00	33.48	7.64	0.13	0.07	0.48	0.06	0.14
2100_200 "deep" thermocouple	46.56	42.90	9.58	0.09	0.06	0.46	0.17	0.18
2100_200 heat-insulation	60.50	31.14	7.50	0.12	0.06	0.48	≤0.06	0.14
2100_400 heat-insulation	53.53	36.26	9.18	0.14	0.08	0.58	≤0.06	0.17
2200_180 heat-insulation	40.36	47.37	10.95	0.14	0.06	0.56	0.34	0.22

Table 7. Element content in the melt calculated using the image analysis data

Test	V_t, mm^3	M_U, g	$M^t_{O_2}$ g	V_c, mm^3	M^c_{Zr} g	$M^c_{O_2}$ g	M^c_{Ca} g	ΣM_p g	Element content in the melt, wt %						
									U	Zr	O	Fe	Cr	Sn	Ca
2100_600(calibrating)	713.88	6.32	0.85	-	-	-	-	17.2	36.7	57.3	4.9	0.12	0.06	0.85	-
2100_100	1039.64	9.22	1.24	154.3	0.6	0.2	0.025	20.2	45.7	46.2	7.2	0.09	0.04	0.64	0.12
2100_200	1740.07	15.47	2.08	656.6	2.5	0.9	0.104	29.9	51.7	37.5	10.0	0.06	0.03	0.43	0.35
2100_300	1866.59	16.55	2.23	537.5	2.0	0.7	0.086	30.6	54.2	35.3	9.7	0.06	0.03	0.42	0.28
2100_400	1179.28	10.49	1.41	515.6	2.0	0.7	0.083	23.6	44.5	45.5	9.0	0.08	0.04	0.55	0.35
2100_500	1328.67	11.79	1.59	357.7	1.3	0.5	0.057	24.2	48.8	41.7	8.6	0.08	0.04	0.53	0.23
2200_100	713.03	6.3	0.85	190.5	0.7	0.3	0.030	14.6	43.4	48.0	7.6	0.09	0.04	0.64	0.21
2200_180	1992.74	17.7	2.38	674.2	2.6	0.9	0.108	30.1	58.8	29.5	11.0	0.04	0.02	0.31	0.36
2100_600(calibrating) heat-insulation	829.45	7.37	0.99	-	-	-	-	18.3	40.3	53.3	5.4	0.11	0.05	0.79	-
2100_200 "deep" thermocouple	951.55	8.46	1.14	308.3	1.2	0.4	0.049	20.2	41.8	49.4	7.7	0.09	0.04	0.64	0.24
2100_200 heat-insulation	576.29	5.11	0.69	79.3	0.3	0.1	0.013	15.3	33.5	60.2	5.2	0.12	0.06	0.86	0.08
2100_400 heat-insulation	807.09	7.17	0.96	121.9	0.5	0.2	0.020	17.8	40.2	52.4	6.4	0.11	0.05	0.74	0.11
2200_180 heat-insulation	1107.45	9.8	1.32	391.4	1.5	0.5	0.063	19.7	49.9	39.7	9.5	0.07	0.03	0.47	0.32

Table 8. Comparison of chemical and image analysis results

Test	Element content in the melt, wt %					
	U		Zr		O	
	image analysis	chemical analysis	image analysis	chemical analysis	image analysis	chemical analysis
2100_600(calibrating)	36.74±1.10	32.13±0.48	57.29±1.72	58.91±1.18	4.94±0.15	7.36±0.15
2100_100	45.68±1.37	42.08±0.63	46.22±1.39	47.83±0.96	7.20±0.22	8.63±0.17
2100_200	51.67±1.55	48.79±0.73	37.47±1.12	38.57±0.77	9.99±0.30	11.54±0.23
2100_300	54.18±1.63	50.90±0.76	35.30±1.06	35.77±0.72	9.73±0.29	12.32±0.25
2100_400	44.47±1.33	43.74±0.66	45.47±1.36	44.07±0.88	9.04±0.27	11.52±0.23
2100_500	48.78±1.46	42.63±0.64	41.74±1.25	45.43±0.91	8.60±0.26	10.49±0.21
2200_100	43.41±1.30	37.62±0.56	47.97±1.44	50.72±1.01	7.64±0.23	10.63±0.21
2200_180	58.77±1.76	59.32±0.89	29.47±0.88	27.82±0.56	11.03±0.33	12.31±0.25
2100_600(calibrating) heat-insulation	40.33±1.21	33.48±0.50	53.30±1.60	58.00±1.16	5.42±0.16	7.64±0.15
2100_200 "deep" thermocouple	41.80±1.25	42.90±0.64	49.43±1.48	46.56±0.93	7.75±0.23	9.58±0.19
2100_200 heat-insulation	33.49±1.00	31.14±0.47	60.16±1.80	60.50±1.21	5.22±0.16	7.50±0.15
2100_400 heat-insulation	40.22±1.21	36.26±0.54	52.42±1.57	53.53±1.07	6.37±0.19	9.18±0.18
2200_180 heat-insulation	49.88±1.50	47.37±0.71	39.72±1.19	40.36±0.81	9.50±0.29	10.95±0.22

Table 9. U/(U+Zr) ratio in the melt

Test	time$^{0.5}$	U/(U+Zr), wt%	
		image analysis	chemical analysis
2100_600(calibrating)	24.49	39.07	35.29
2100_100	10.00	49.70	46.80
2100_200	14.14	57.96	55.85
2100_300	17.32	60.55	58.73
2100_400	20.00	49.45	49.81
2100_500	22.36	53.89	48.41
2200_100	10.00	47.51	42.59
2200_180	13.42	66.60	68.07
2100_600(calibrating) heat-insulation	24.49	43.07	36.60
2100_200 “deep” thermocouple	14.14	45.82	47.95
2100_200 heat-insulation	14.14	35.76	33.98
2100_400 heat-insulation	20.00	43.42	40.38
2200_180 heat-insulation	13.42	55.67	54.00

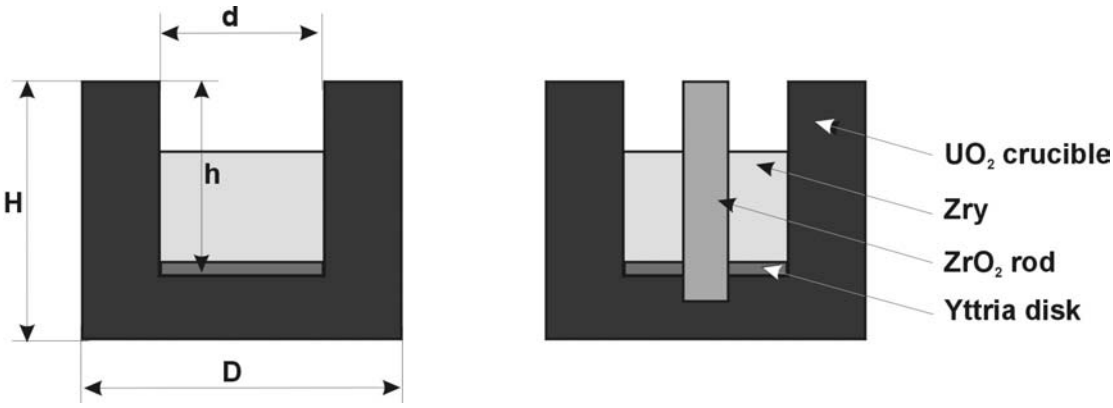

Fig. I - 1. Test specimens

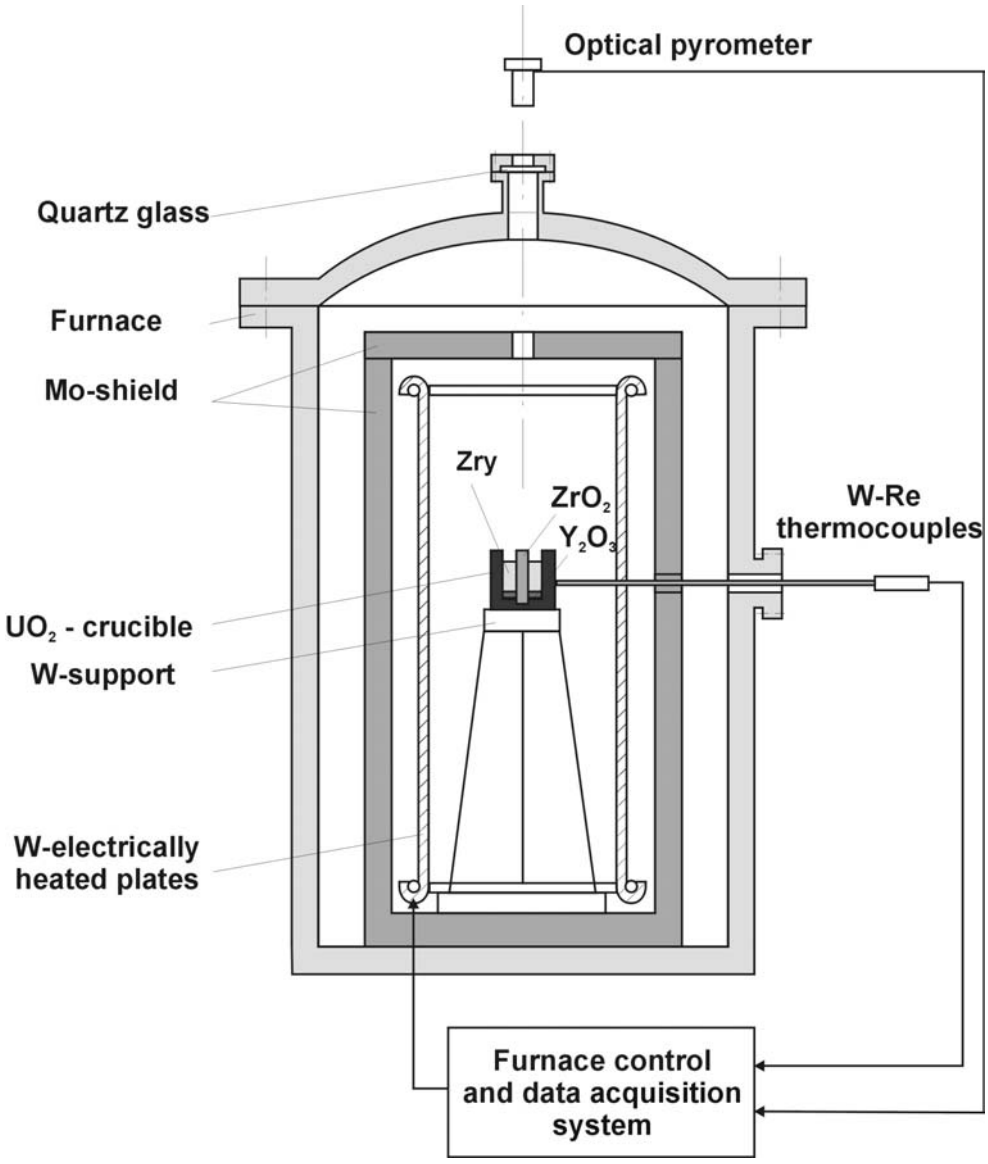

Fig. I - 2. Test rig

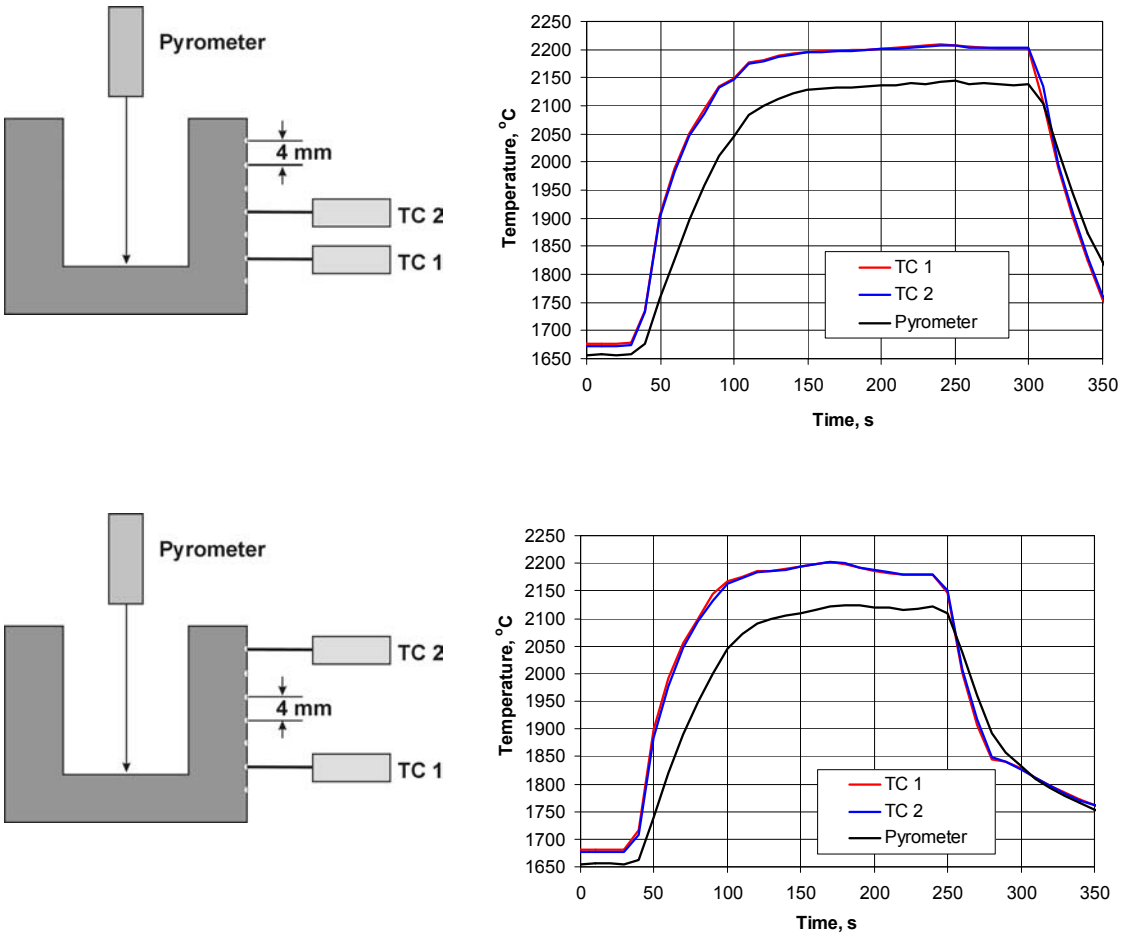

Fig. I - 3. Measurement of temperature gradient along the crucible sidewall

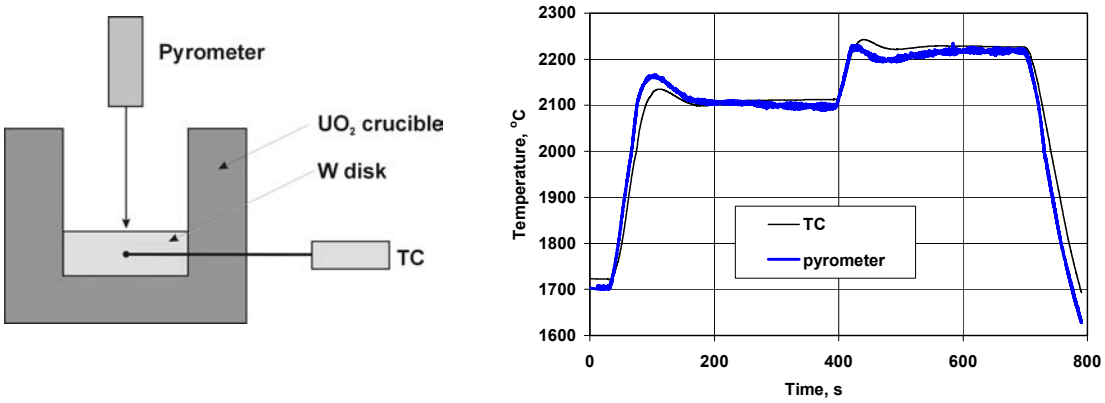

Fig. I - 4. Test for comparison of the thermocouple and pyrometer temperature readings

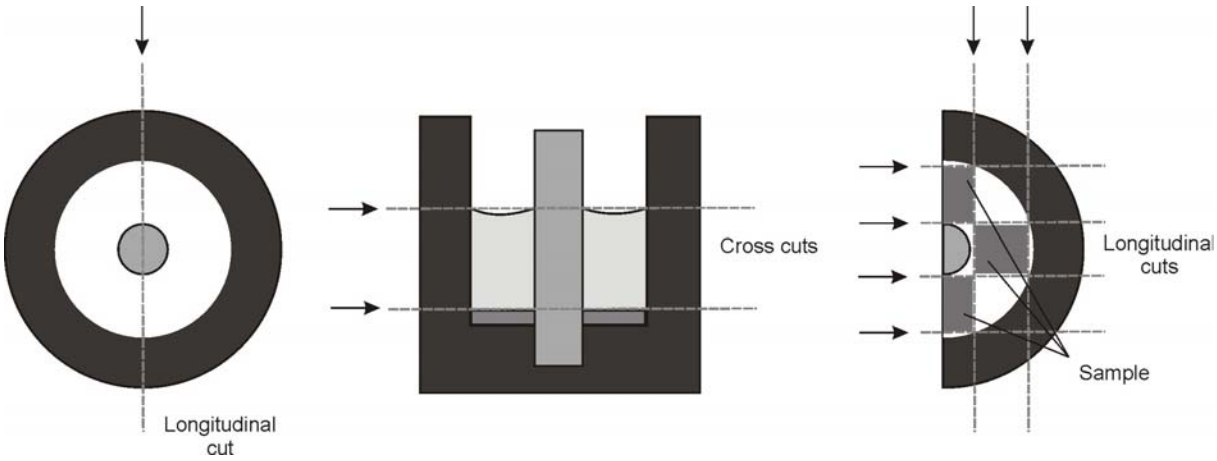

Fig. I - 5. Melt sampling for chemical analysis

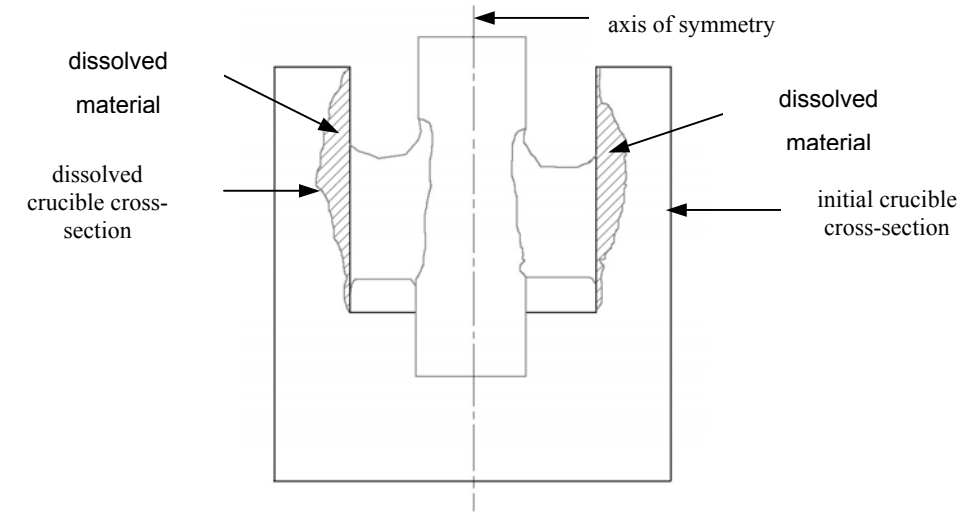

a

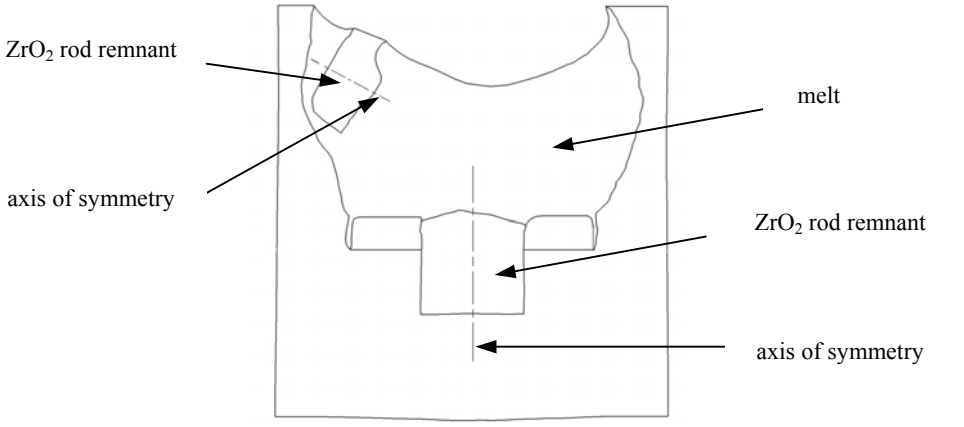

b

Fig. I - 6. Schematic model of image analysis measurements of dissolved sidewall (a) and central rod remnants volumes (b)

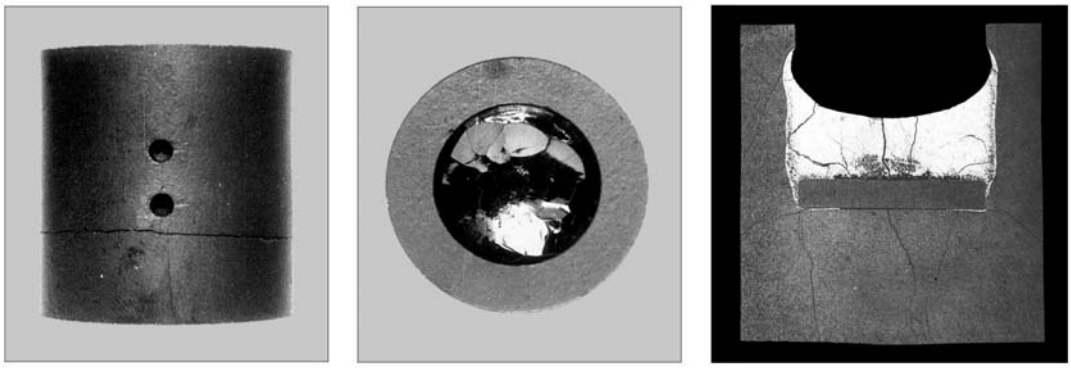

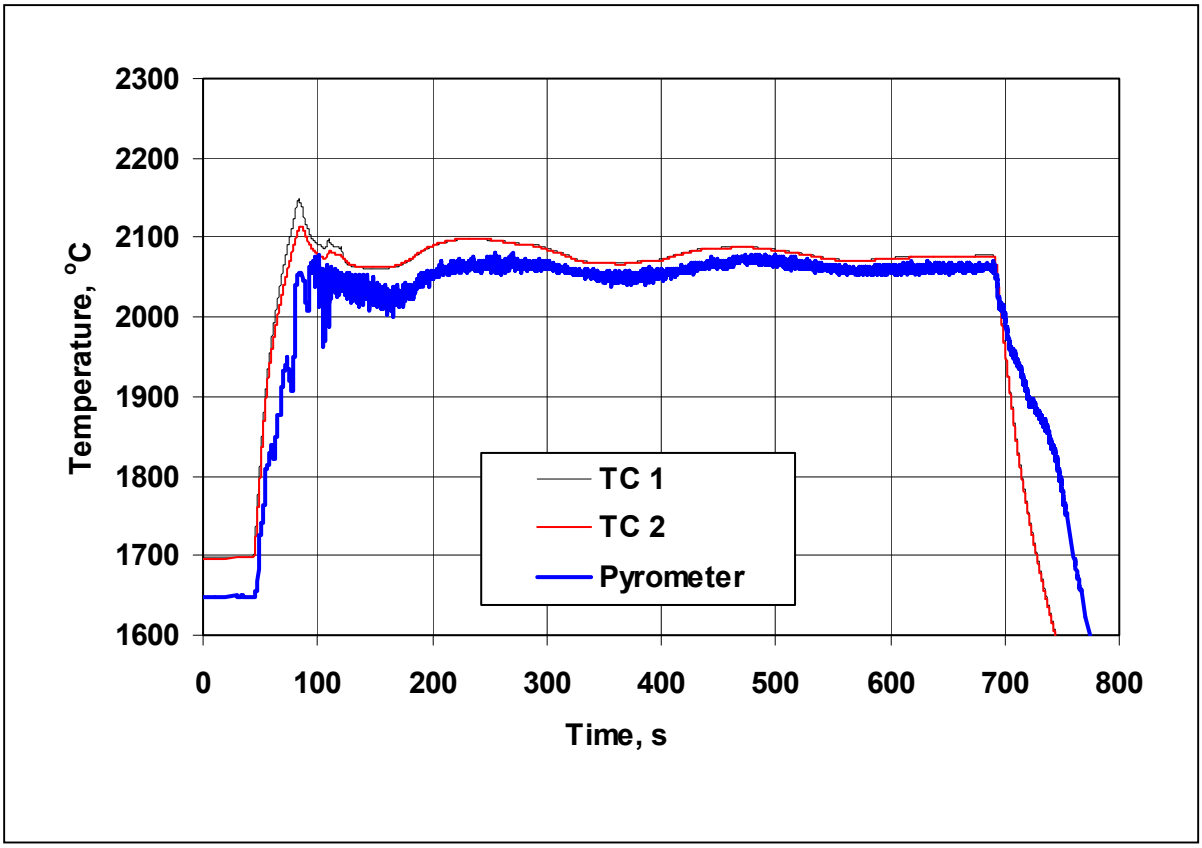

Fig. I - 7. Calibrating test 2100 °C, 600 s. Specimen appearance and test regime

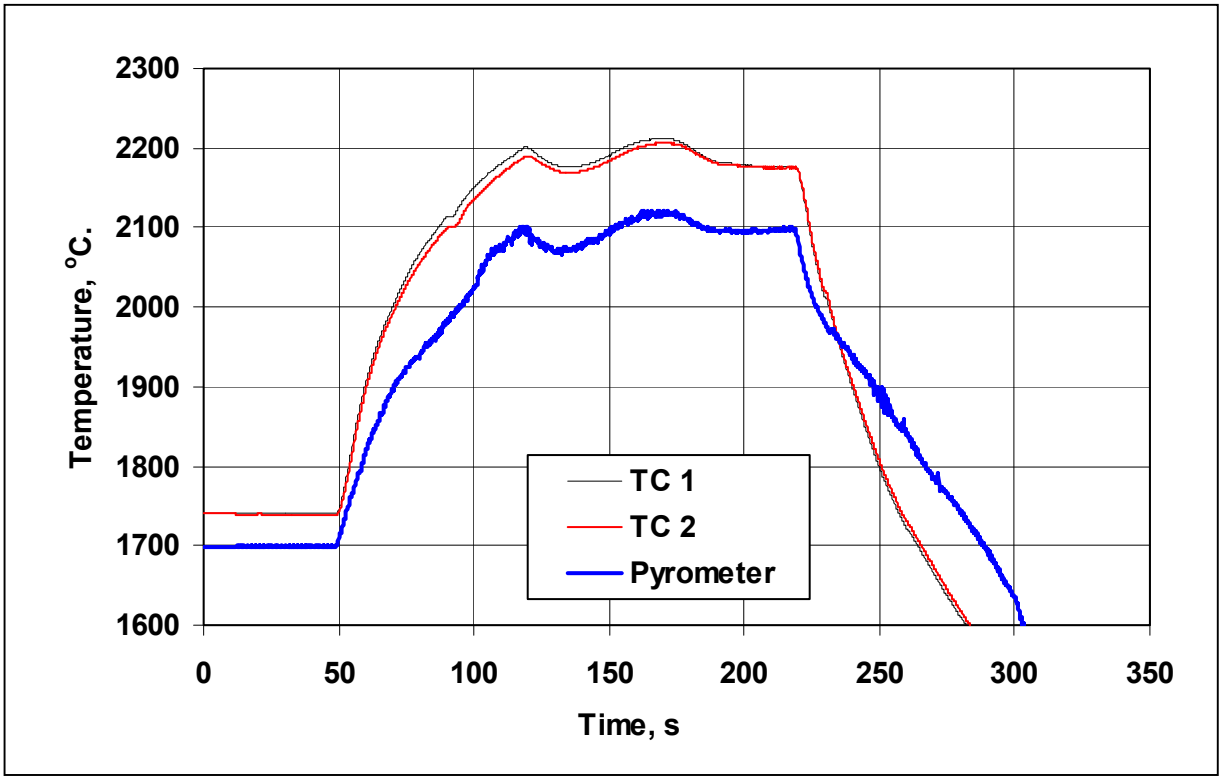

Fig. I - 8. Test 2100 °C, 100 s. Specimen appearance and test regime

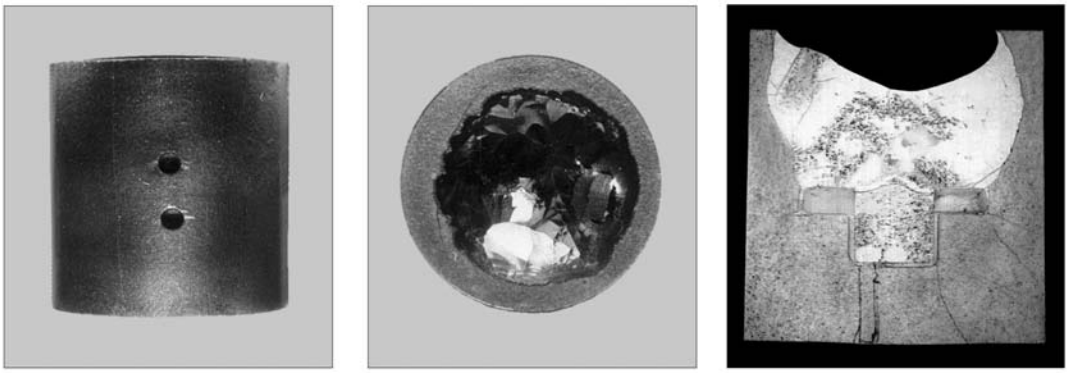

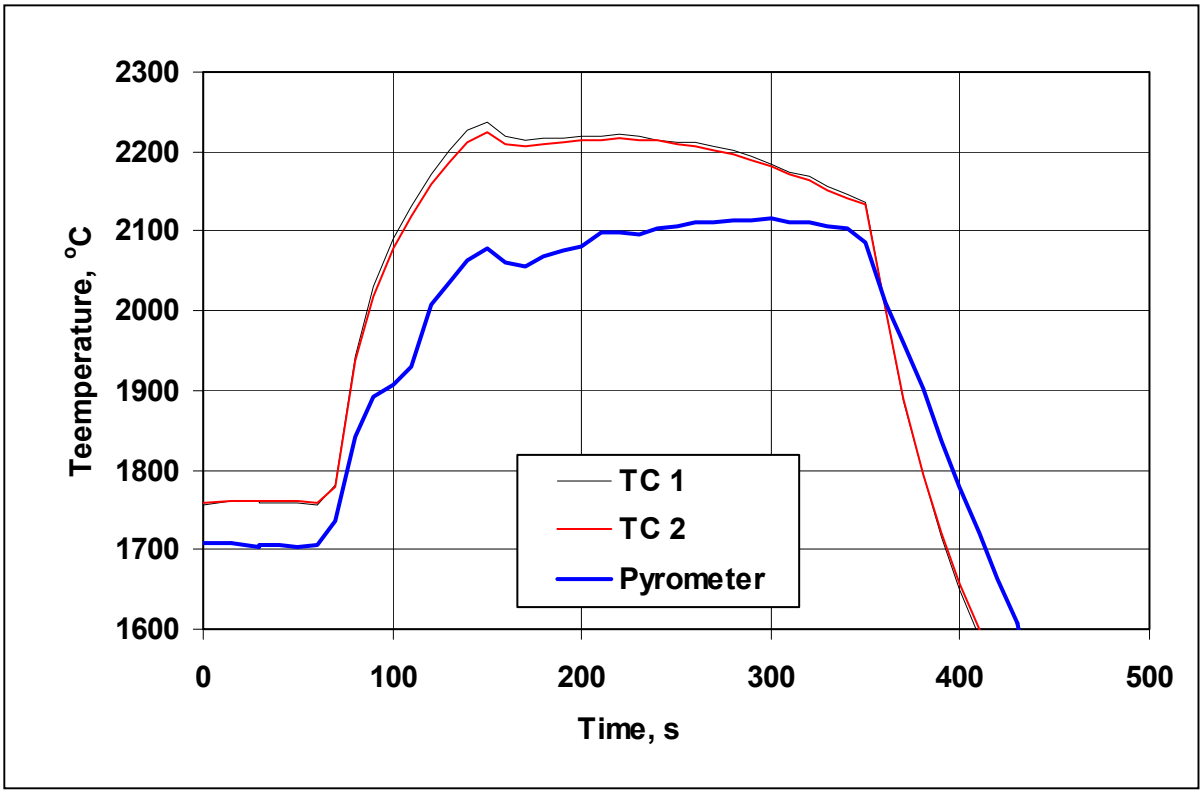

Fig. I - 9. Test 2100 °C, 200 s. Specimen appearance and test regime

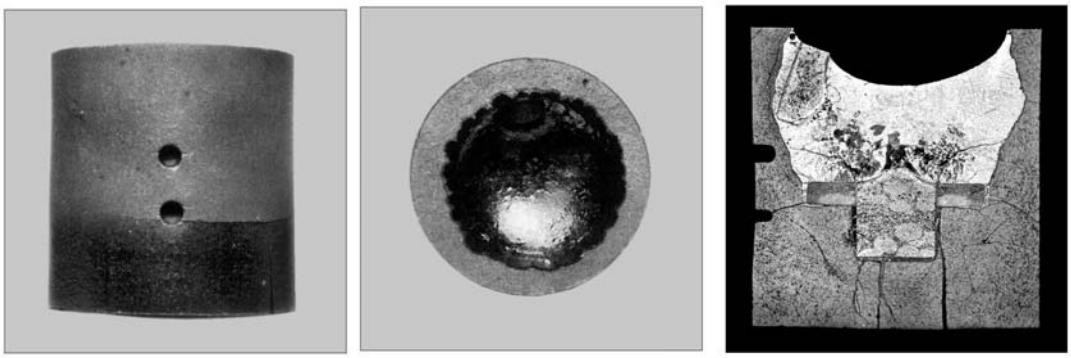

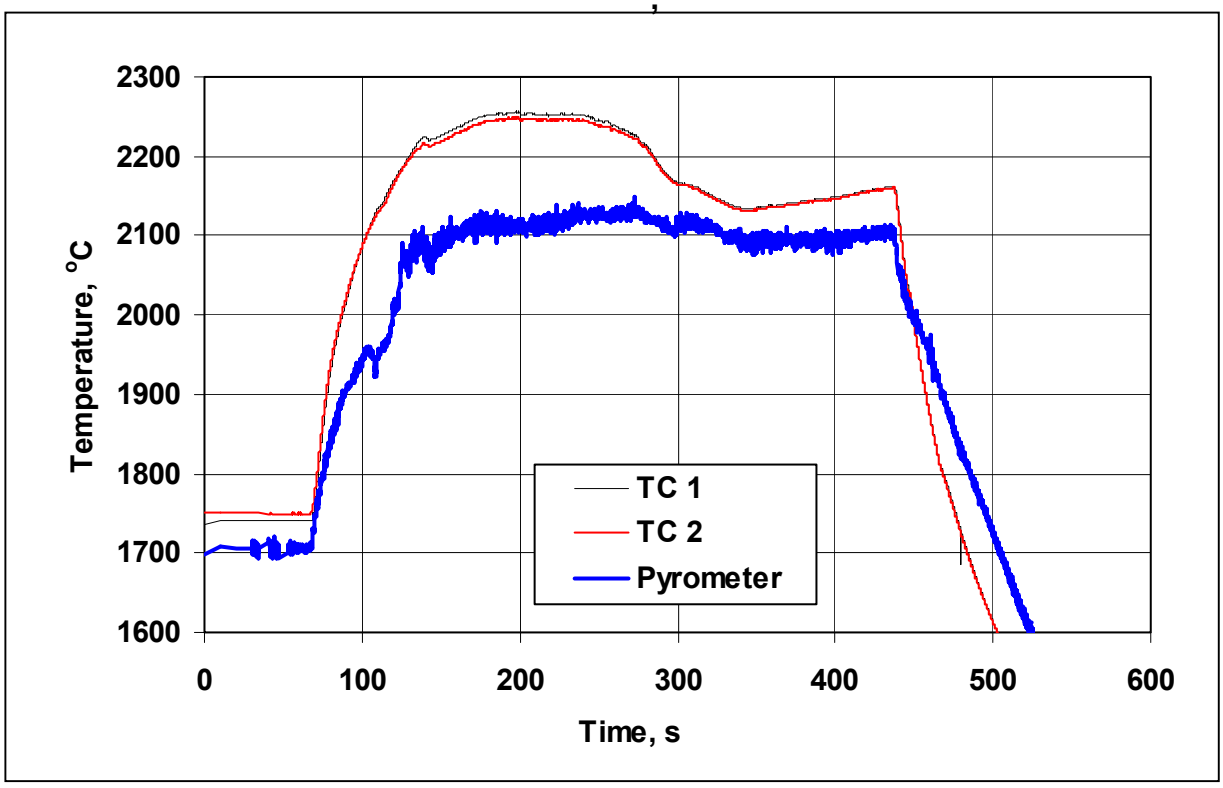

Fig. I - 10. Test 2100 °C, 300 s. Specimen appearance and test regime

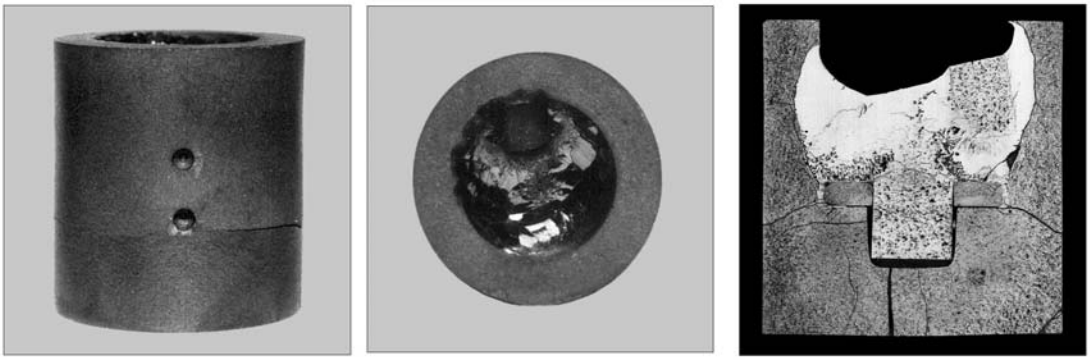

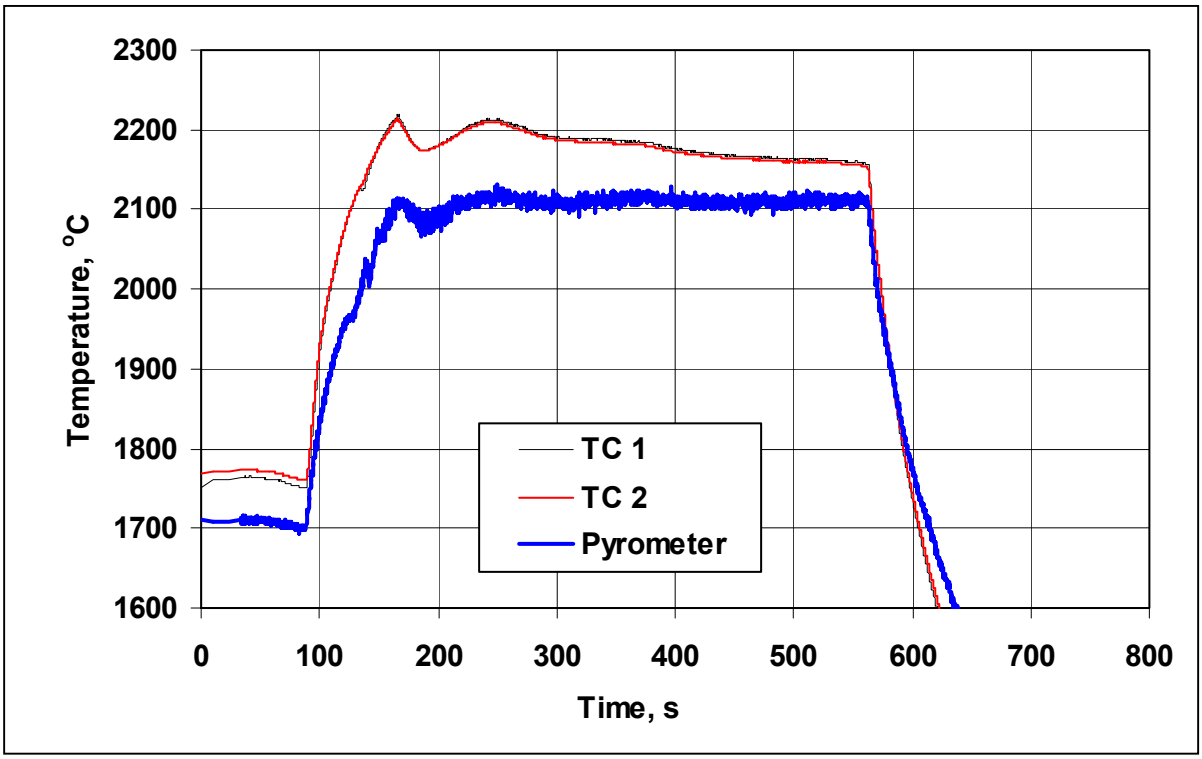

Fig. I - 11. Test 2100 °C, 400 s. Specimen appearance and test regime

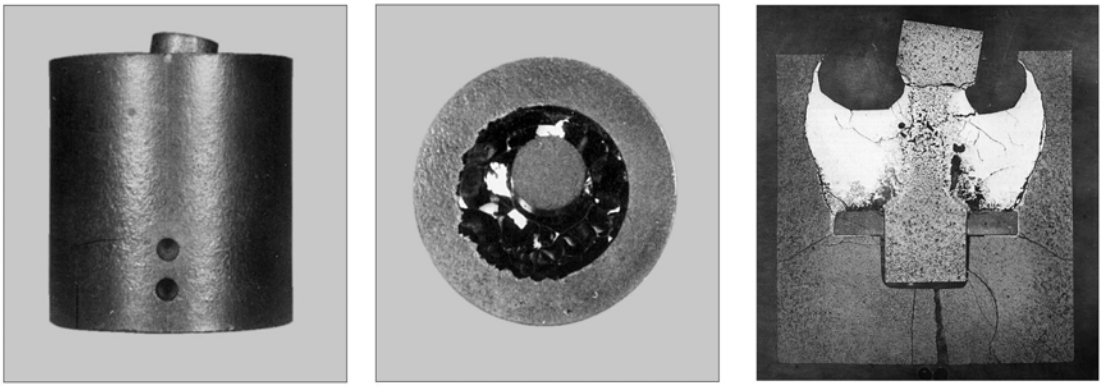

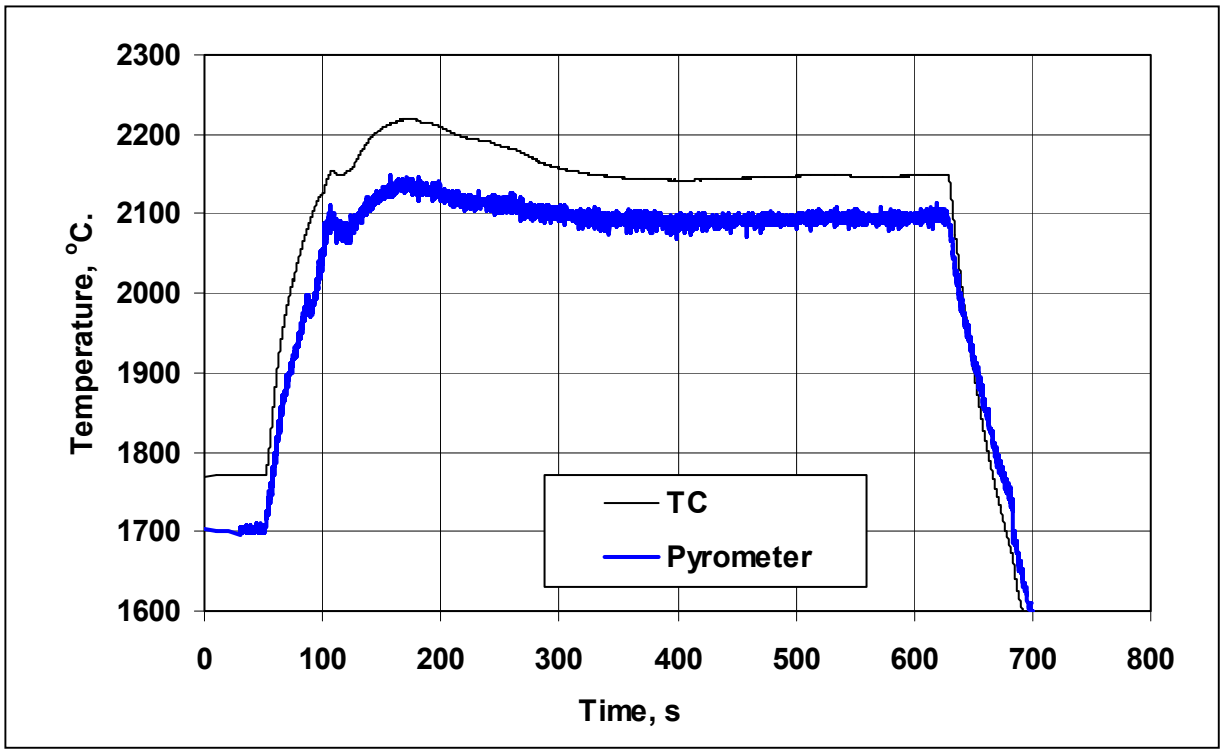

Fig. I - 12. Test 2100 °C, 500 s. Specimen appearance and test regime

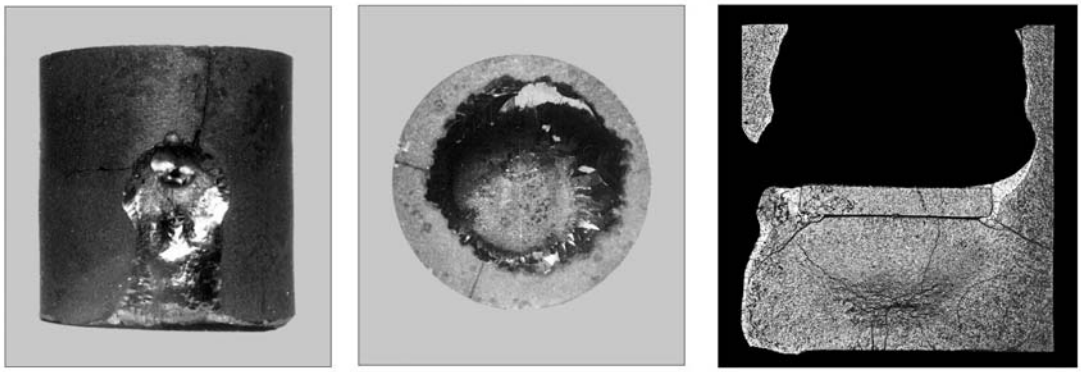

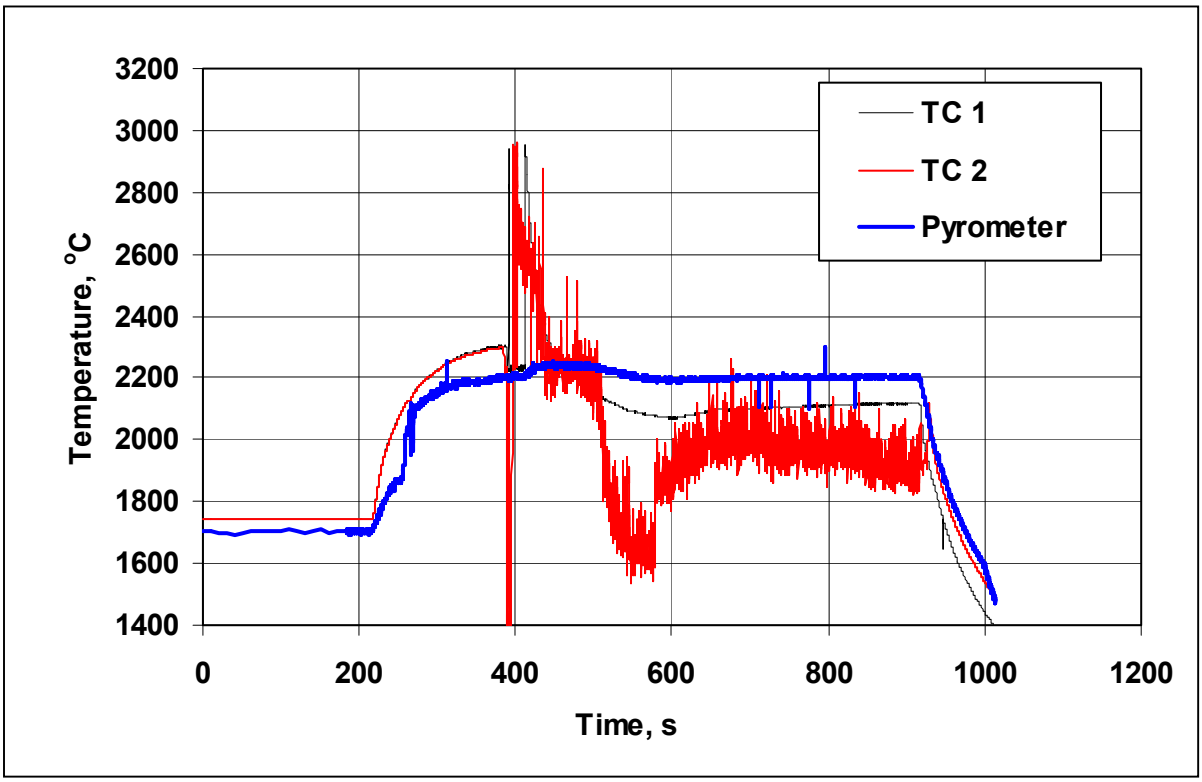

Fig. I - 13. Calibrating test 2200 °C, 600 s. Specimen appearance and test regime

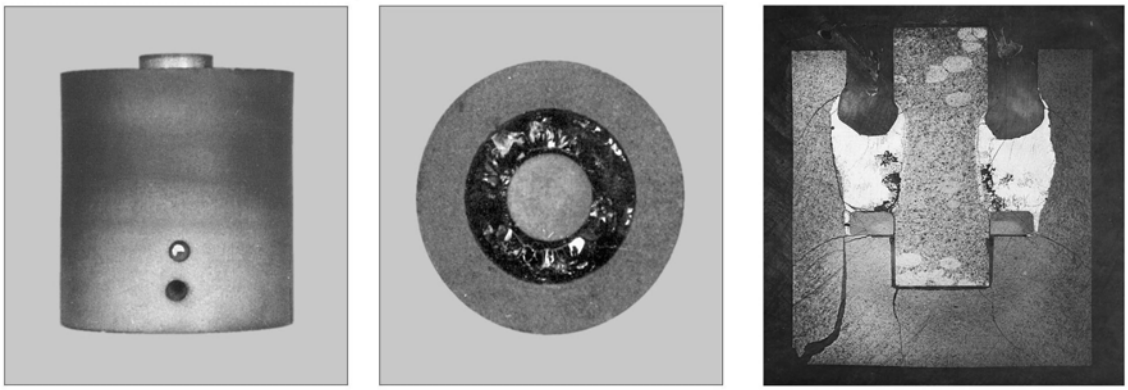

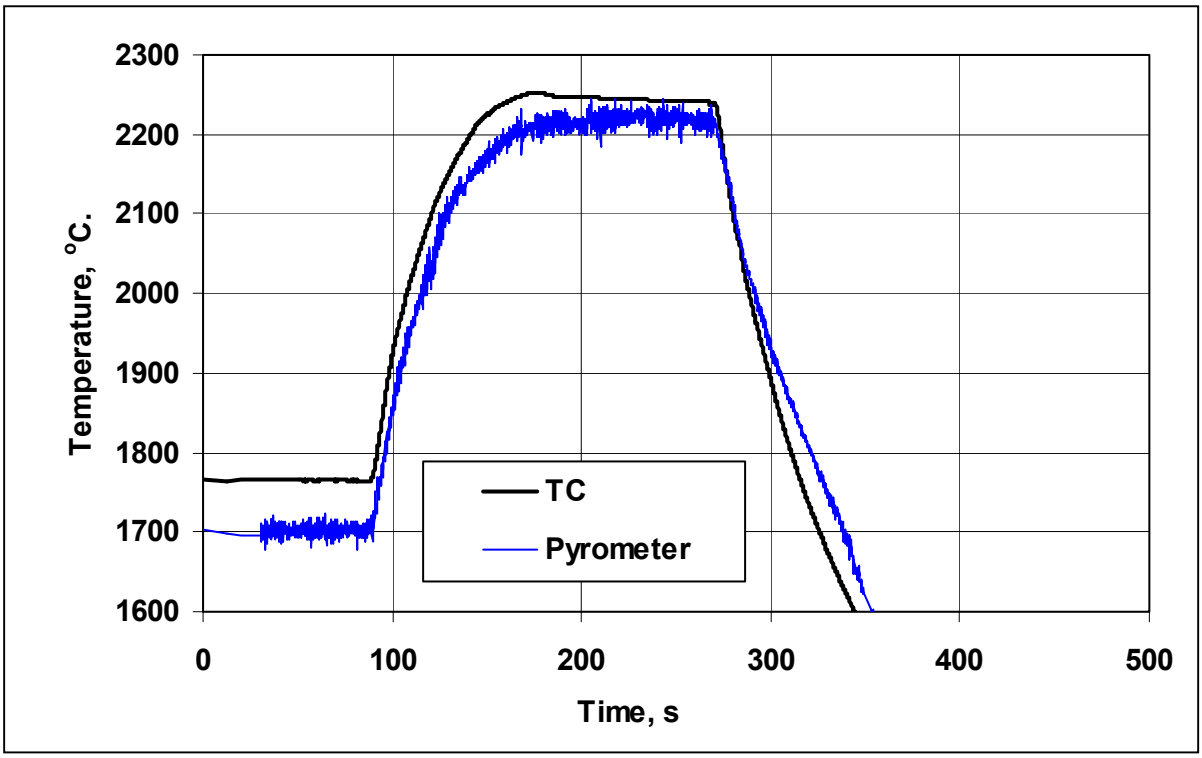

Fig. I - 14. Test 2200 °C, 100 s. Specimen appearance and test regime

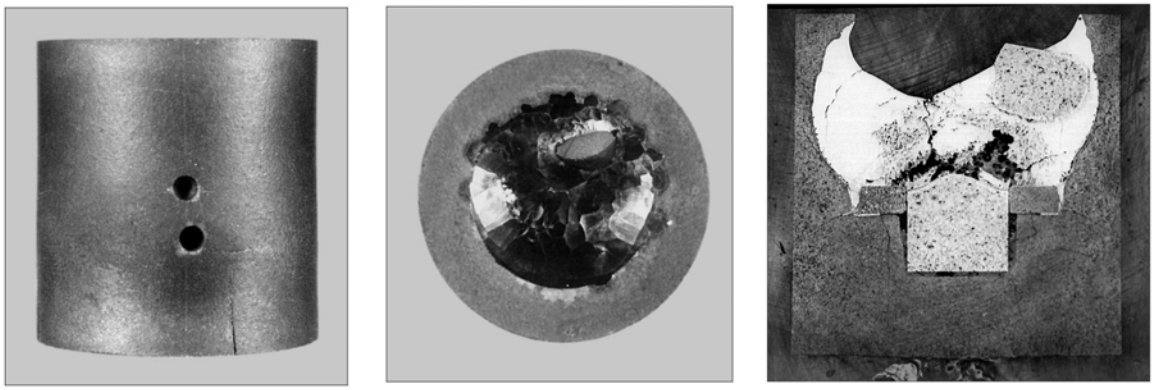

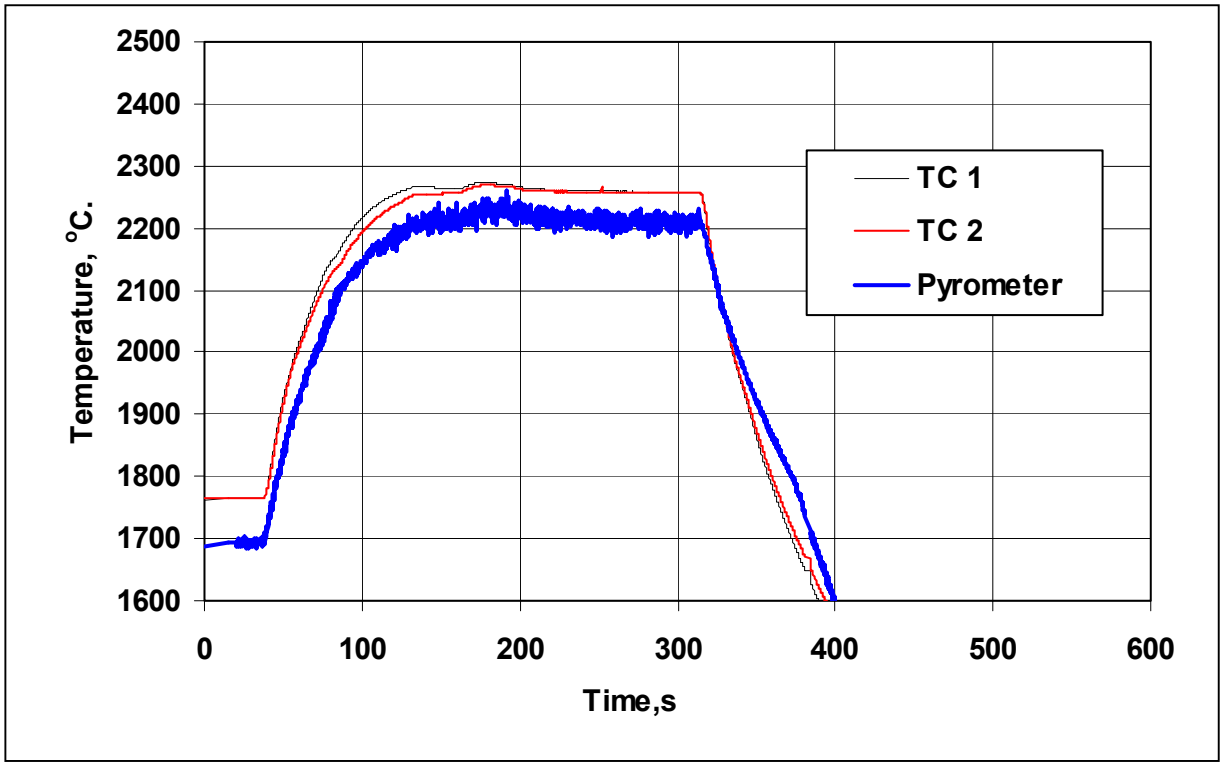

Fig. I - 15. Test 2200 °C, 180 s. Specimen appearance and test regime

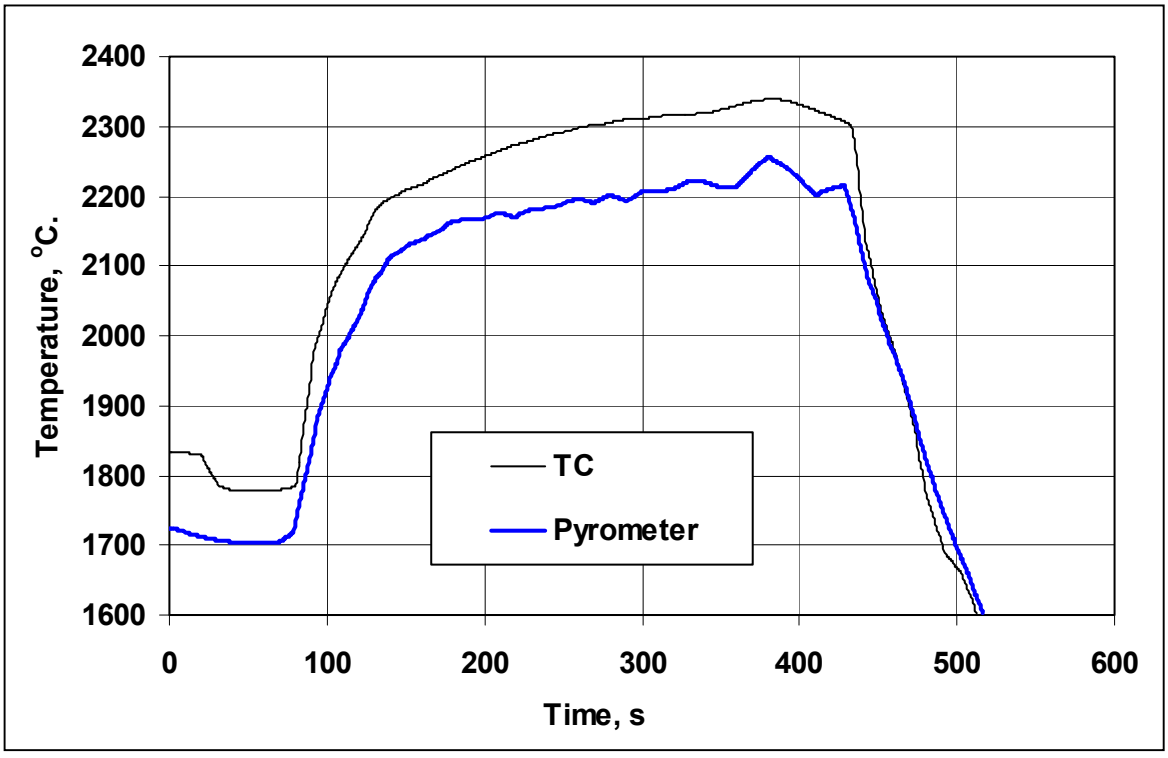

Fig. I - 16. Test 2200 °C, 260 s. Specimen appearance and test regime

Fig. I - 17. Calibrating test 2100 °C, 600 s. Structure of melt

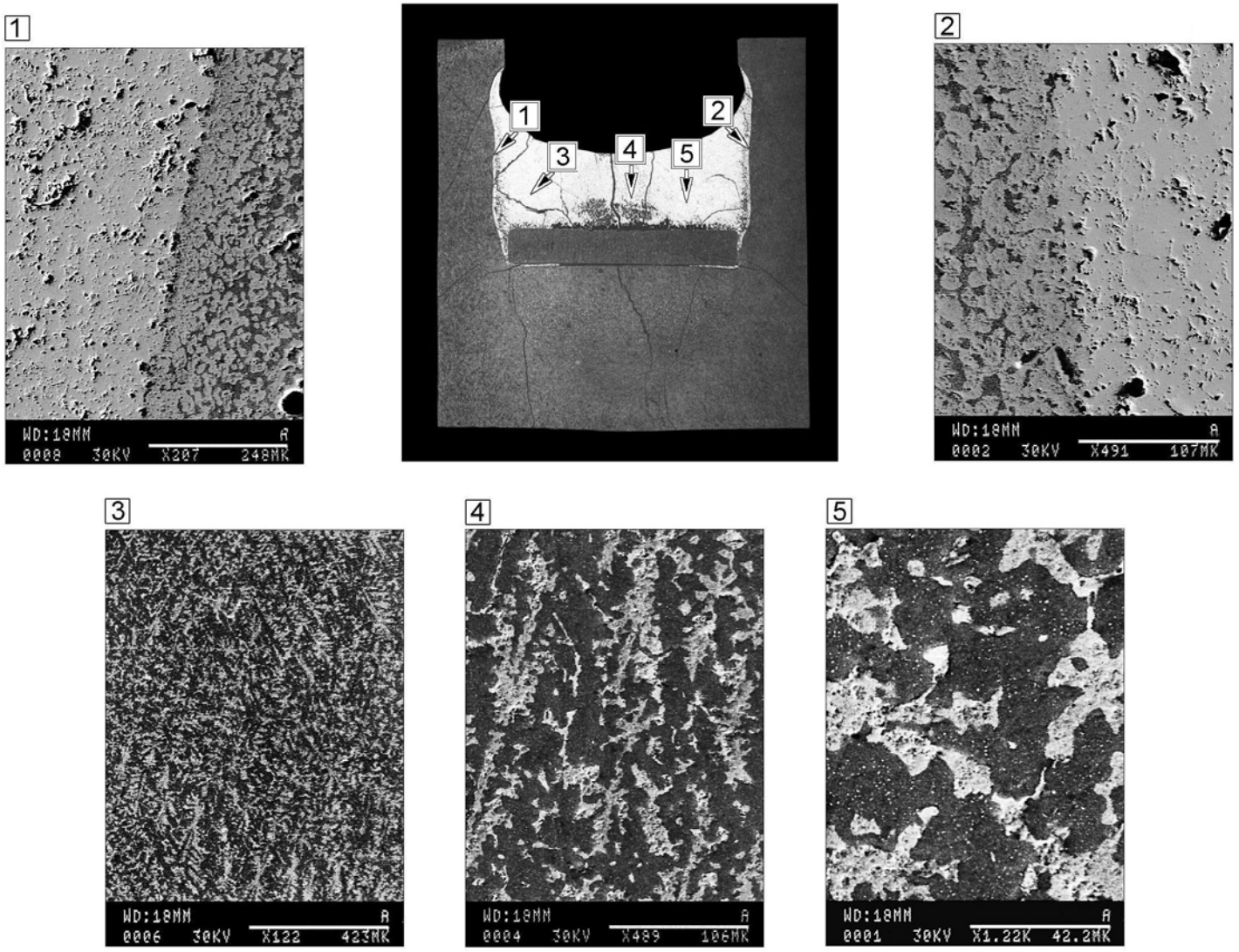

Fig. I - 18. Calibrating test 2100 °C, 600 s. Structure of melt (SEM)

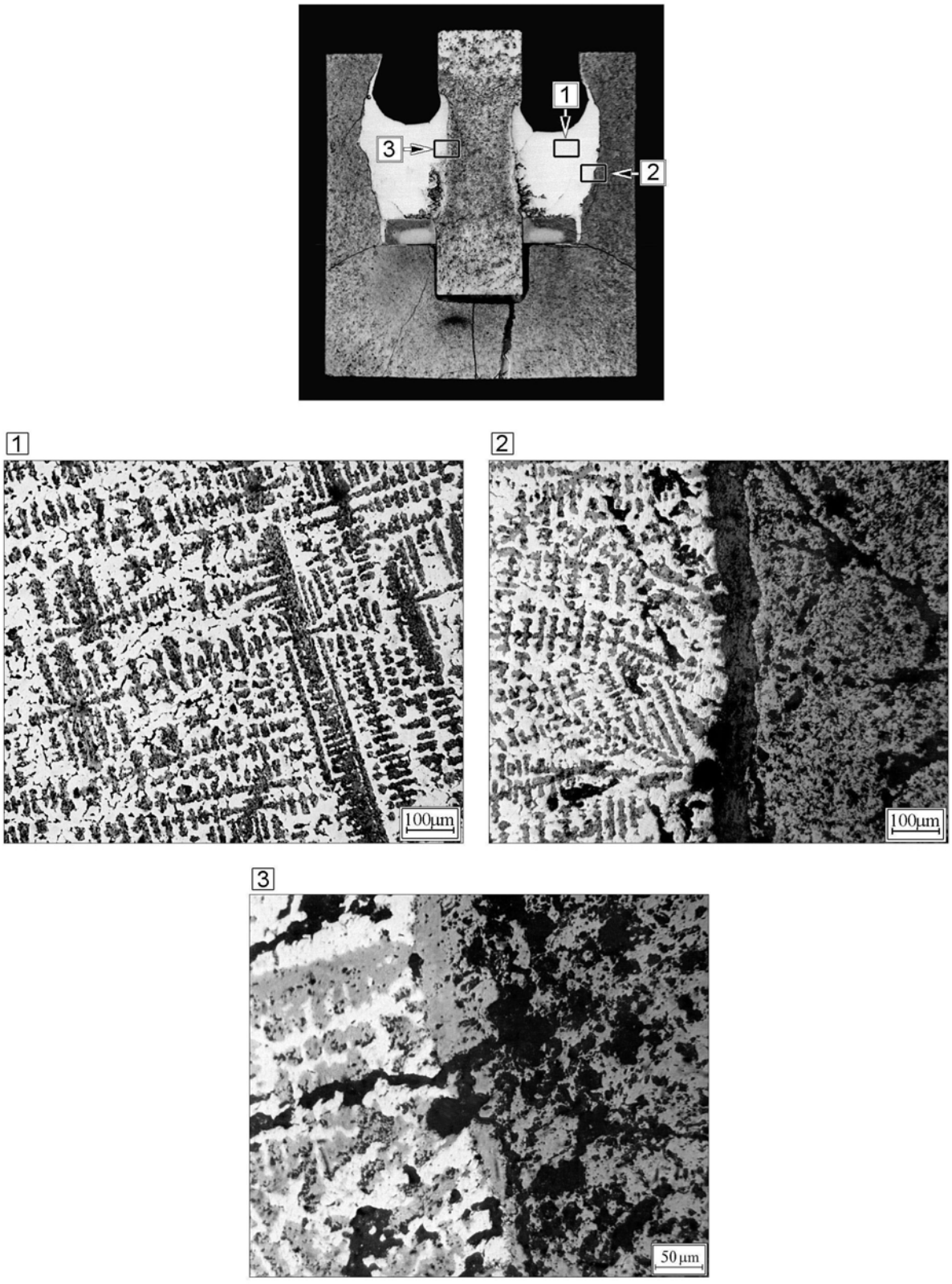

Fig. I - 19. Test 2100 °C, 100 s. Structure of melt

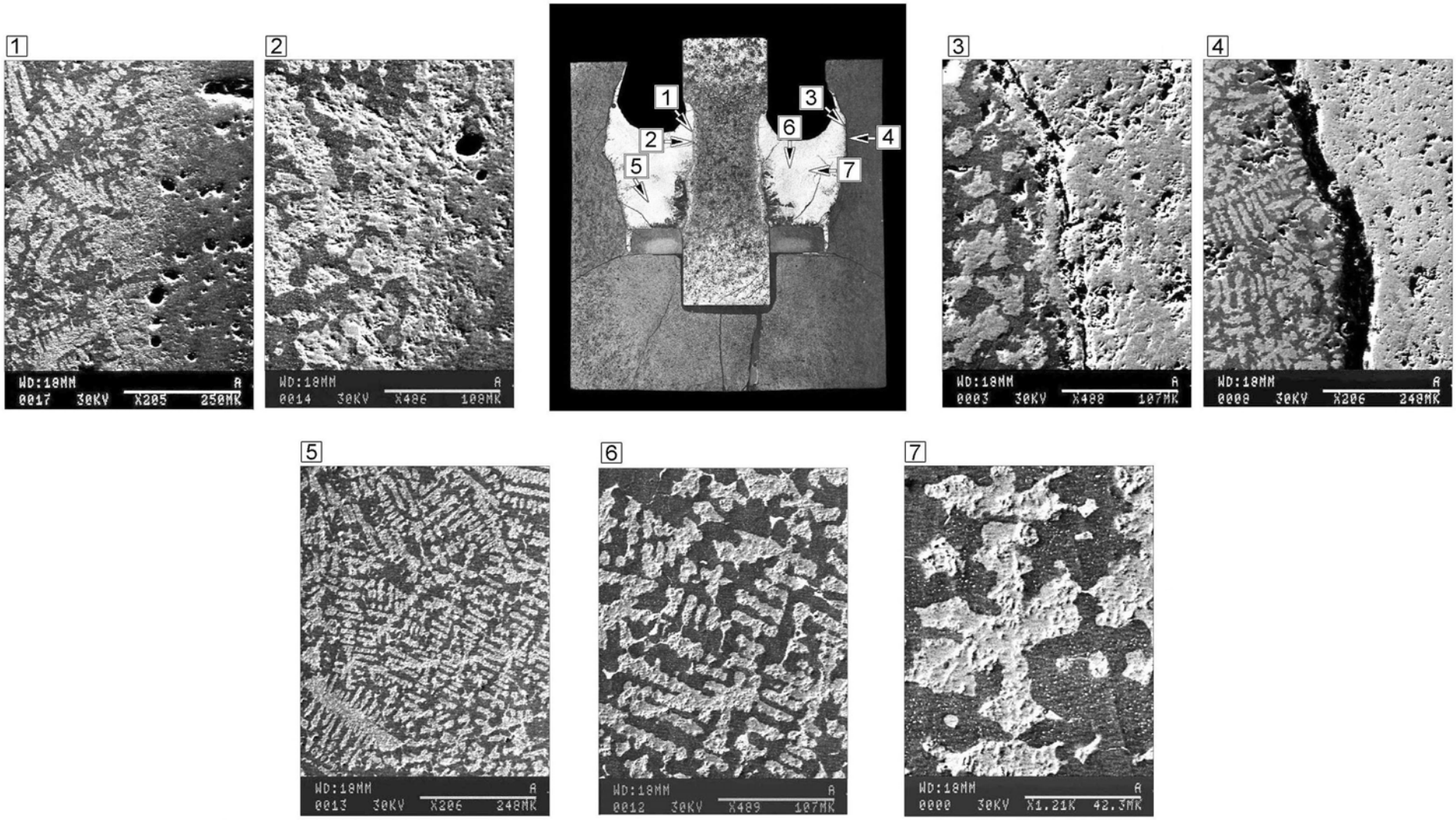

Fig. I - 20. Test 2100 °C, 100 s. Structure of melt (SEM)

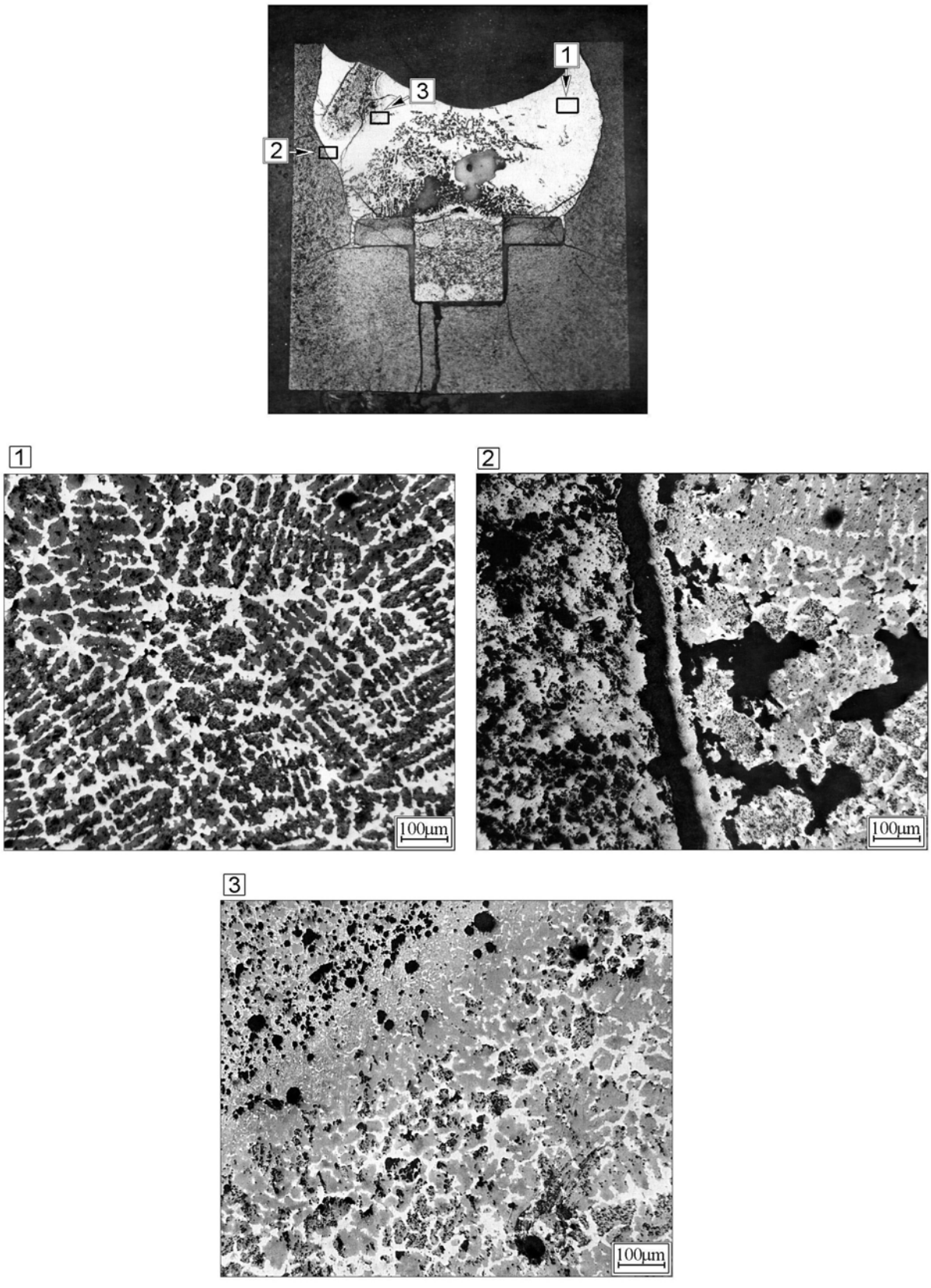

Fig. I - 21. Test 2100 °C, 200 s. Structure of melt

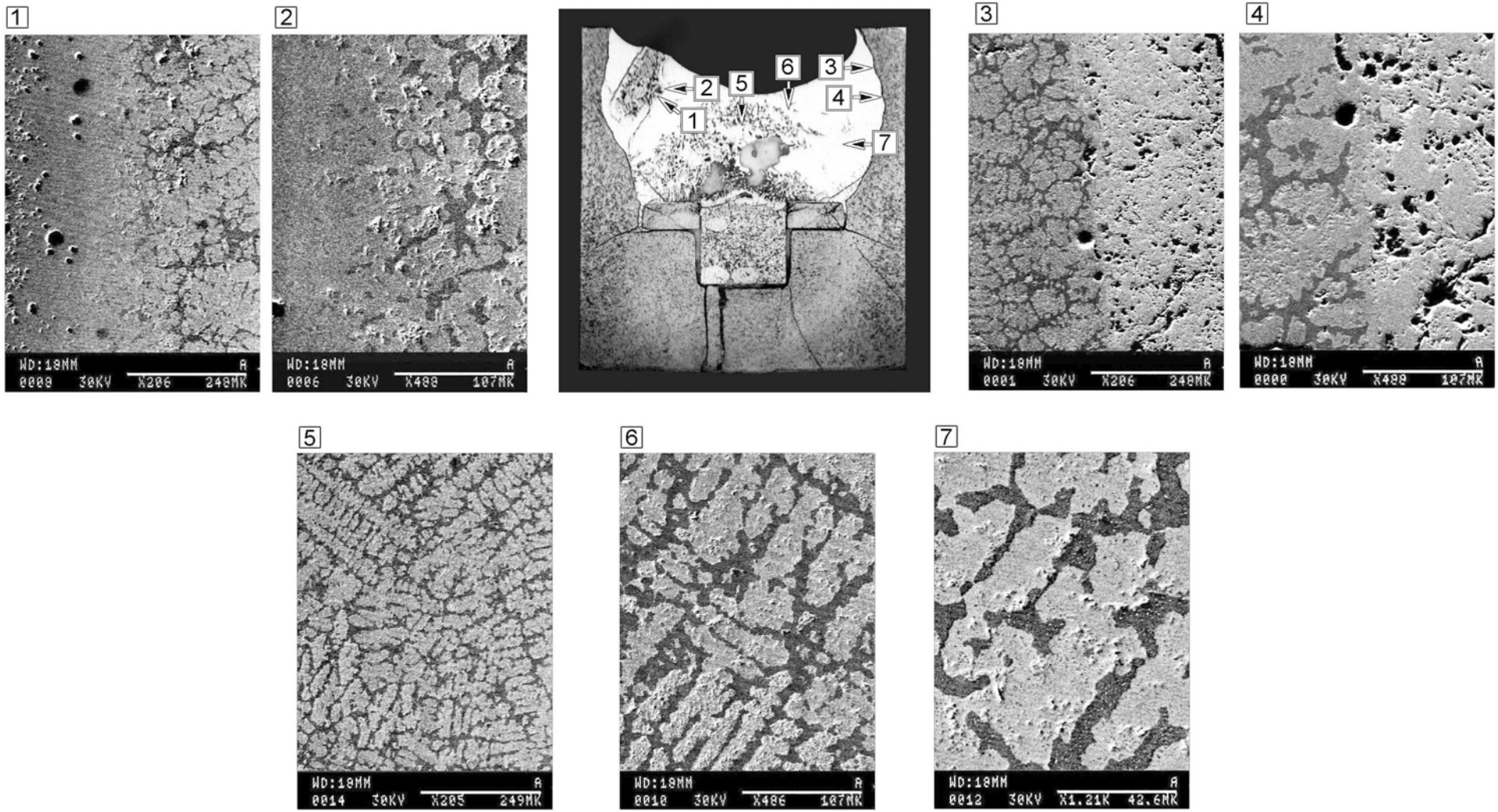

Fig. I - 22. Test 2100 °C, 200 s. Structure of melt (SEM)

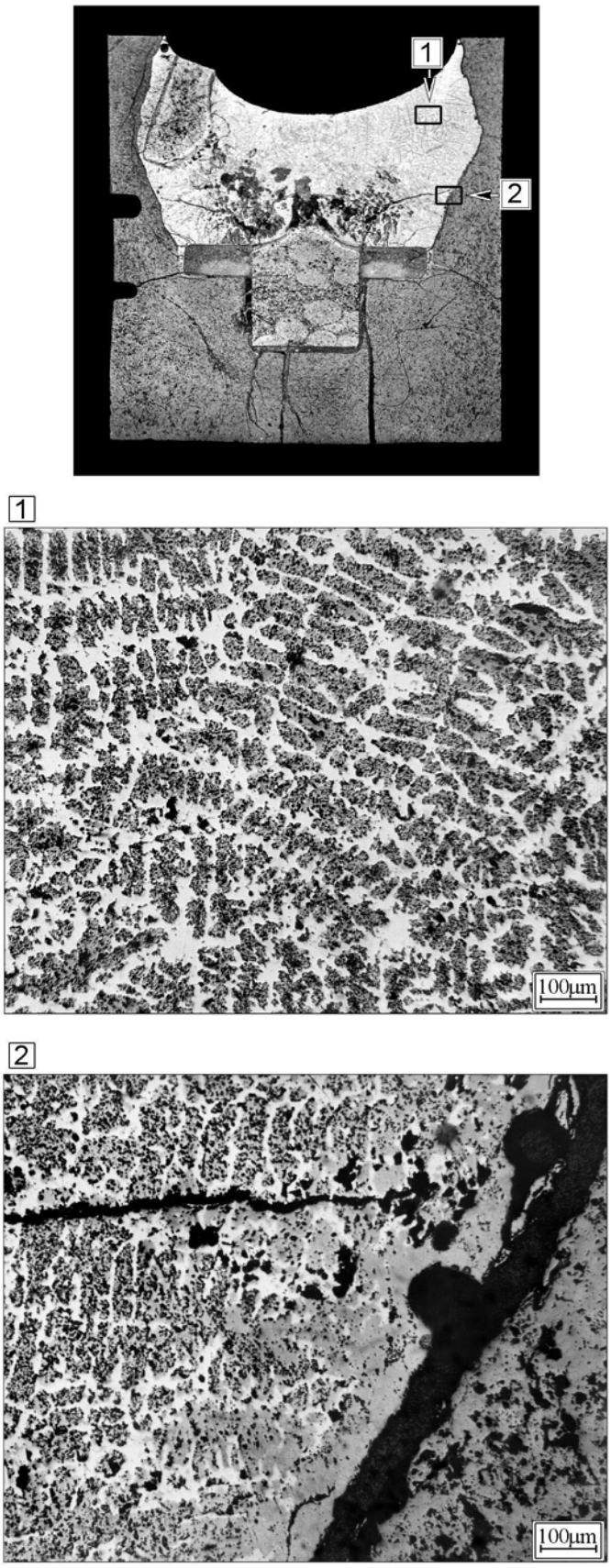

Fig. I - 23. Test 2100 °C, 300 s. Structure of melt

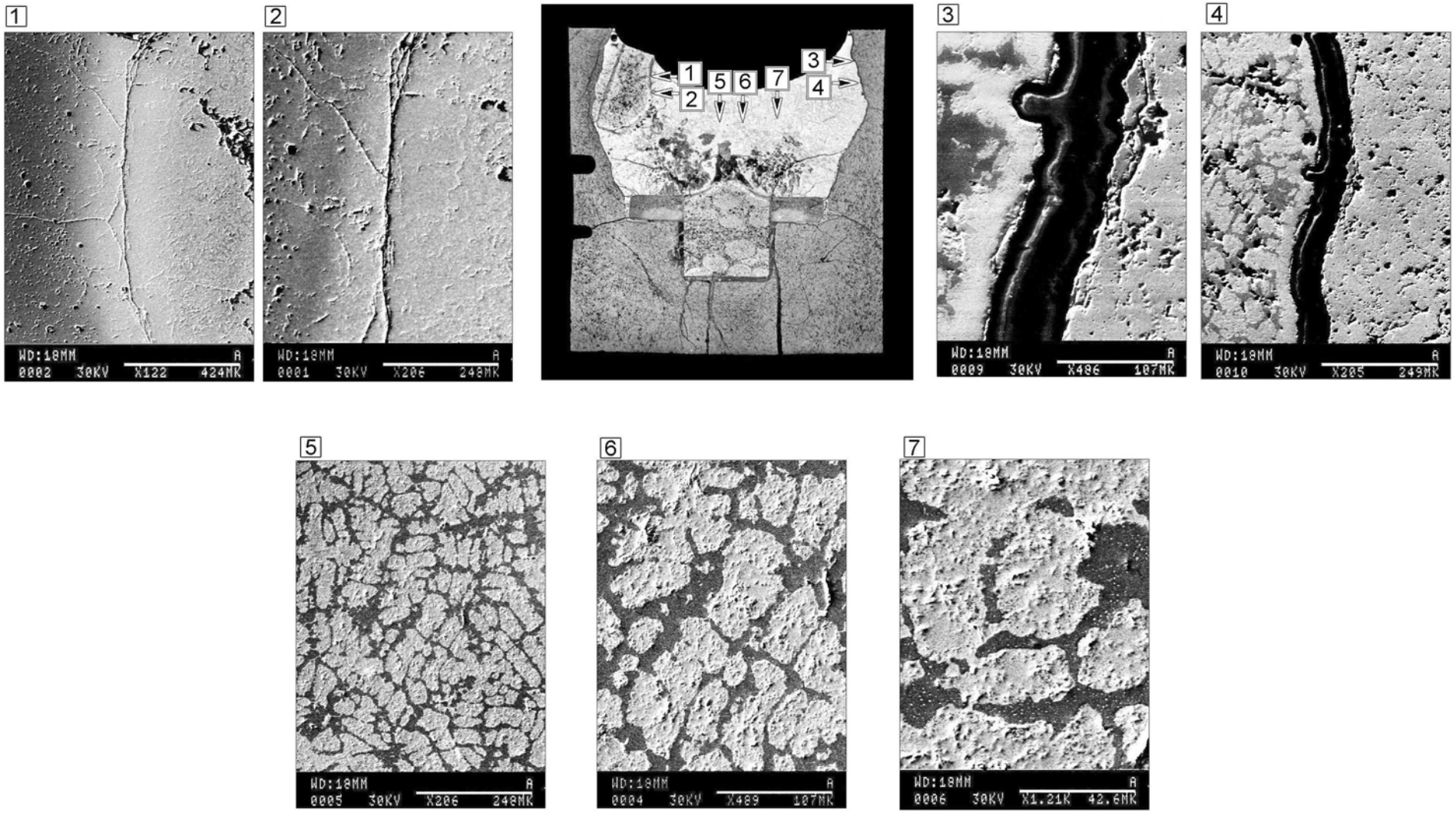

Fig. I - 24. Test 2100 °C, 300 s. Structure of melt (SEM)

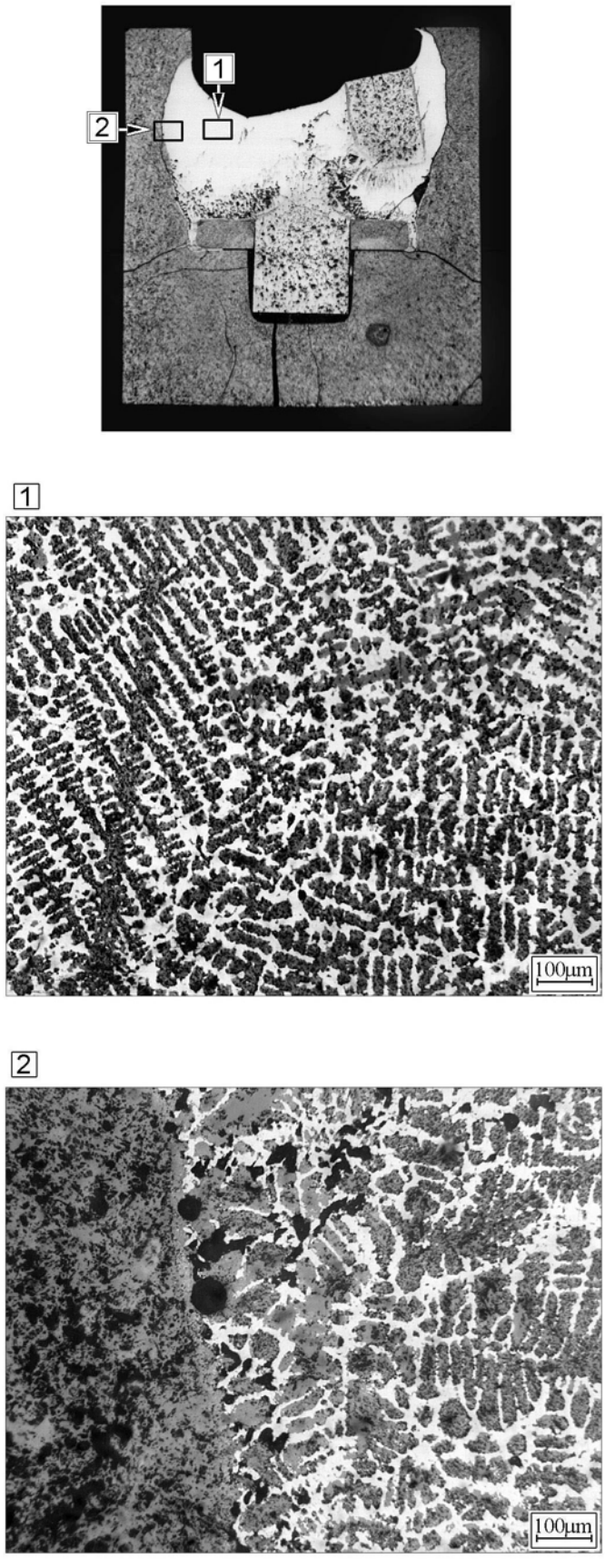

Fig. I - 25. Test 2100 °C, 400 s. Structure of melt

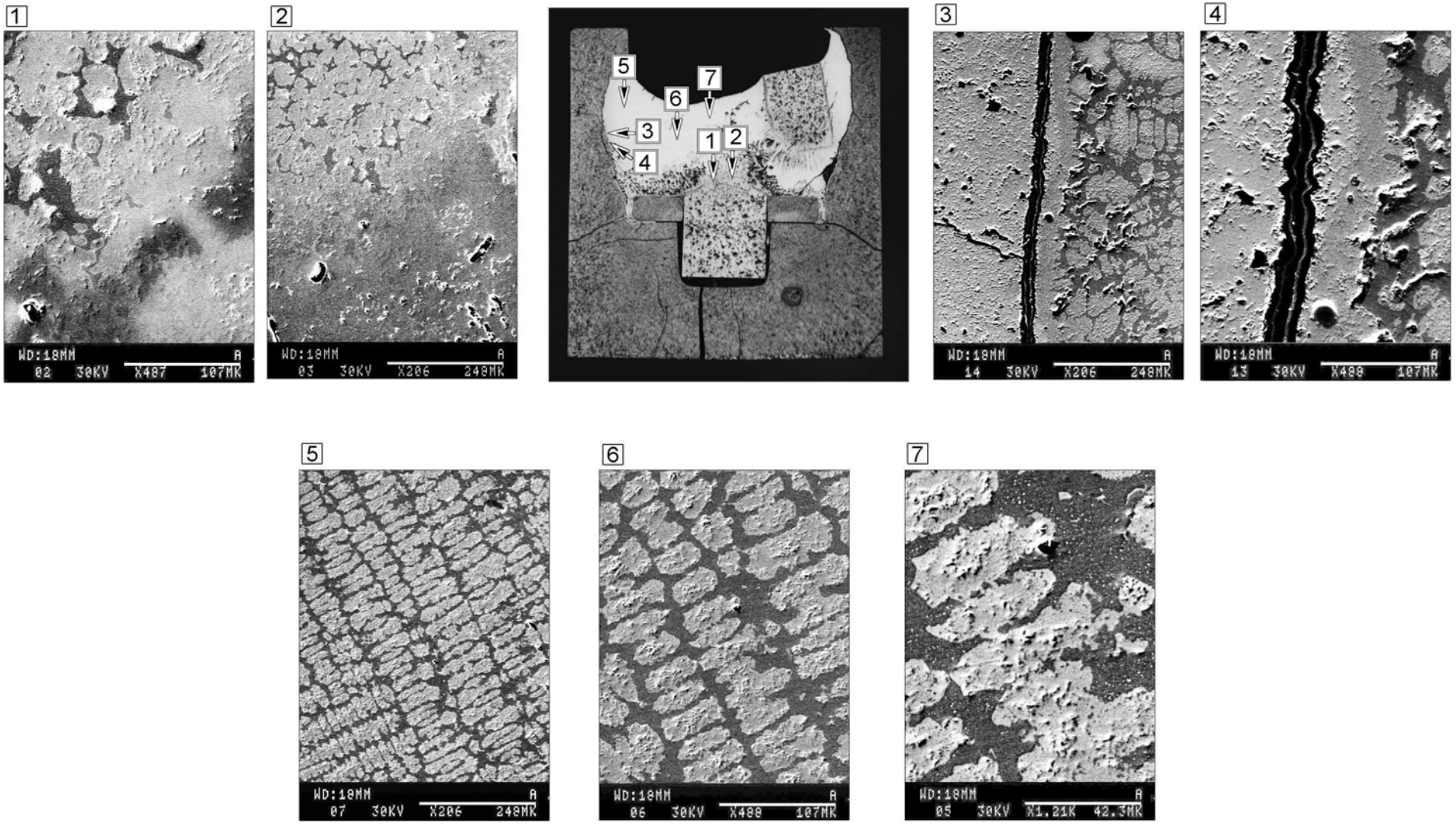

Fig. I - 26. Test 2100 °C, 400 s. Structure of melt (SEM)

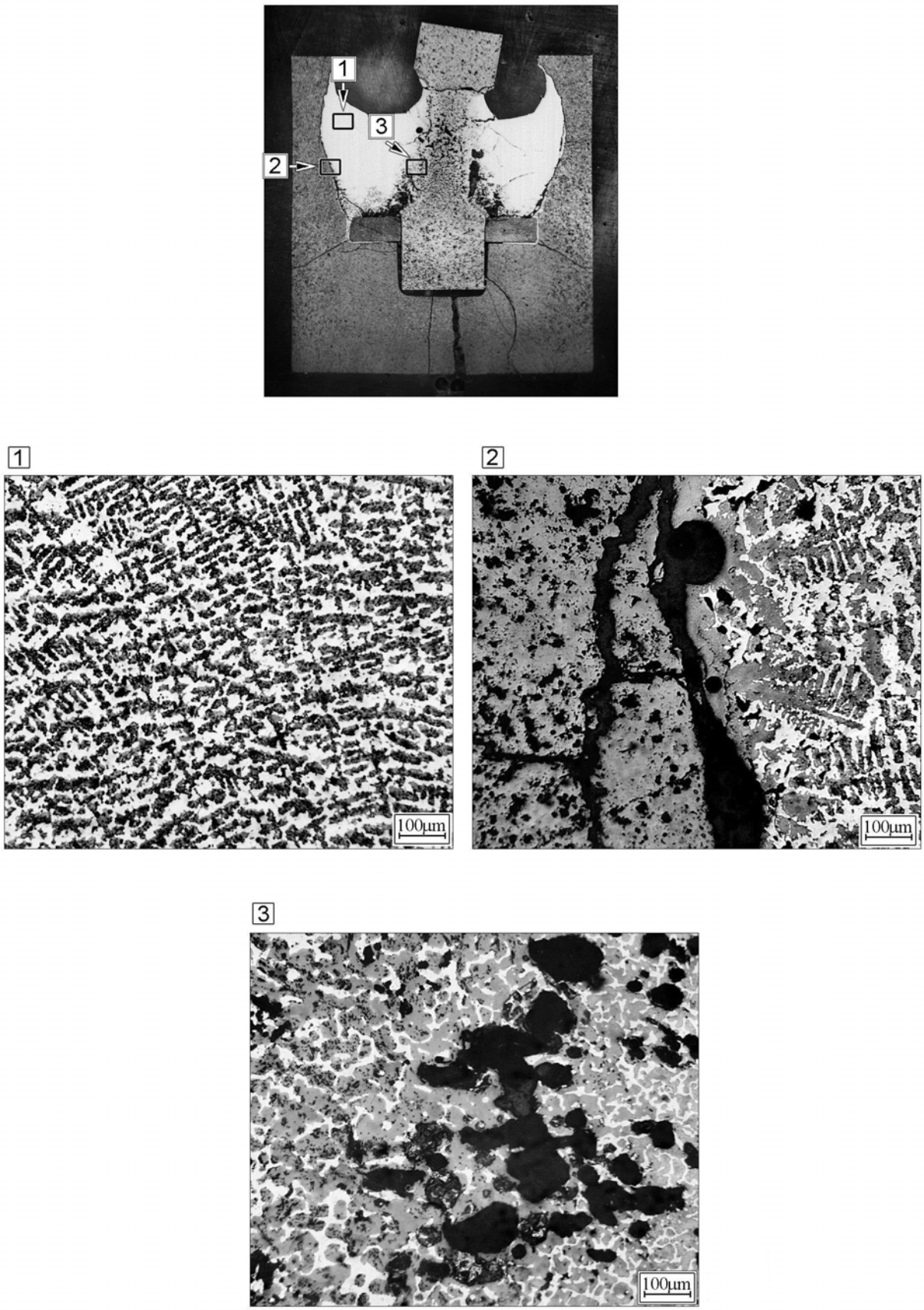

Fig. I - 27. Test 2100 °C, 500 s. Structure of melt

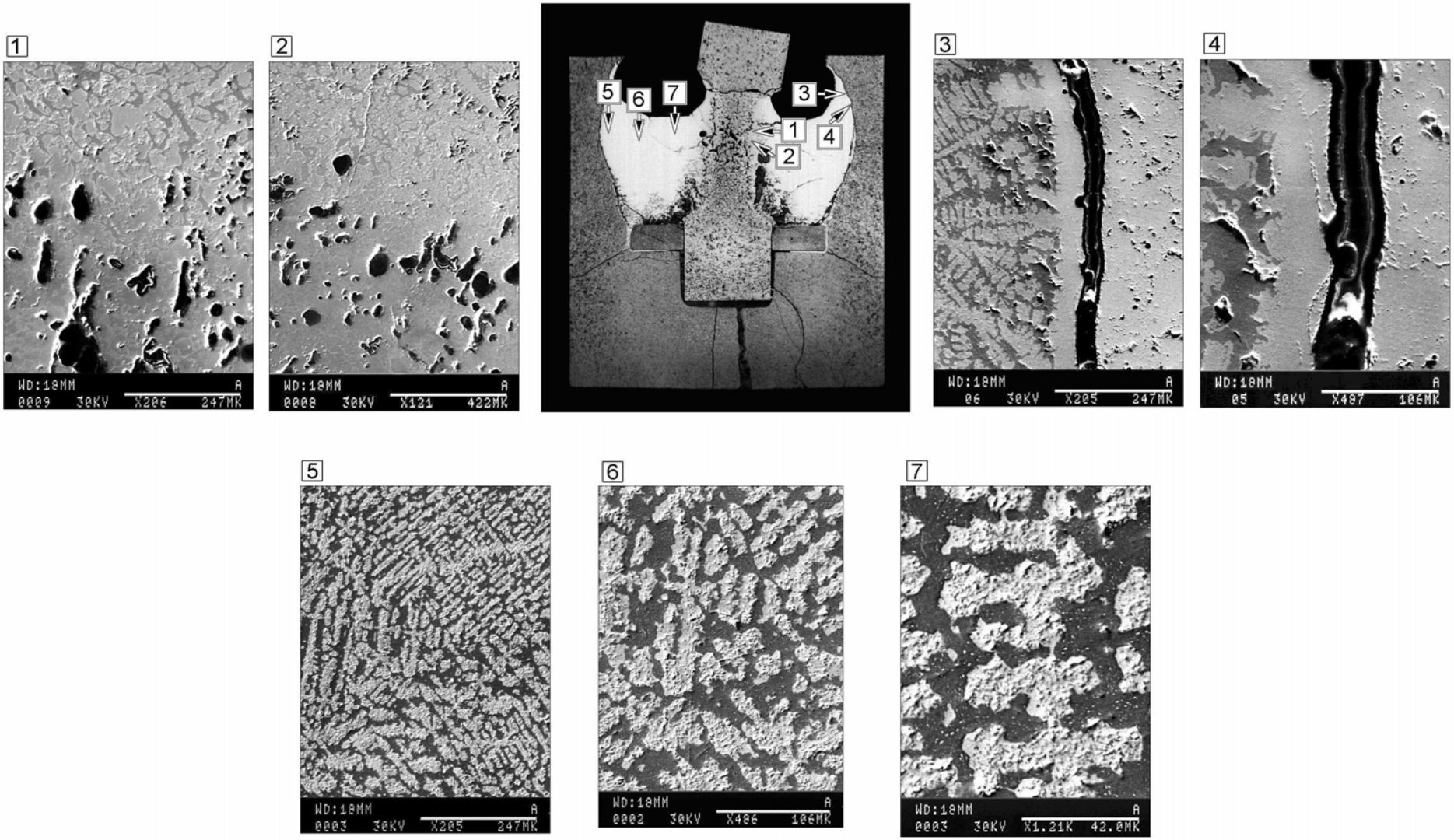

Fig. I - 28. Test 2100 °C, 500 s. Structure of melt (SEM)

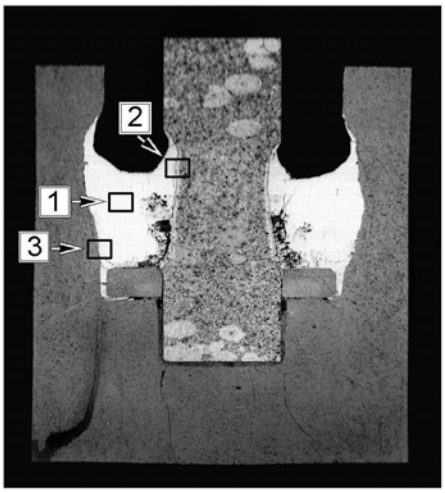

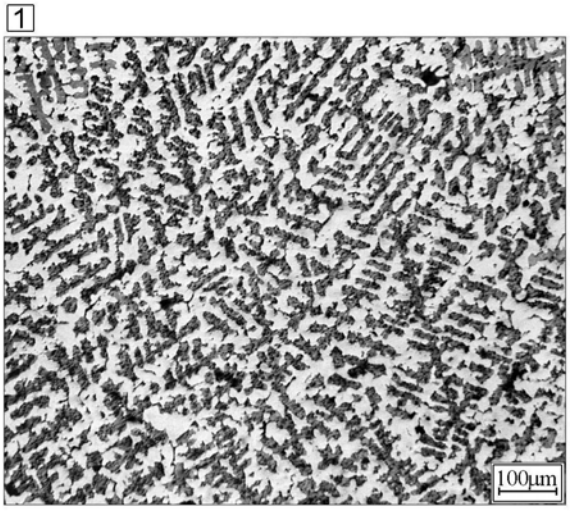

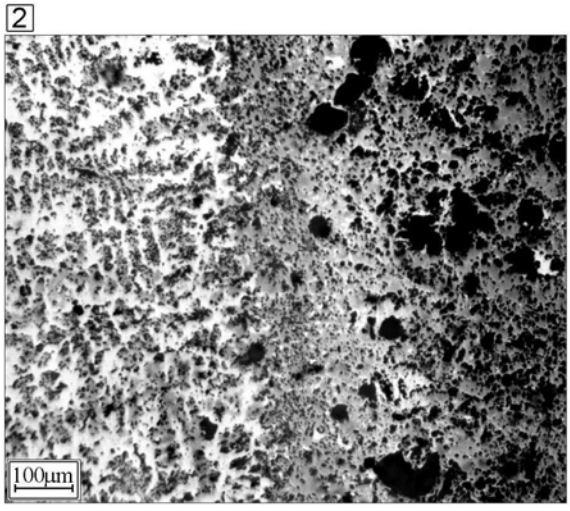

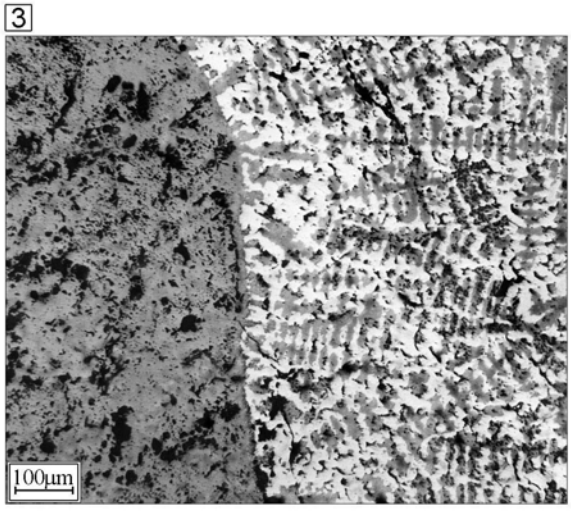

Fig. I - 29. Test 2200 °C, 100 s. Structure of melt

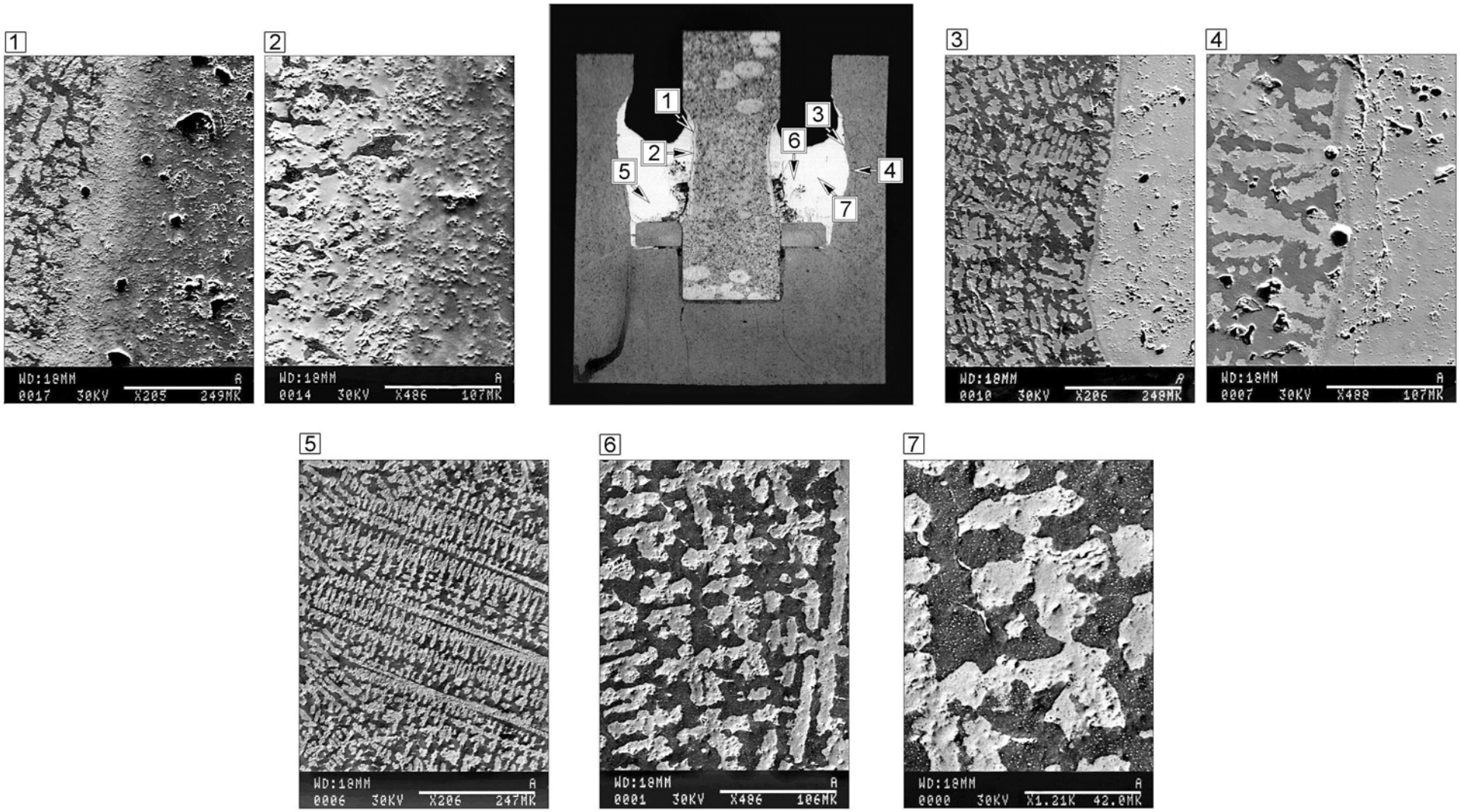

Fig. I - 30. Test 2200 °C, 100 s. Structure of melt (SEM)

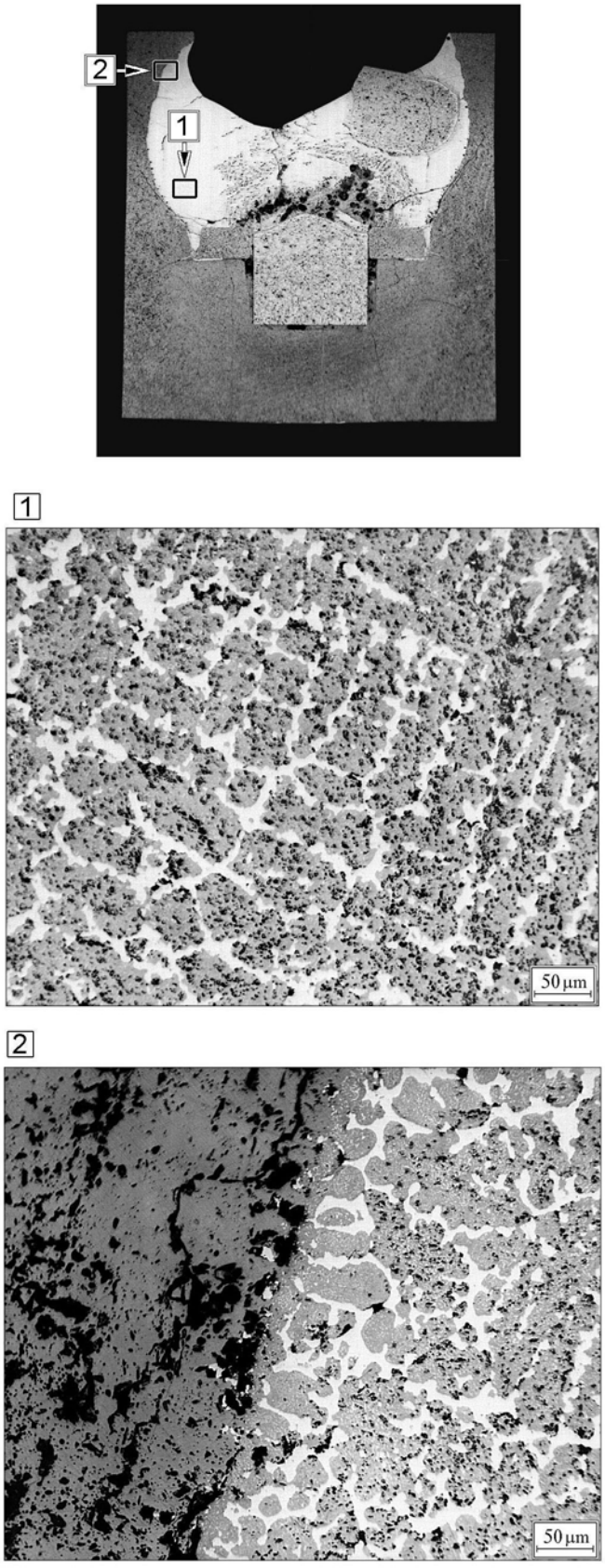

Fig. I - 31. Test 2200 °C, 180 s. Structure of melt

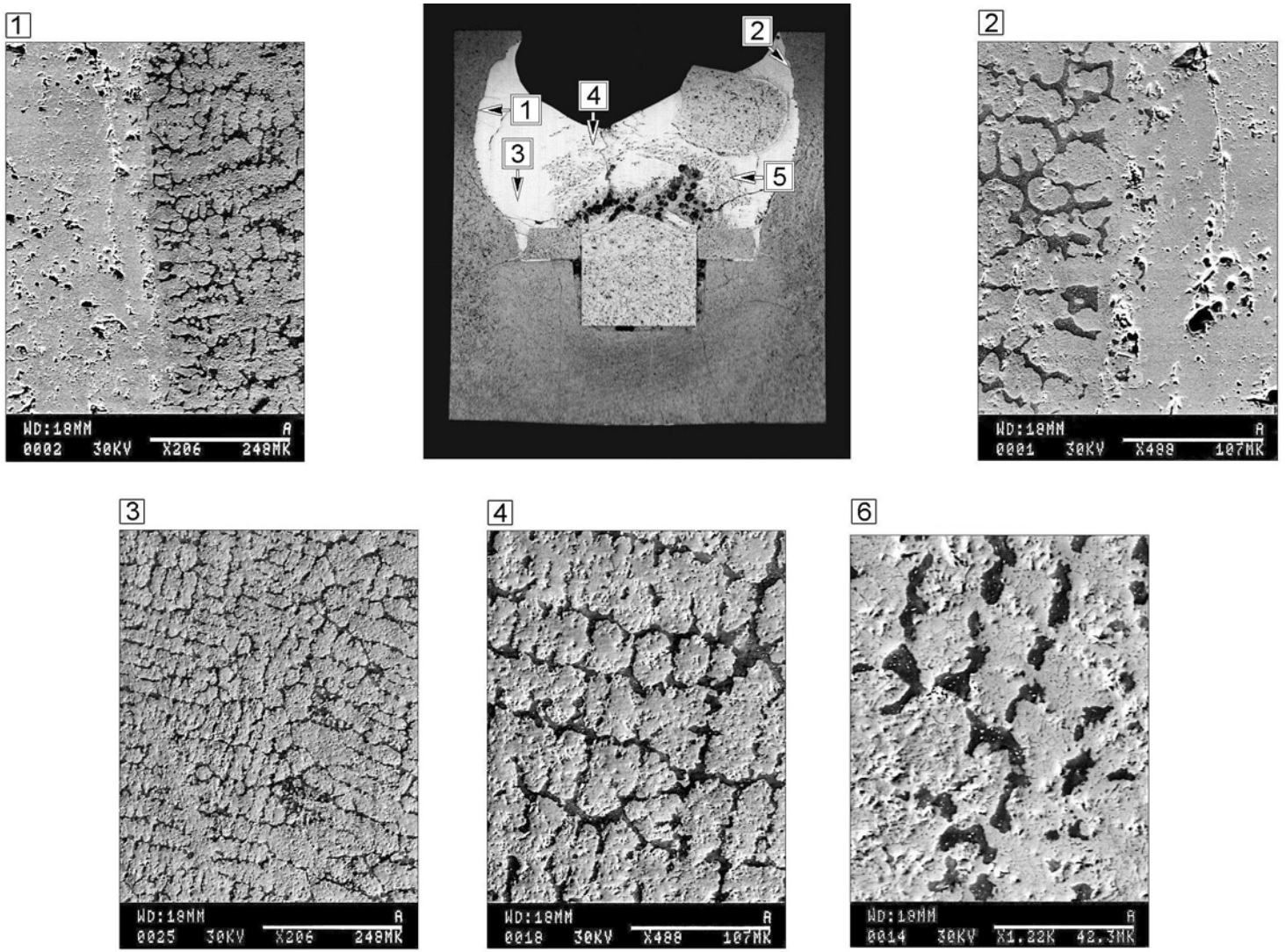

Fig. I - 32. Test 2200 °C, 180 s. Structure of melt (SEM)

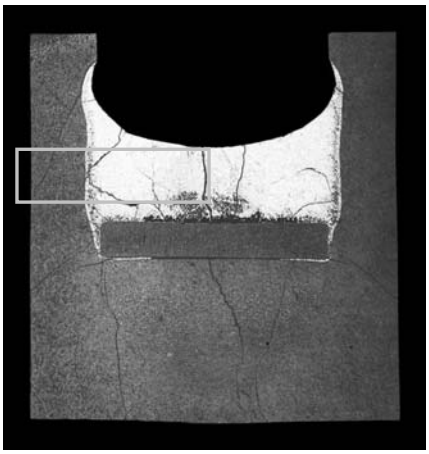

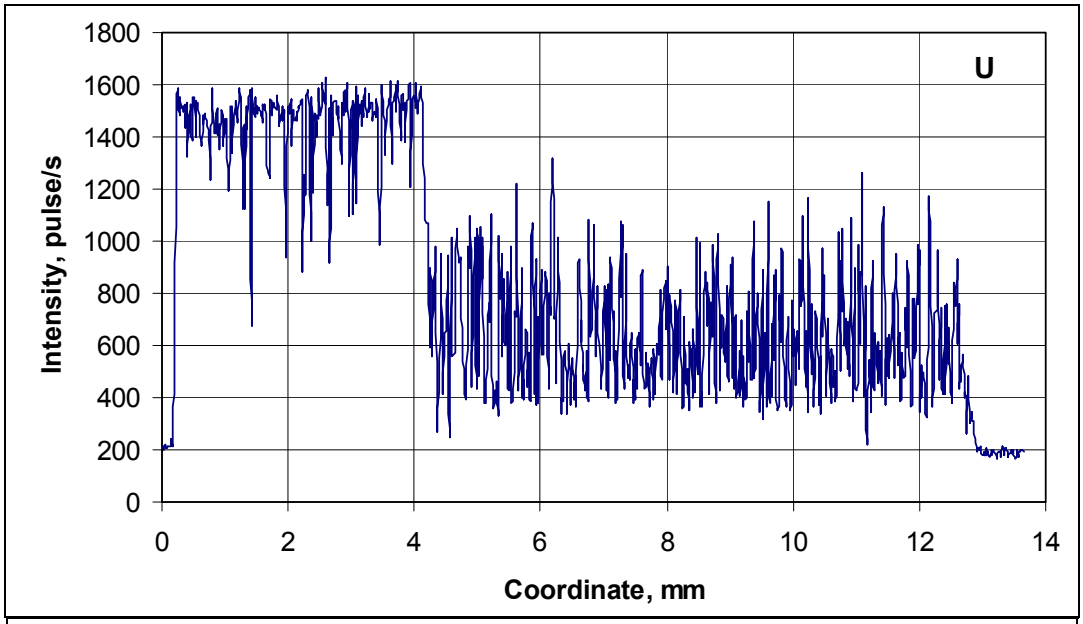

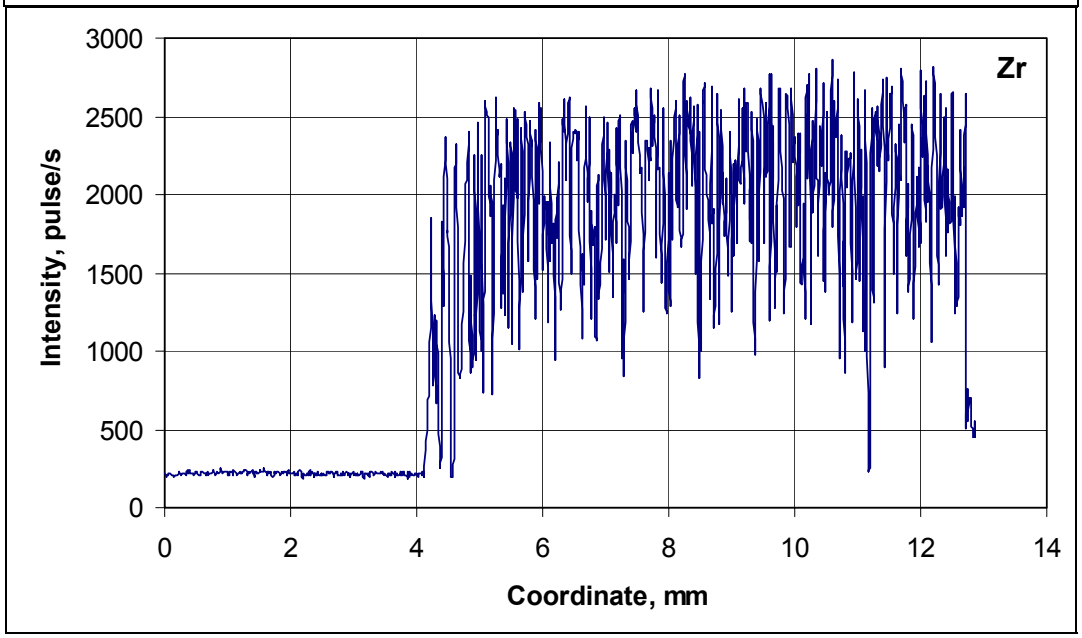

Fig. I - 33. Calibrating test 2100 °C, 600 s. Distribution of uranium and zirconium concentration in the melt

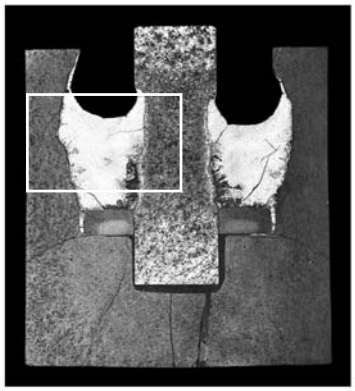

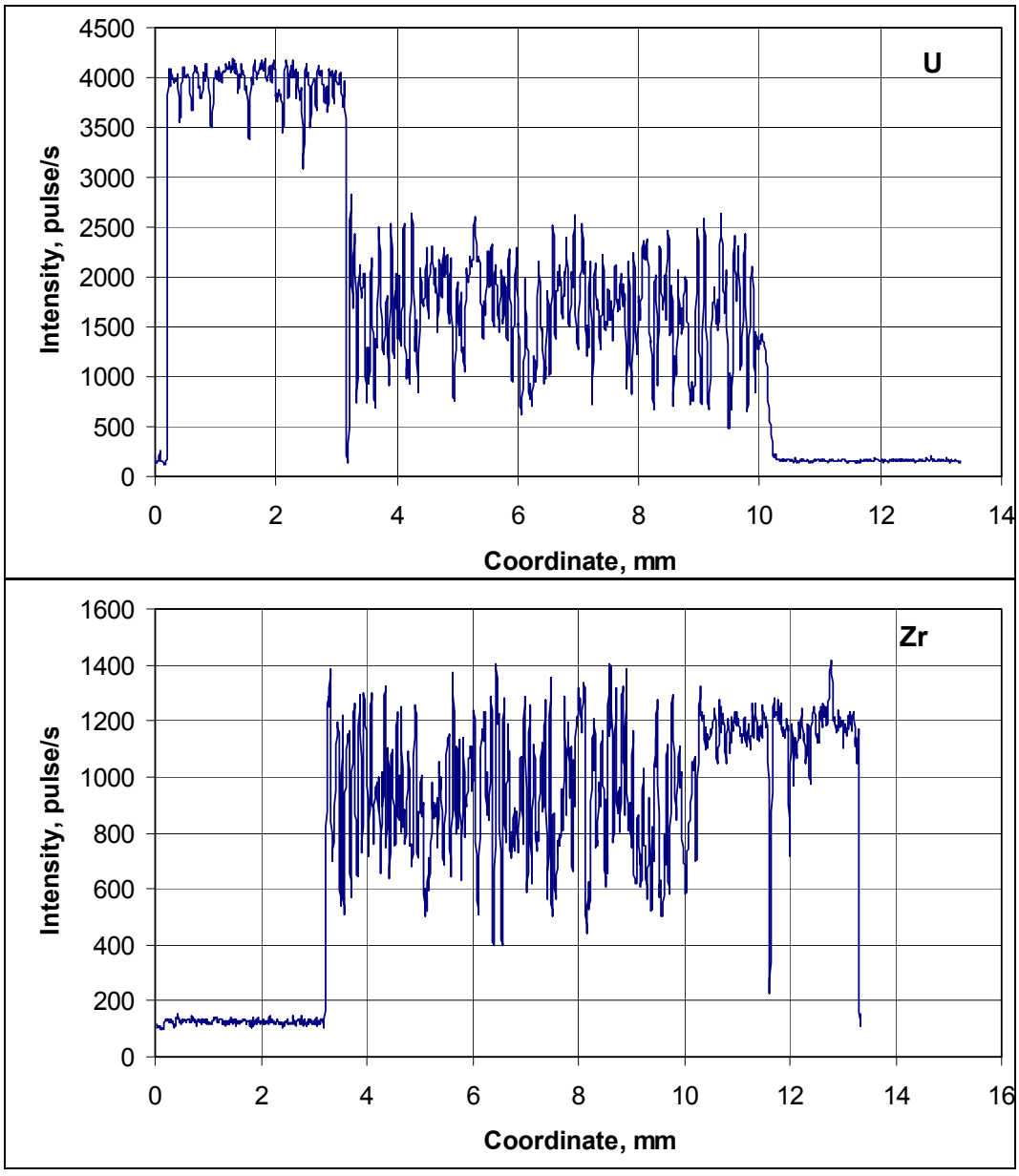

Fig. I - 34. Test 2100 °C, 100 s. Distribution of uranium and zirconium concentration in the melt

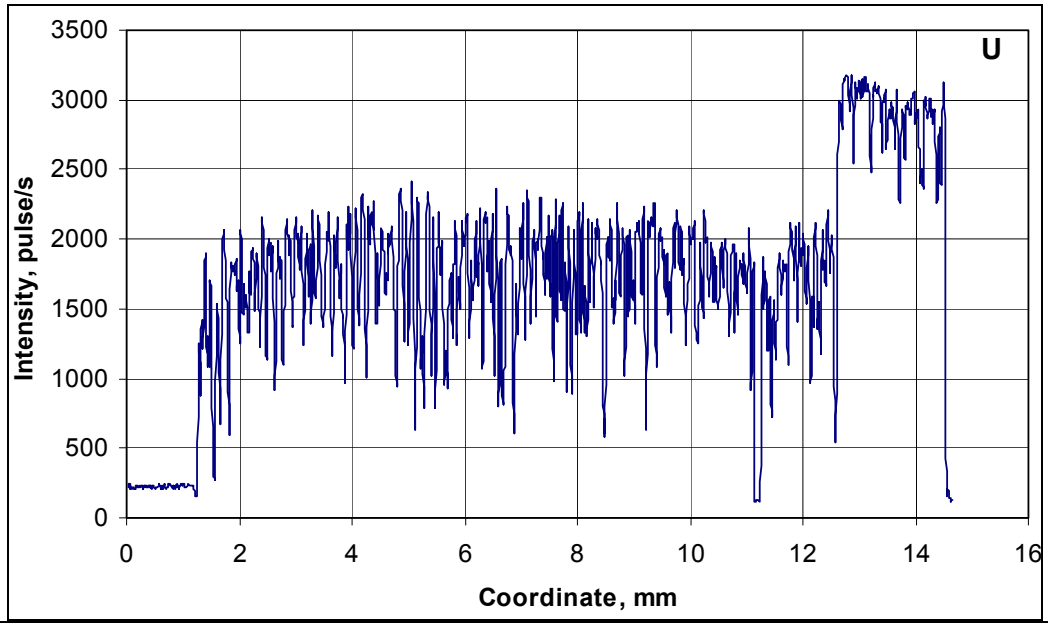

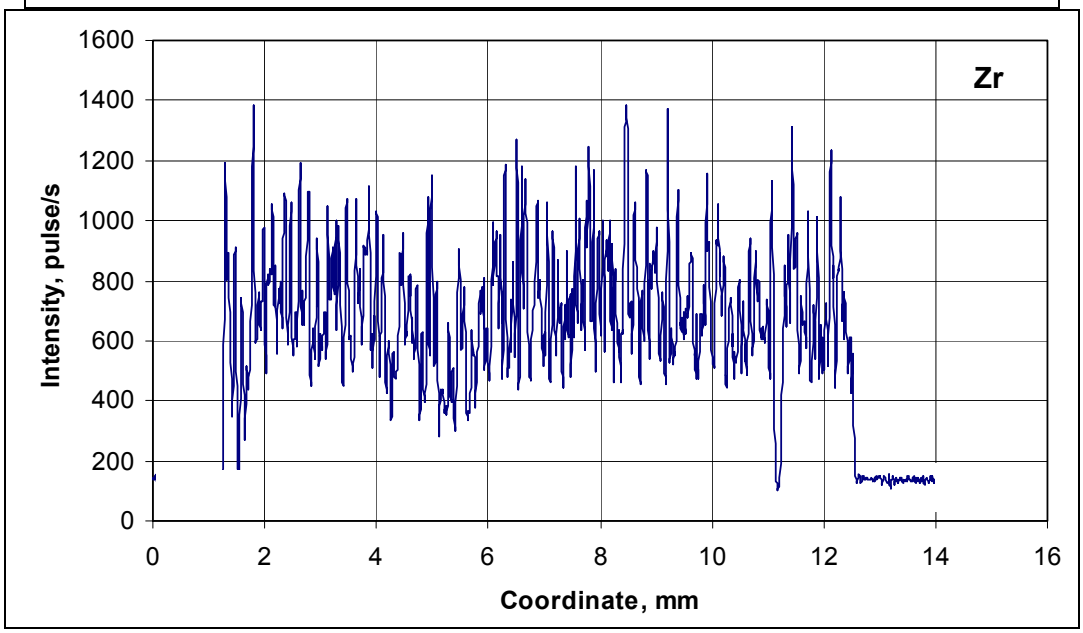

Fig. I - 35. Test 2100 °C, 200 s. Distribution of uranium and zirconium concentration in the melt

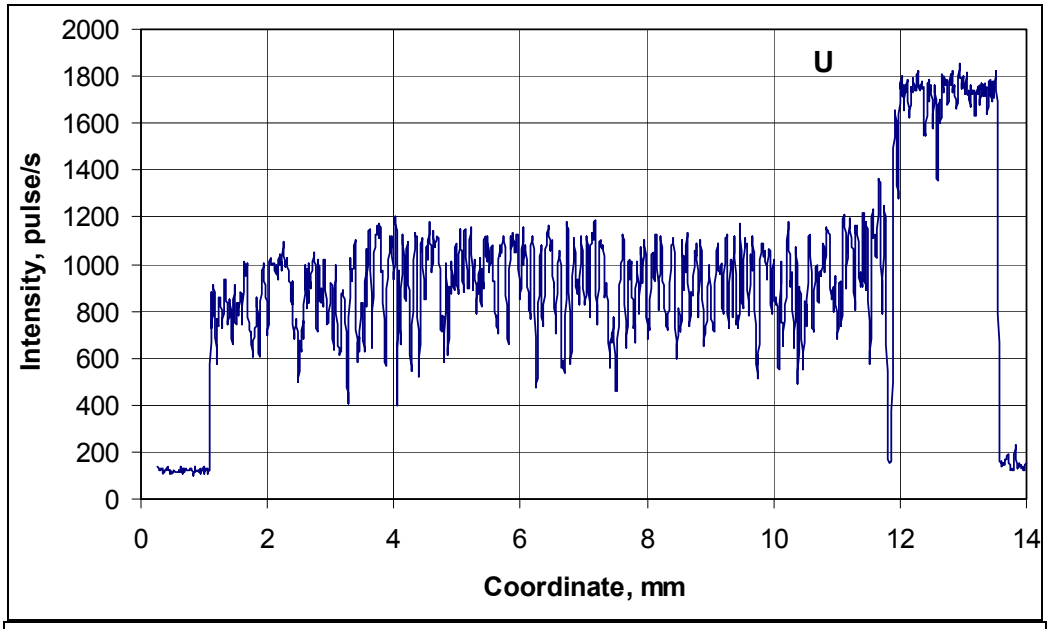

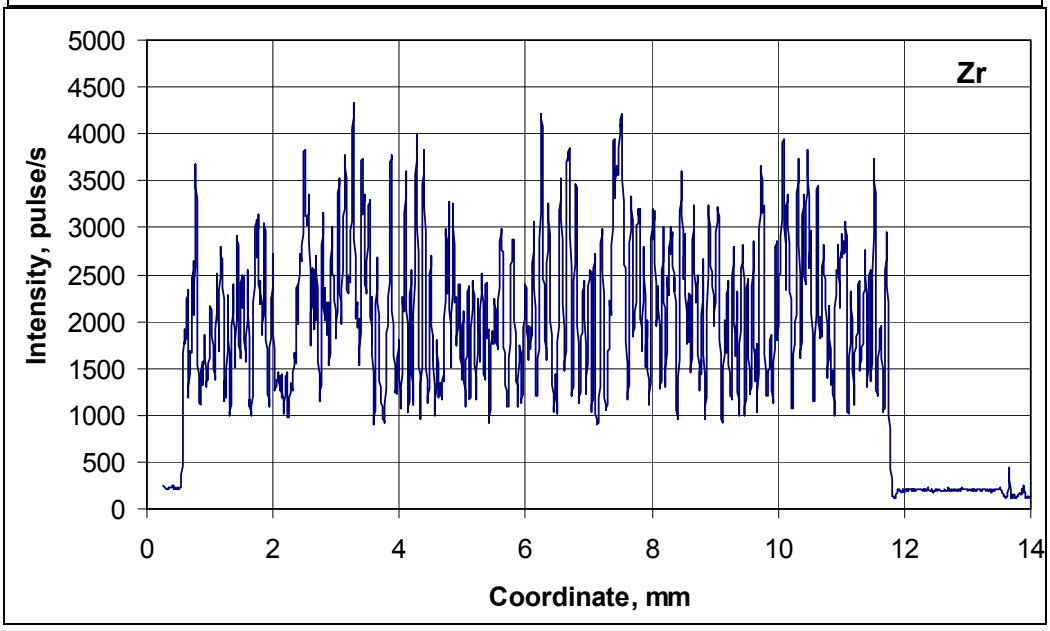

Fig. I - 36. Test 2100 °C, 300 s. Distribution of uranium and zirconium concentration in the melt

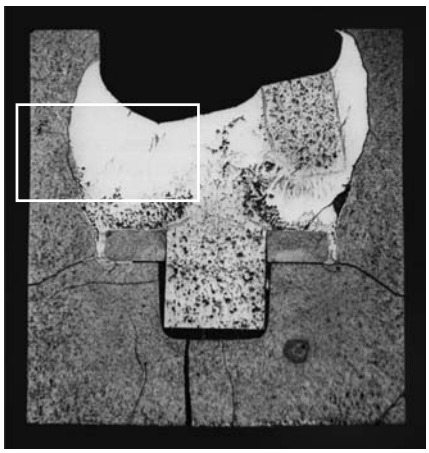

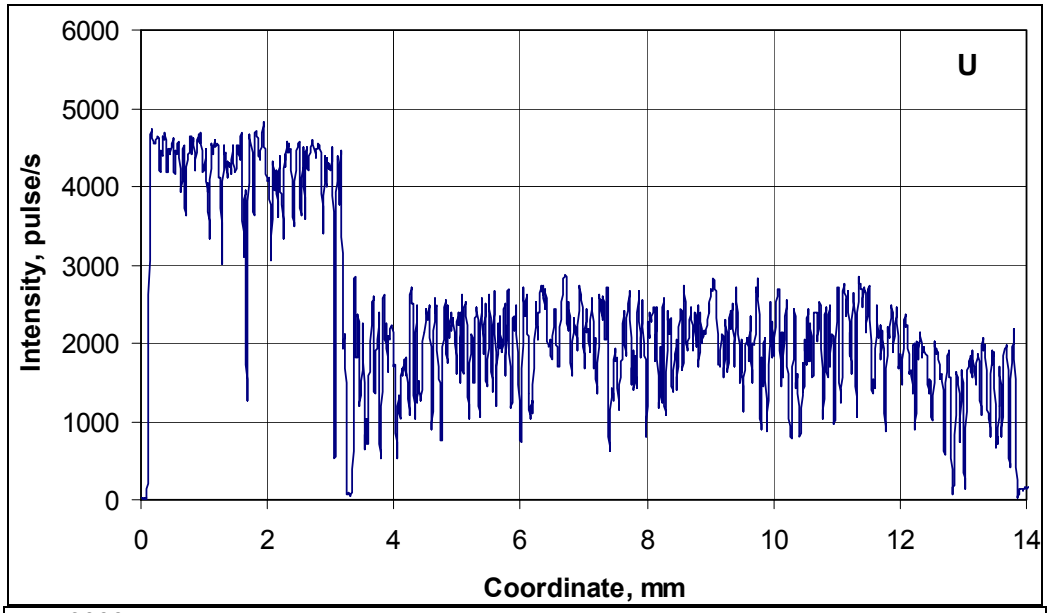

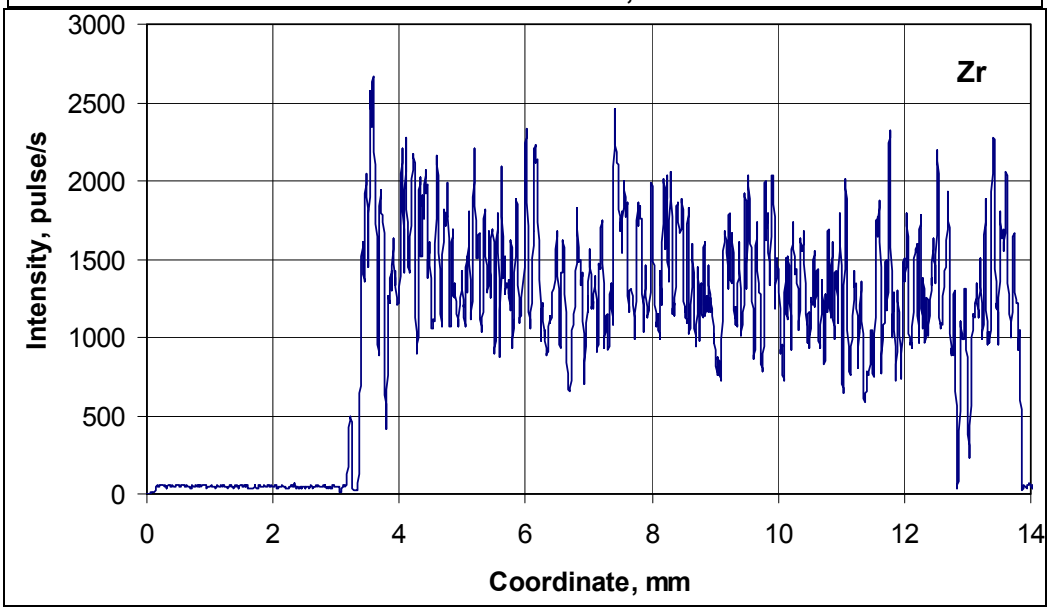

Fig. I - 37. Test 2100 °C, 400 s. Distribution of uranium and zirconium concentration in the melt

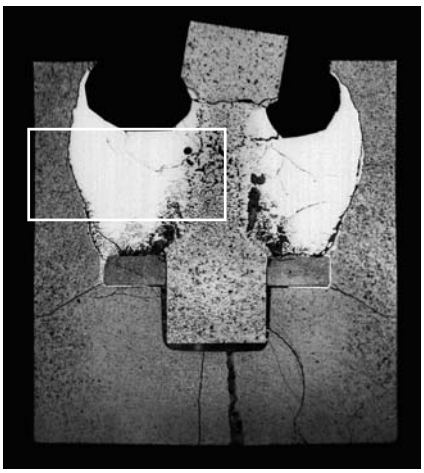

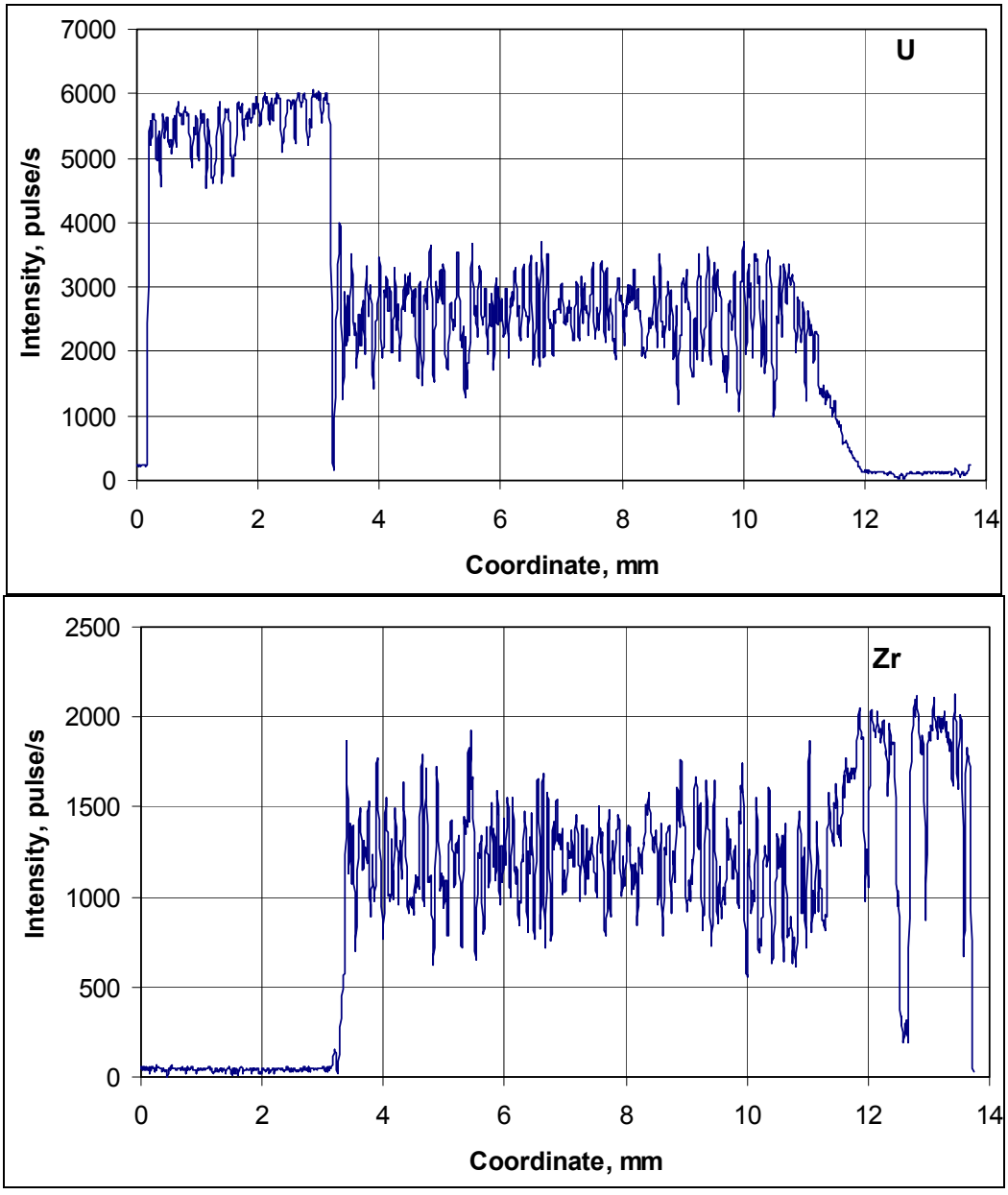

Fig. I - 38. Test 2100 °C, 500 s. Distribution of uranium and zirconium concentration in the melt

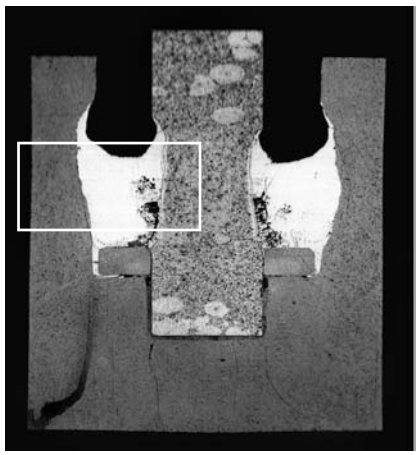

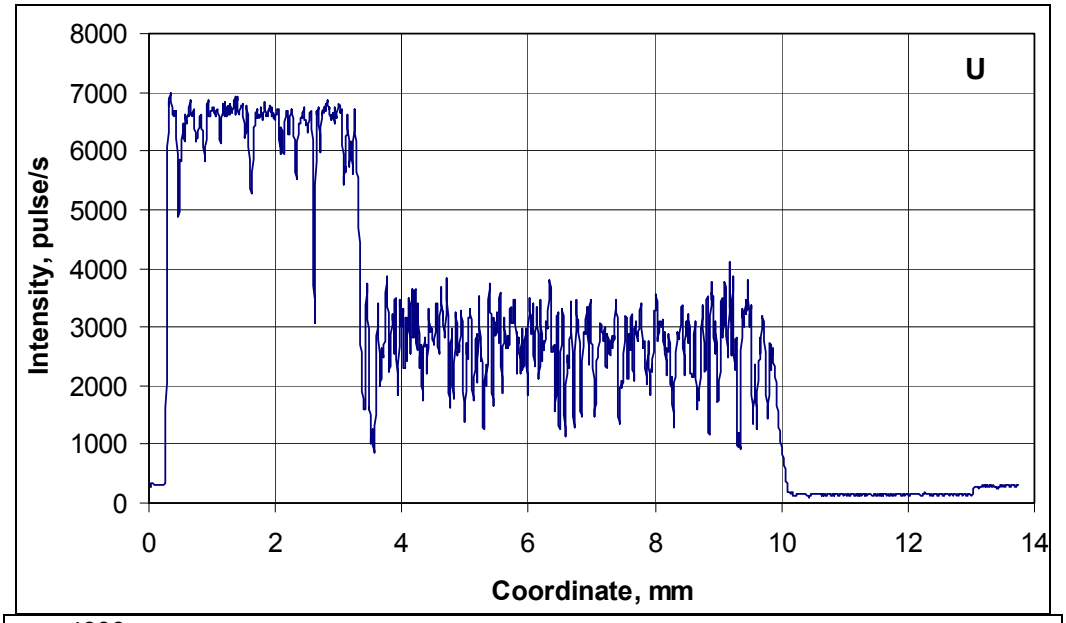

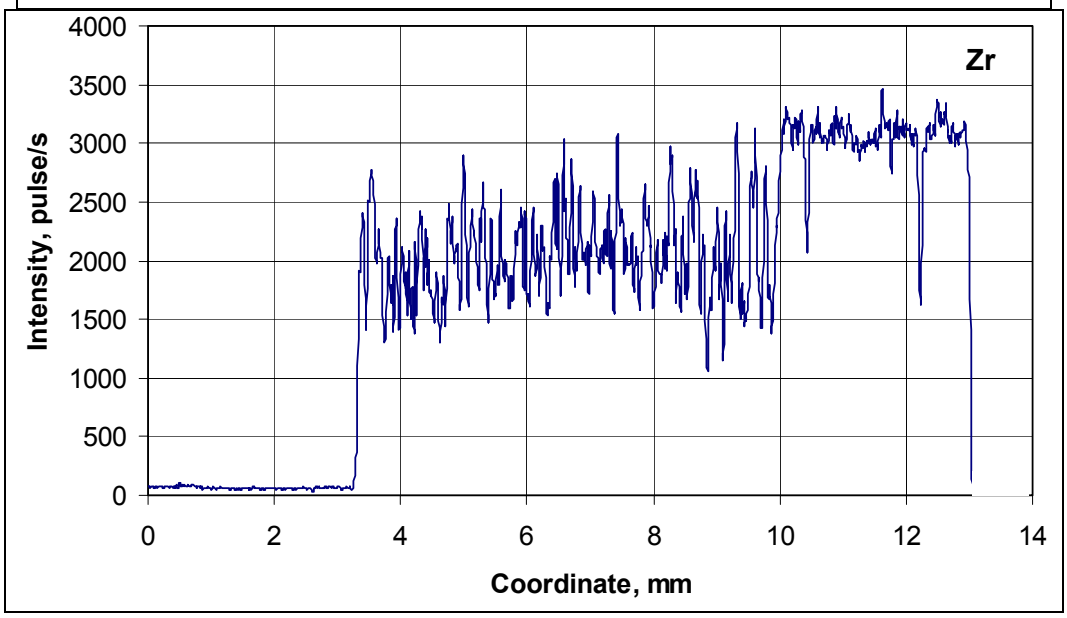

Fig. I - 39. Test 2200 °C, 100 s. Distribution of uranium and zirconium concentration in the melt

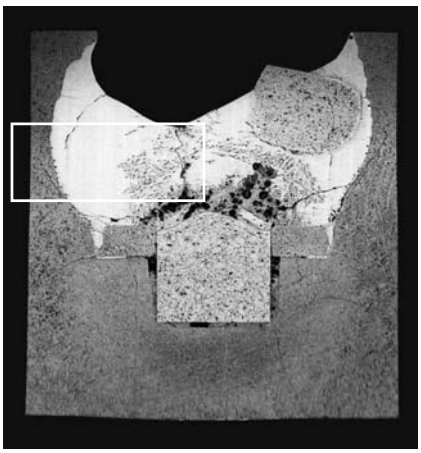

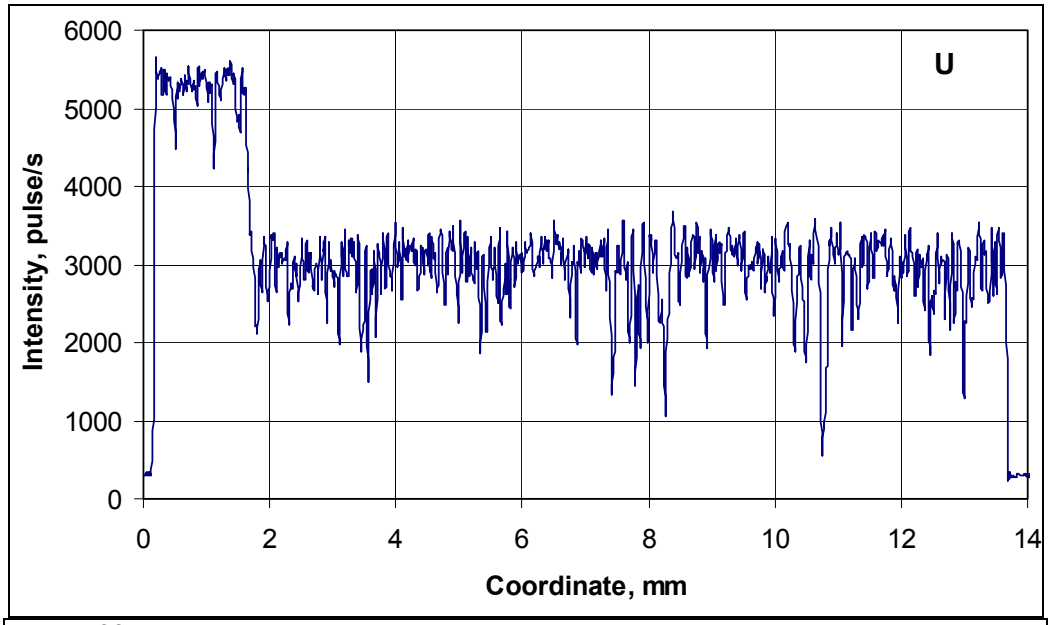

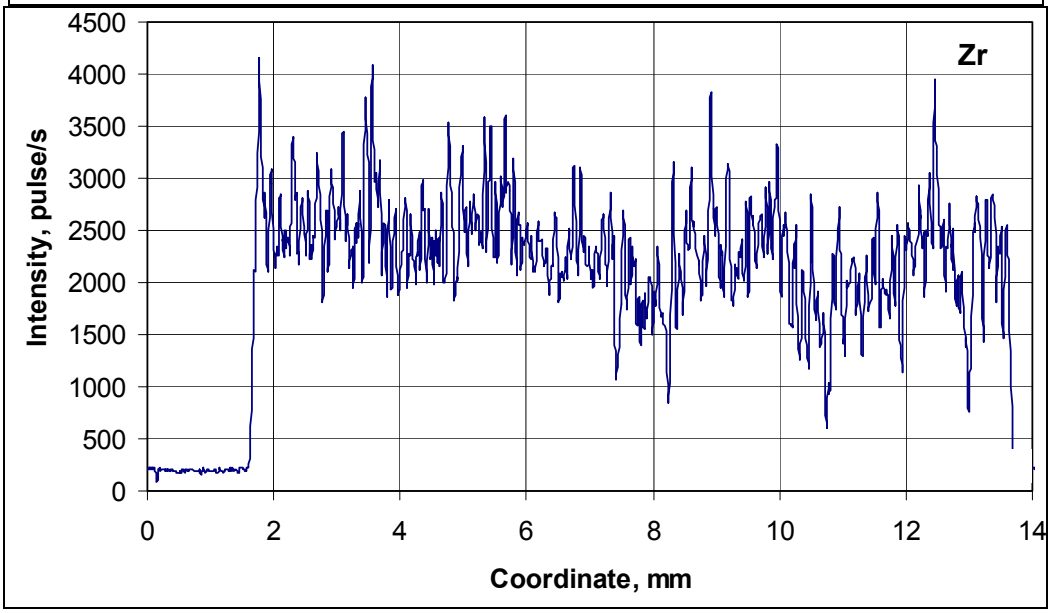

Fig. I - 40. Test 2200 °C, 180 s. Distribution of uranium and zirconium concentration in the melt

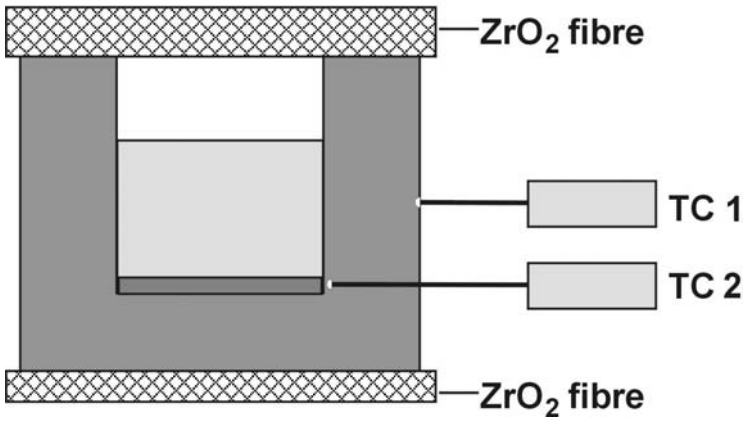

a – calibrating test

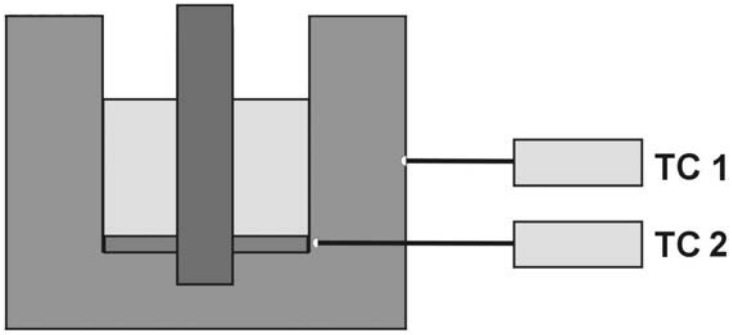

b – without heat insulation

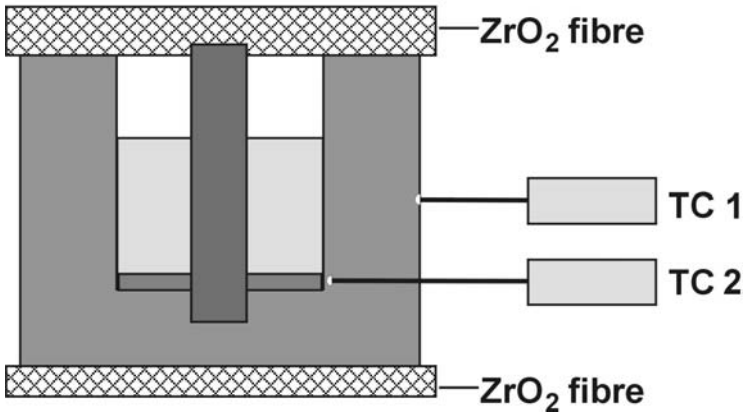

c – with heat insulation

Fig. I - 41. Types of tests realized at the second series

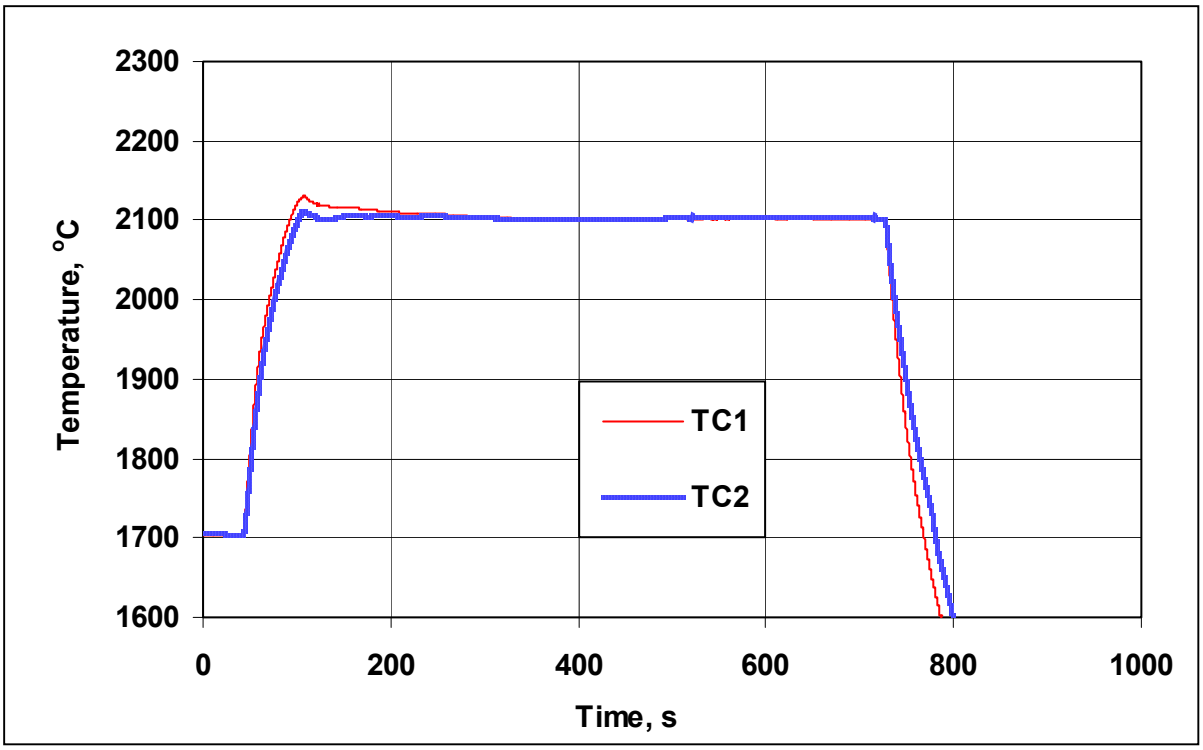

Fig. I - 42. Calibrating test 2100 °C, 600 s (with heat-insulation). Specimen appearance and test regime

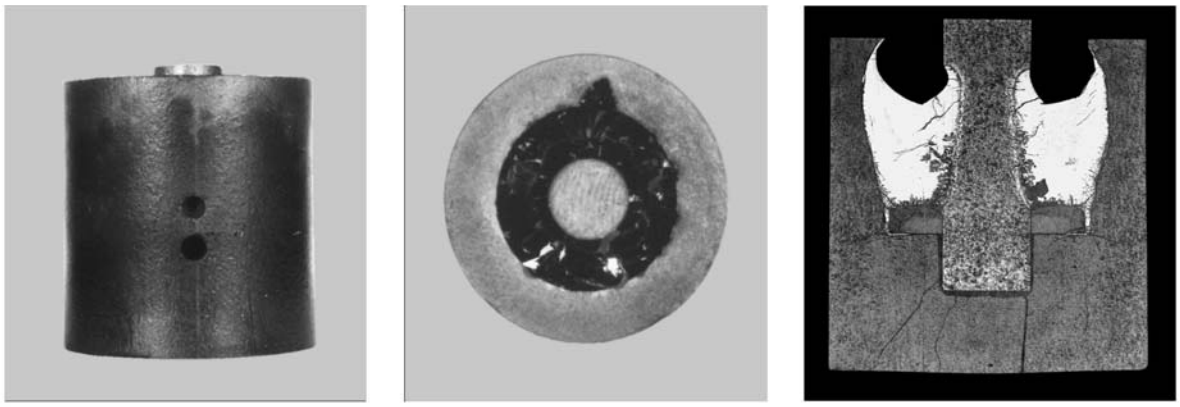

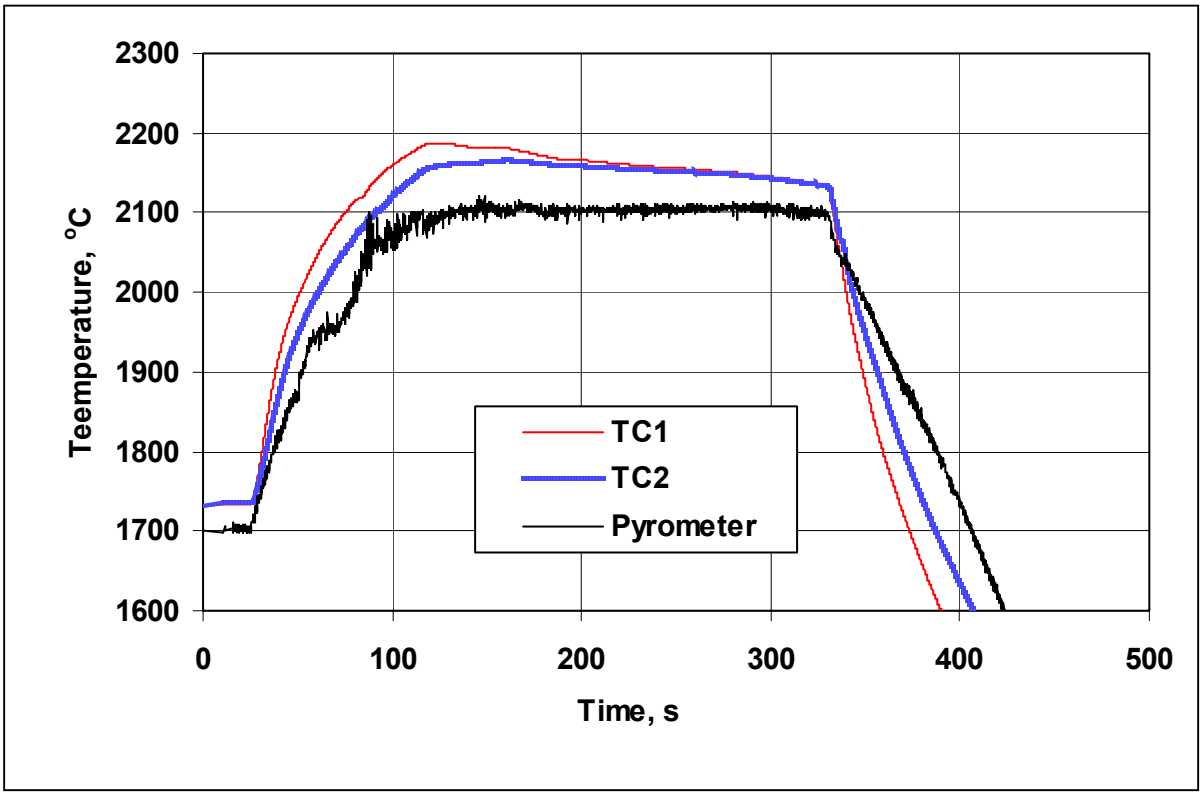

Fig. I - 43. Test 2100 °C, 200 s (with "deep" thermocouple). Specimen appearance and test regime

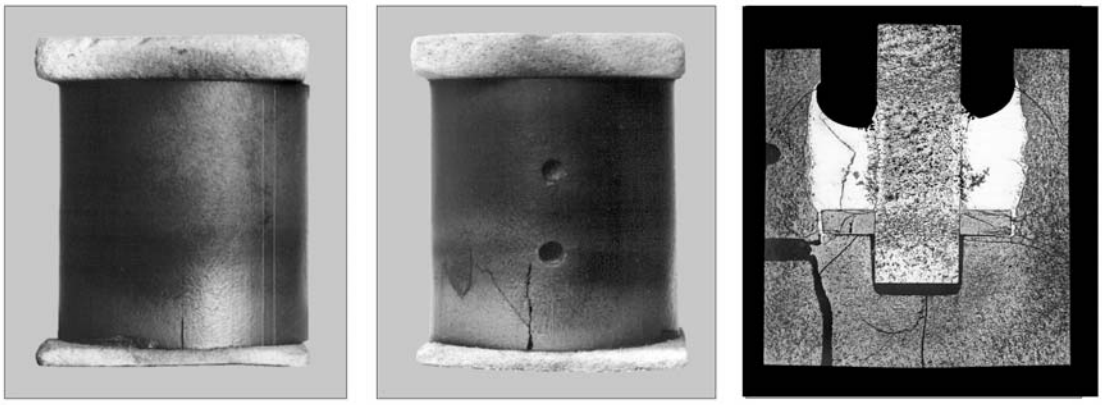

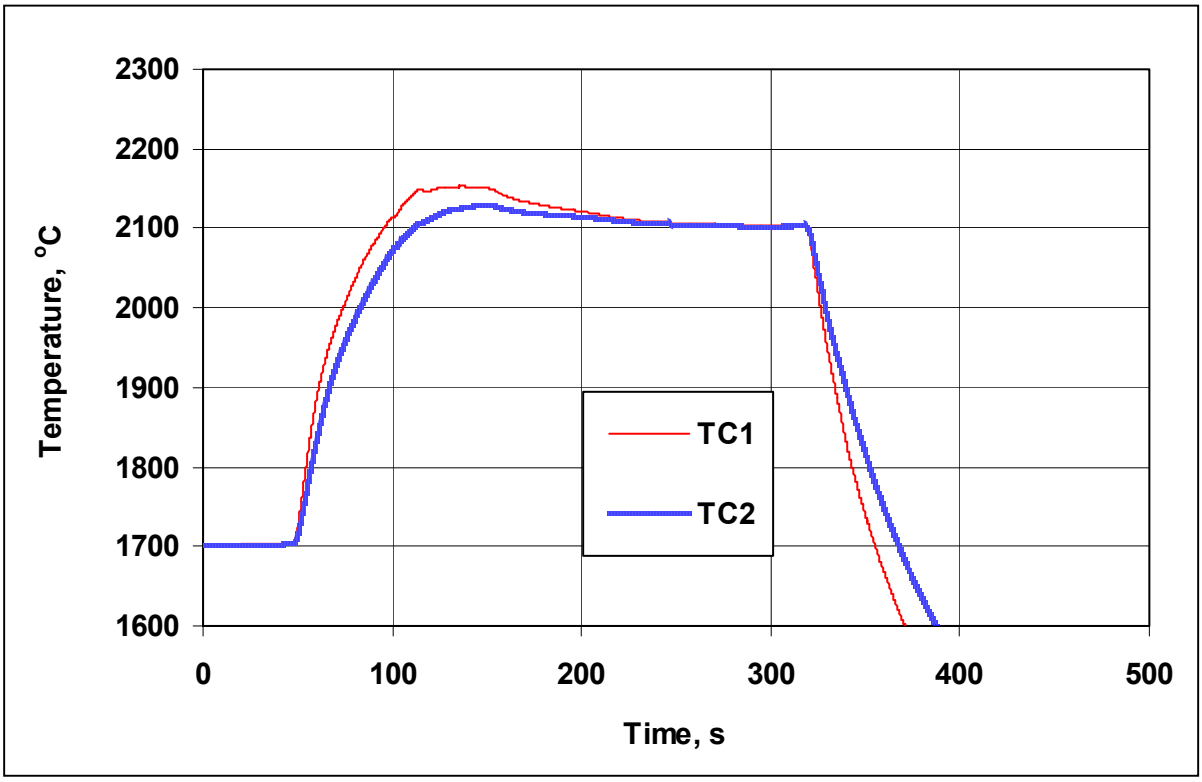

Fig. I - 44. Test 2100 °C, 200 s (with heat-insulation). Specimen appearance and test regime

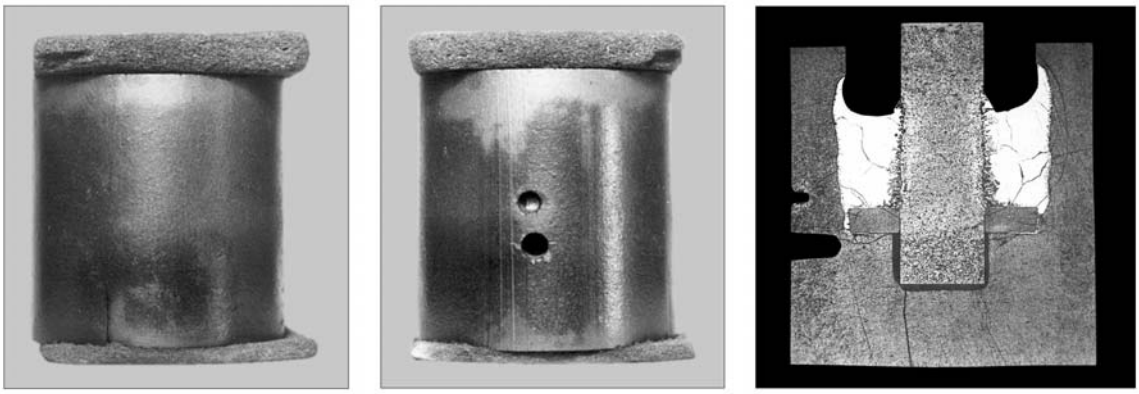

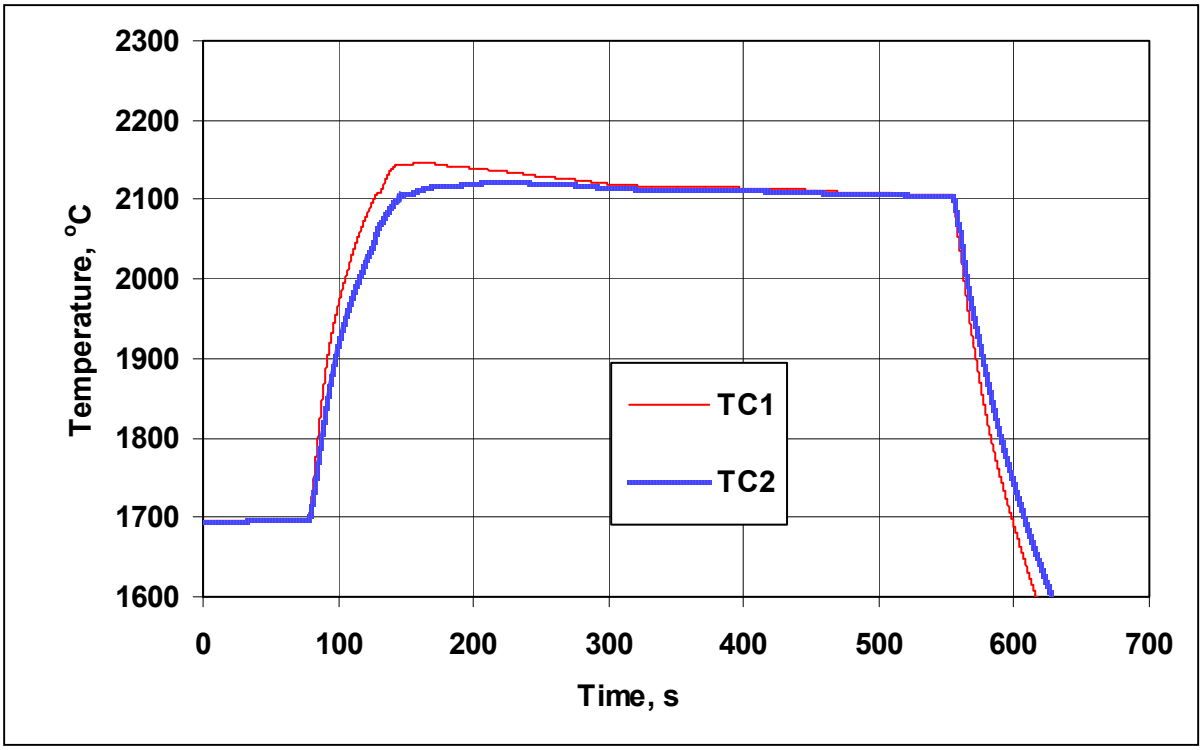

Fig. I - 45. Test 2100 °C, 400 s (with heat-insulation). Specimen appearance and test regime

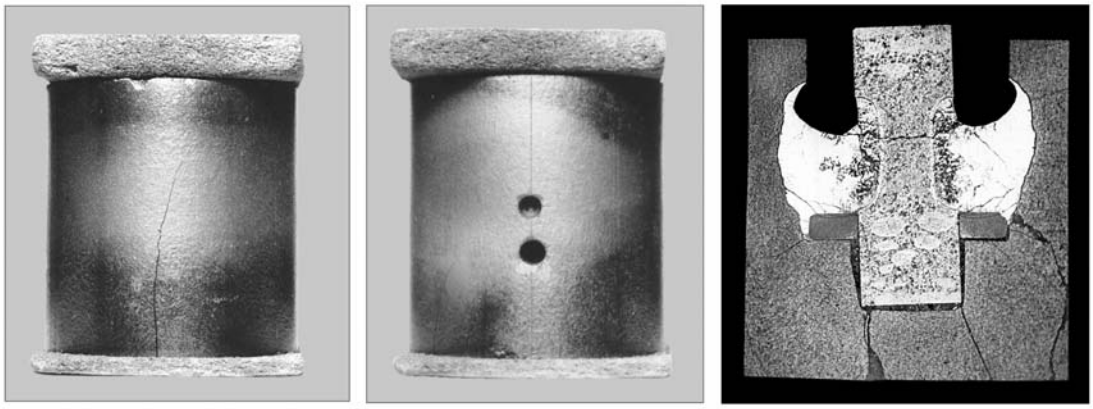

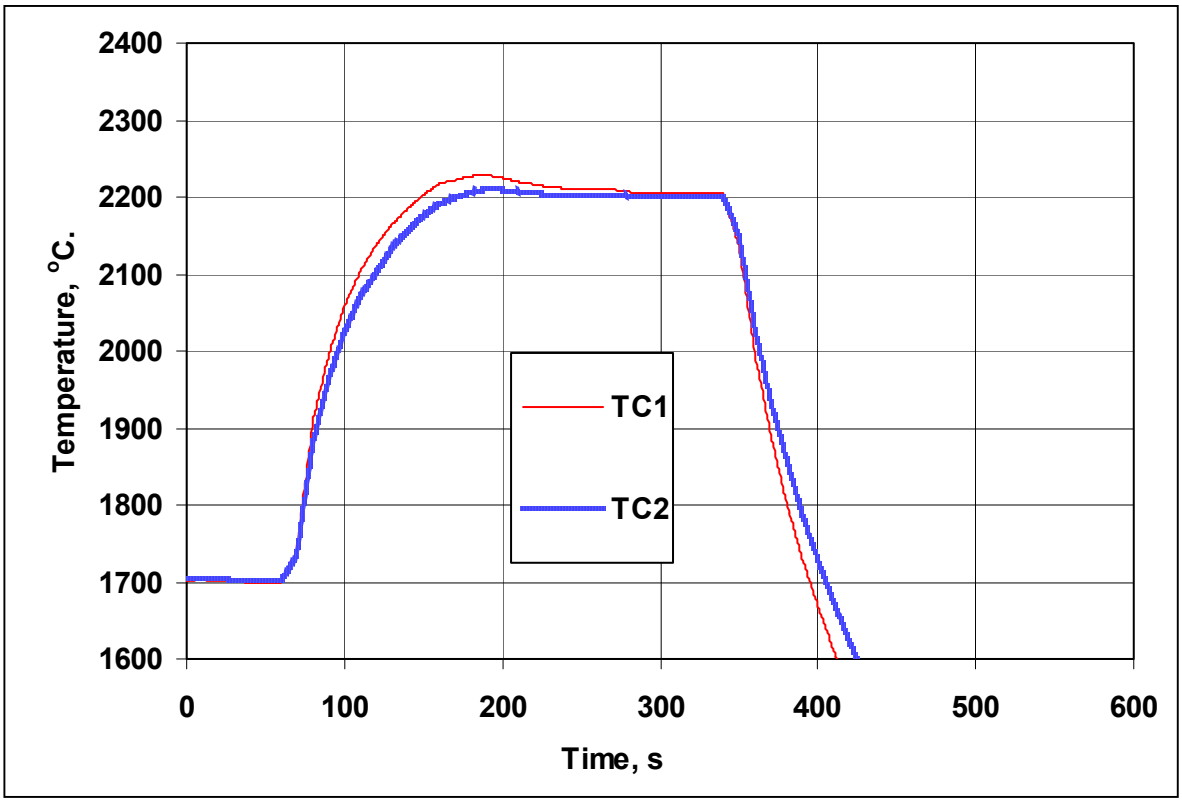

Fig. I - 46. Test 2200 °C, 180 s (with heat-insulation). Specimen appearance and test regime

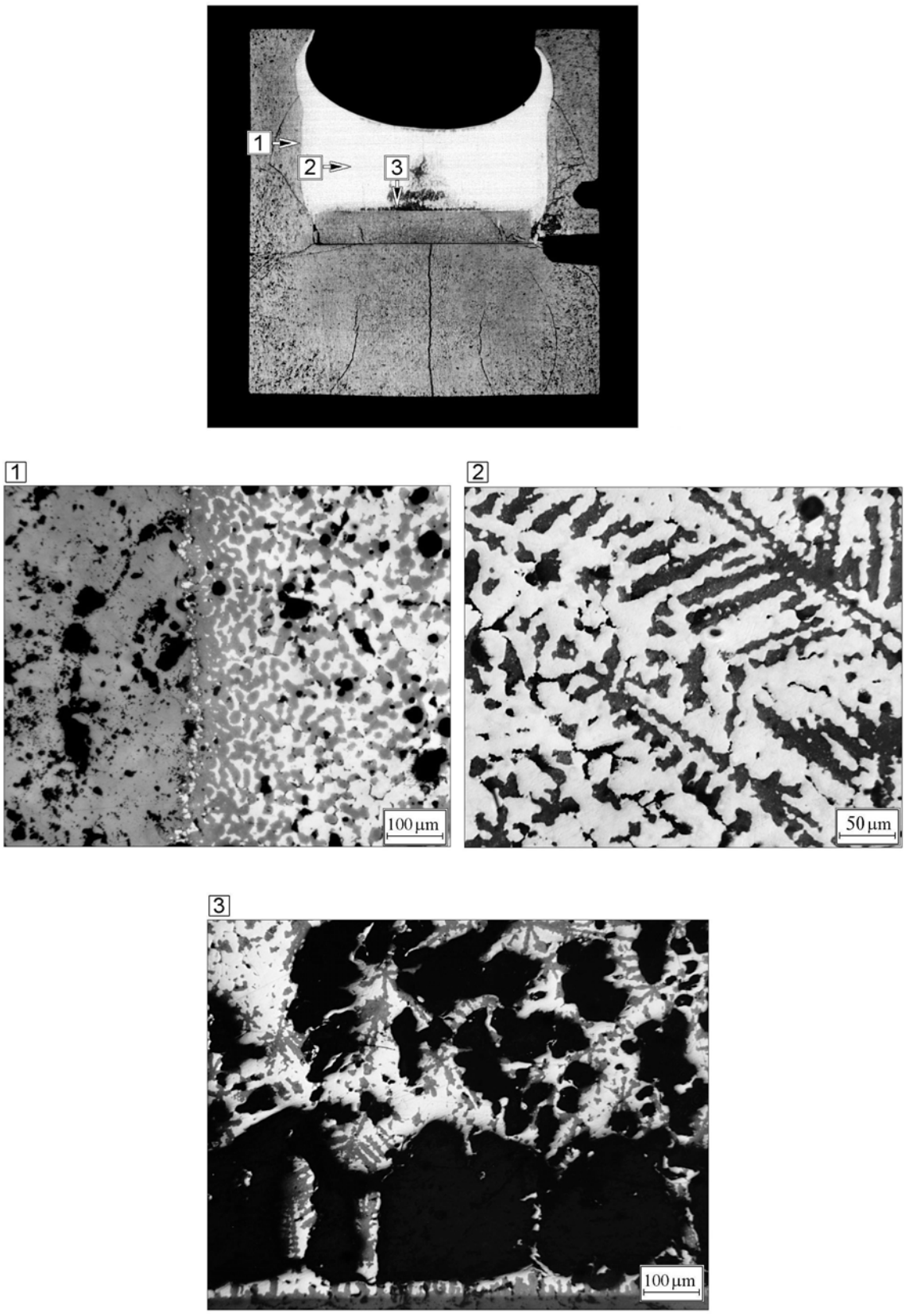

Fig. I - 47. Calibrating test 2100 °C, 600 s (with heat insulation). Structure of melt

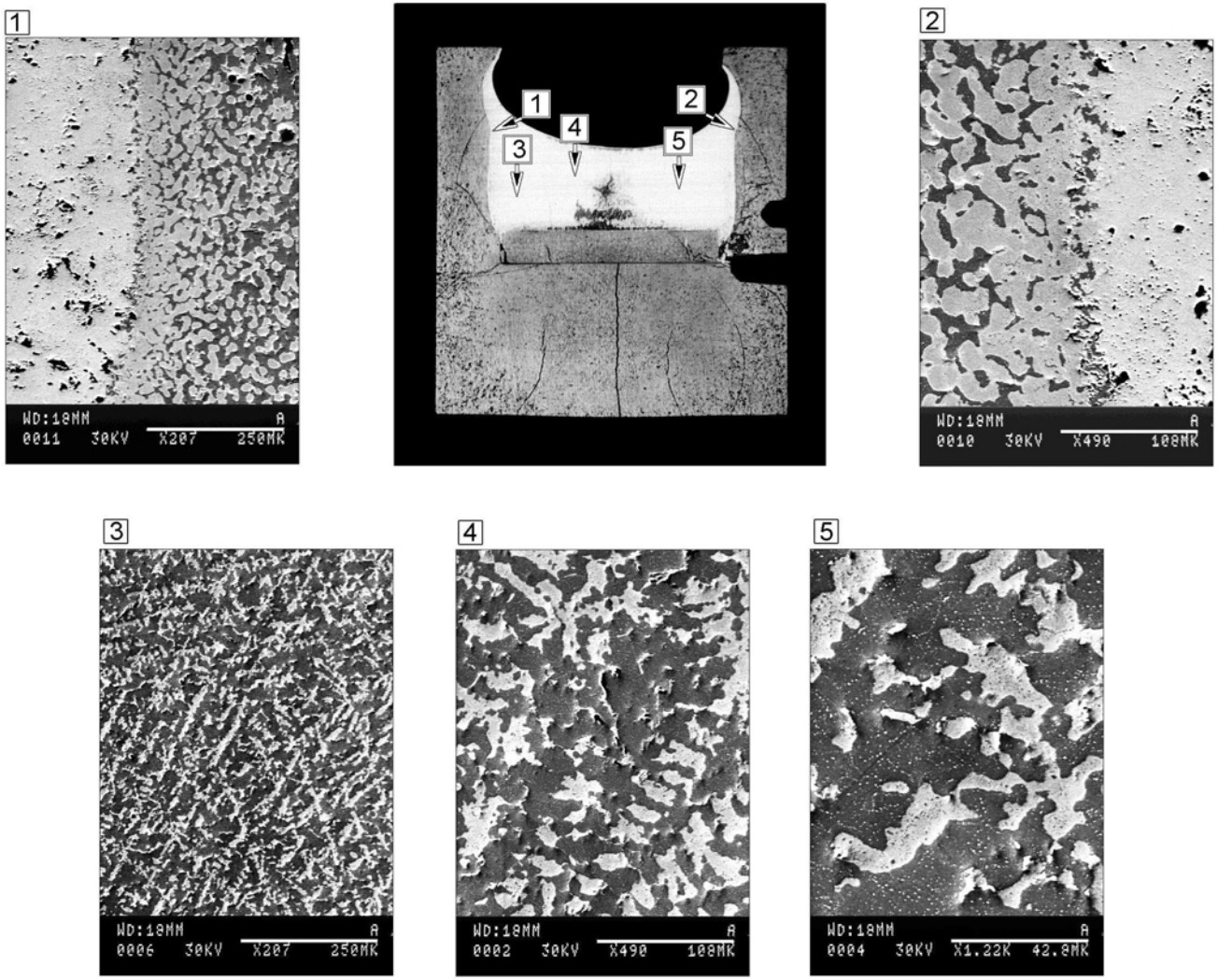

Fig. I - 48. Calibrating test 2100 °C, 600 s (with heat insulation). Structure of melt (SEM)

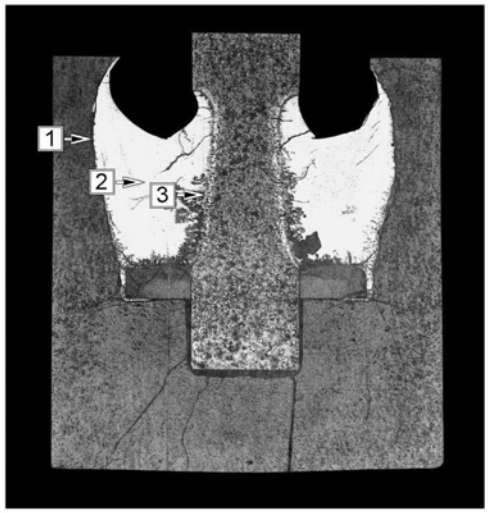

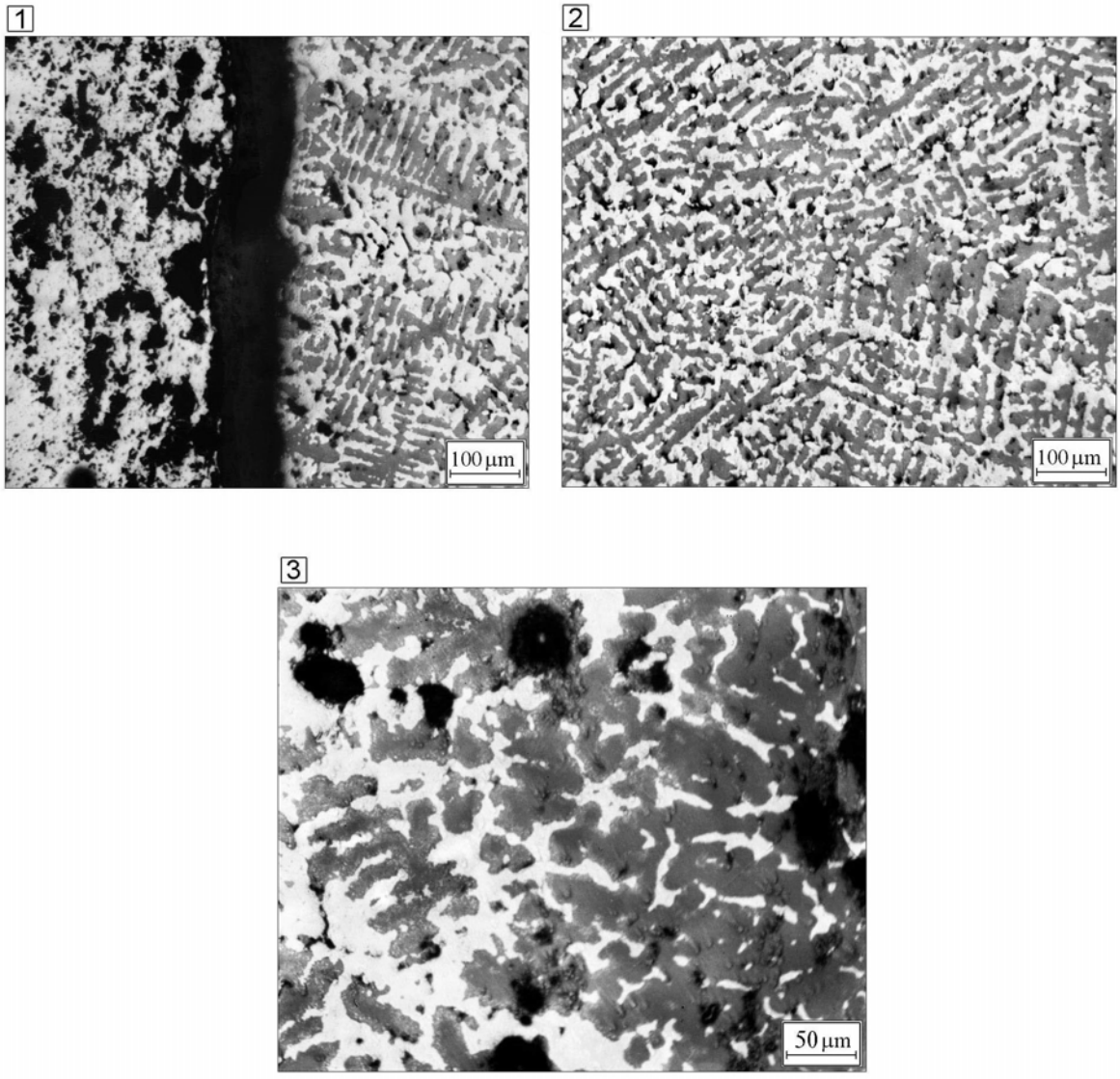

Fig. I - 49. Test 2100 °C, 200 s (with "deep" thermocouple). Structure of melt

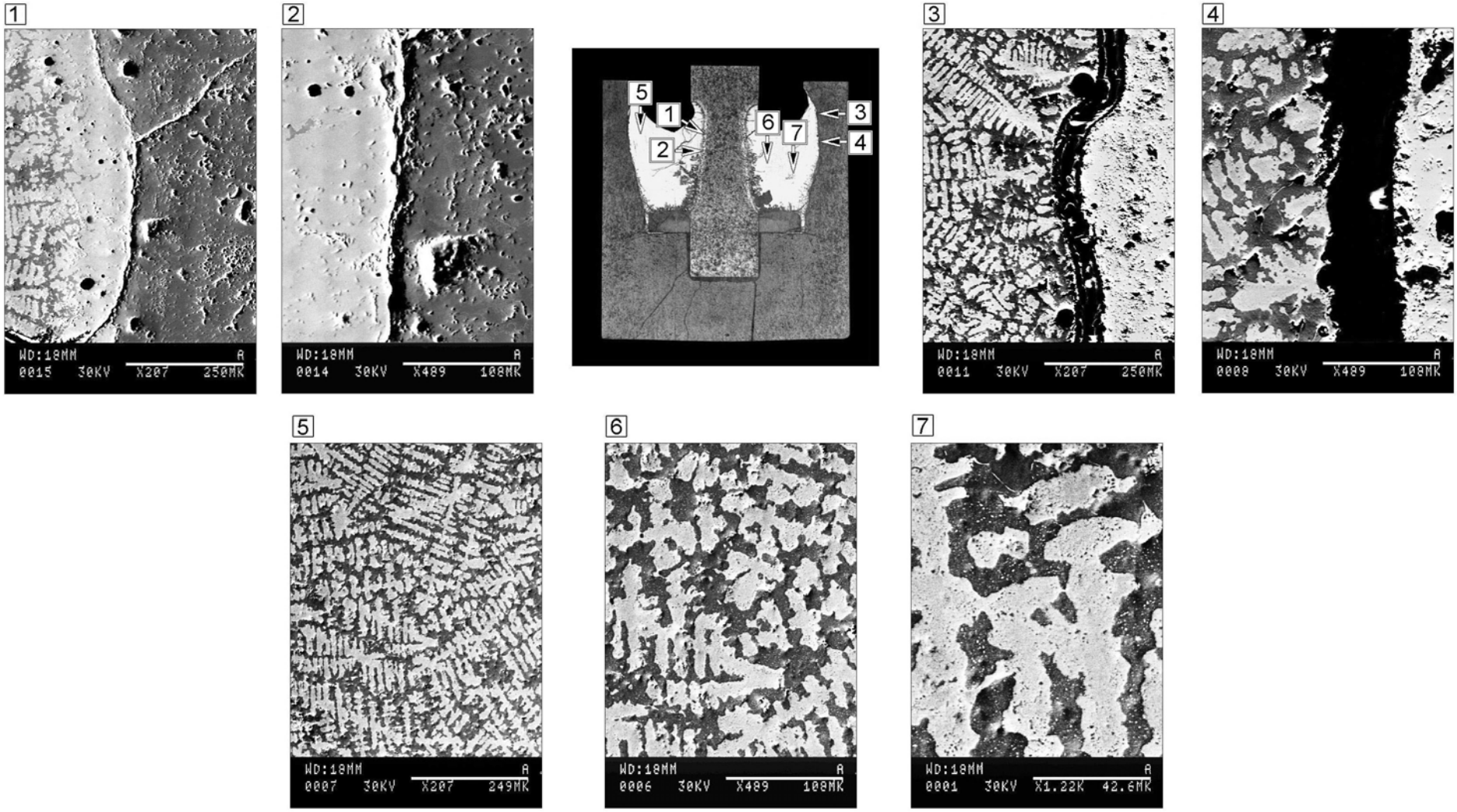

Fig. I - 50. Test 2100 °C, 200 s (with "deep" thermocouple). Structure of melt (SEM)

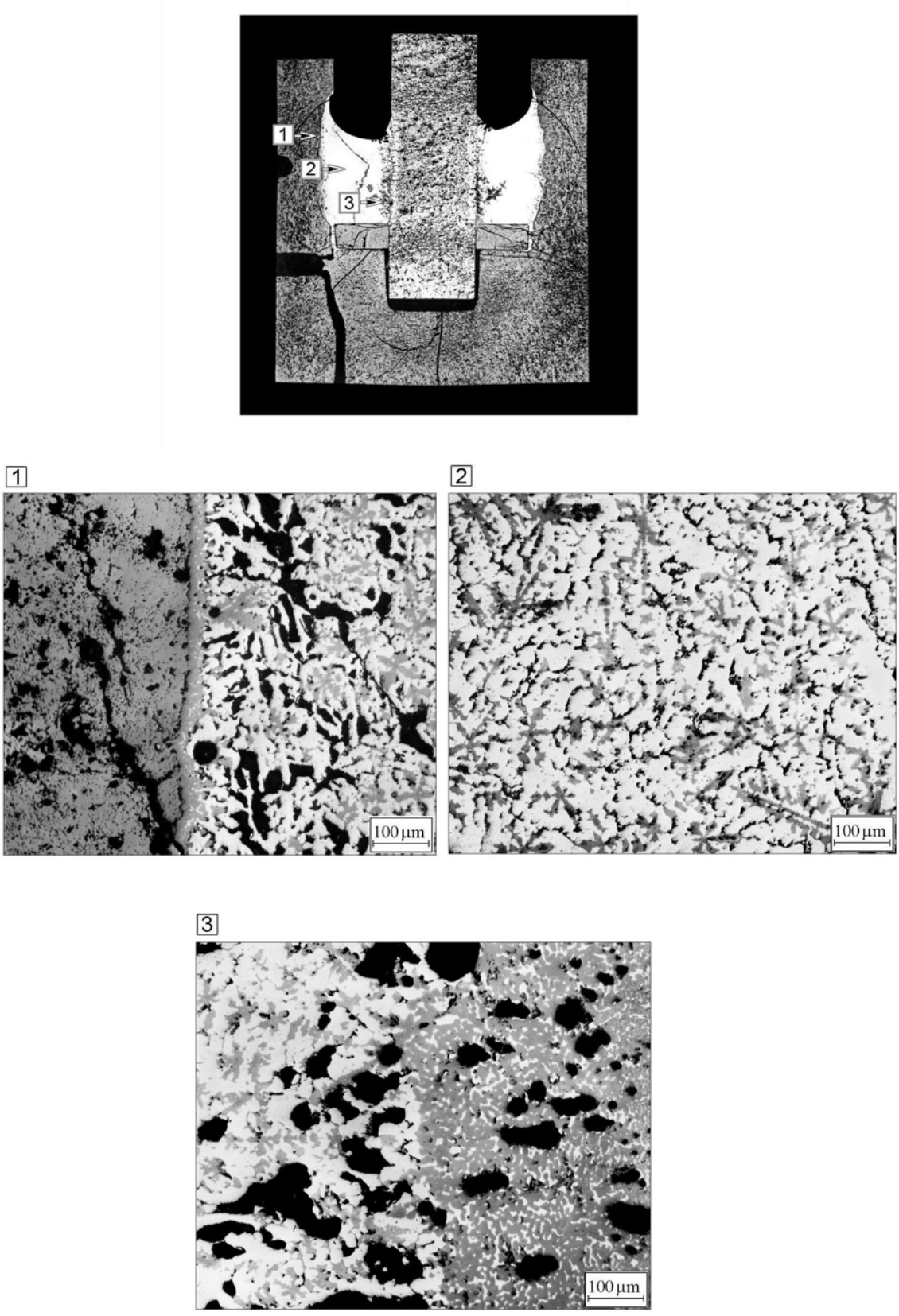

Fig. I - 51. Test 2100 °C, 200 s (with heat insulation). Structure of melt

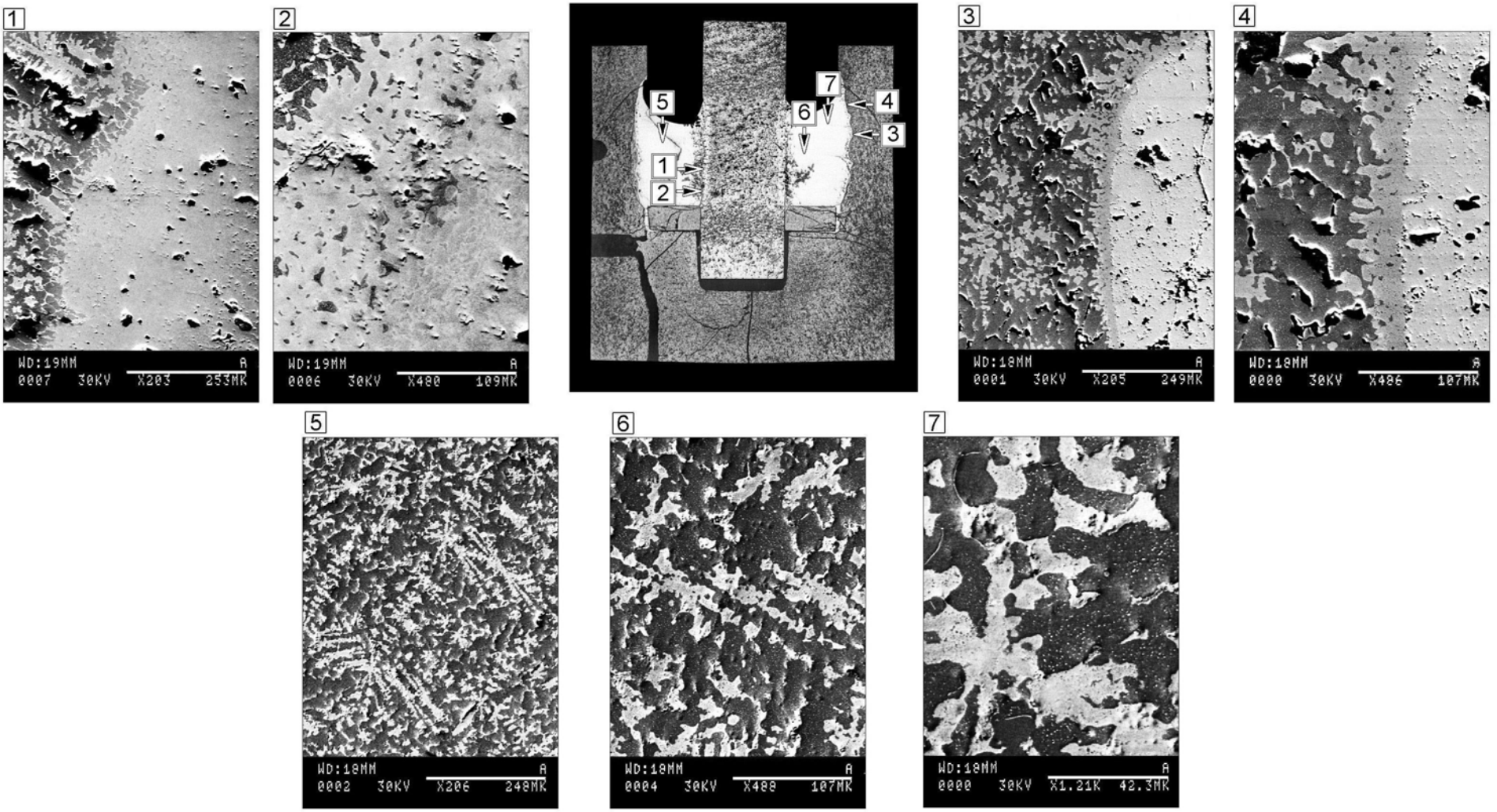

Fig. I - 52. Test 2100 °C, 200 s (with heat insulation). Structure of melt (SEM)

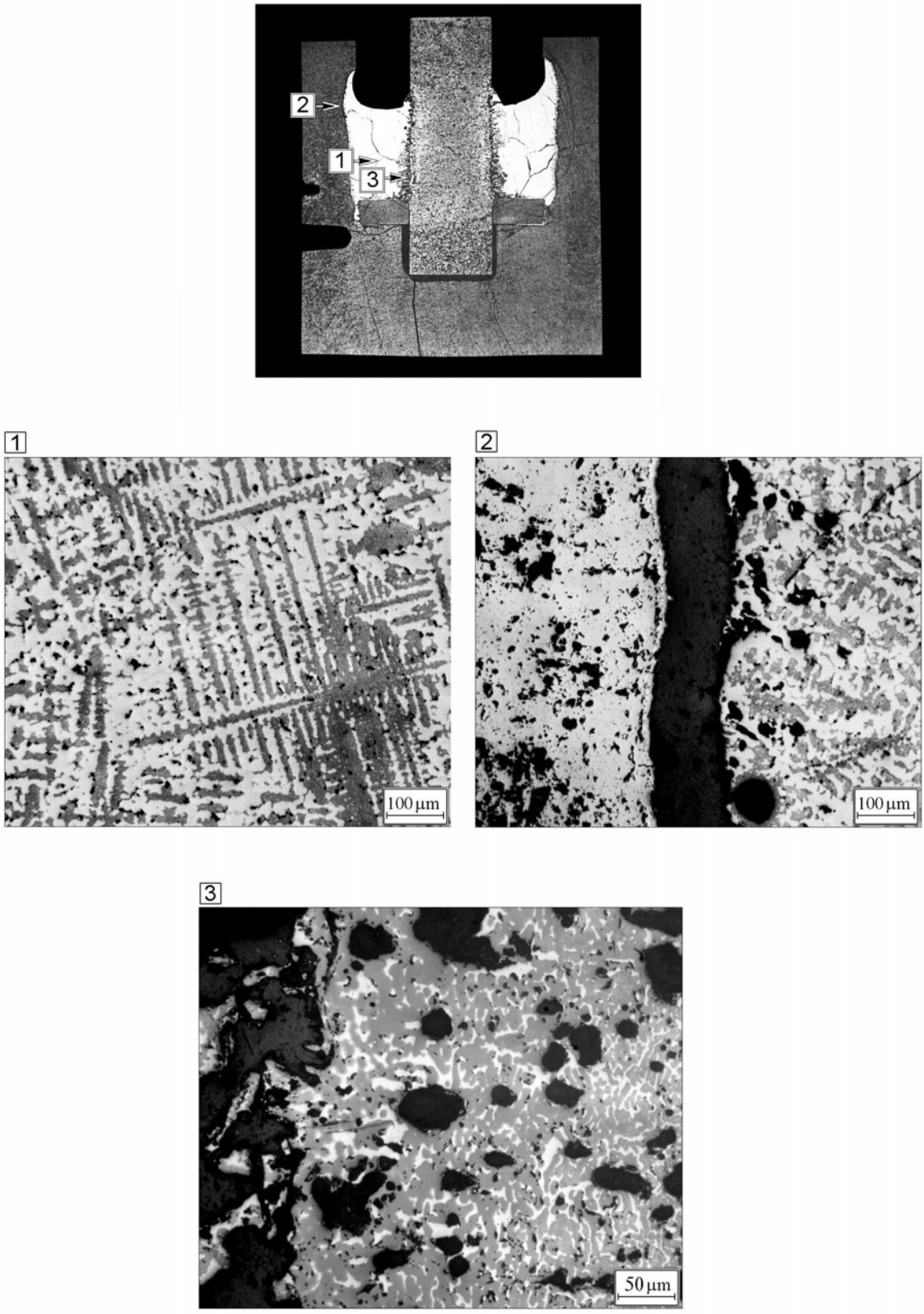

Fig. I - 53. Test 2100 °C, 400 s (with heat insulation). Structure of melt

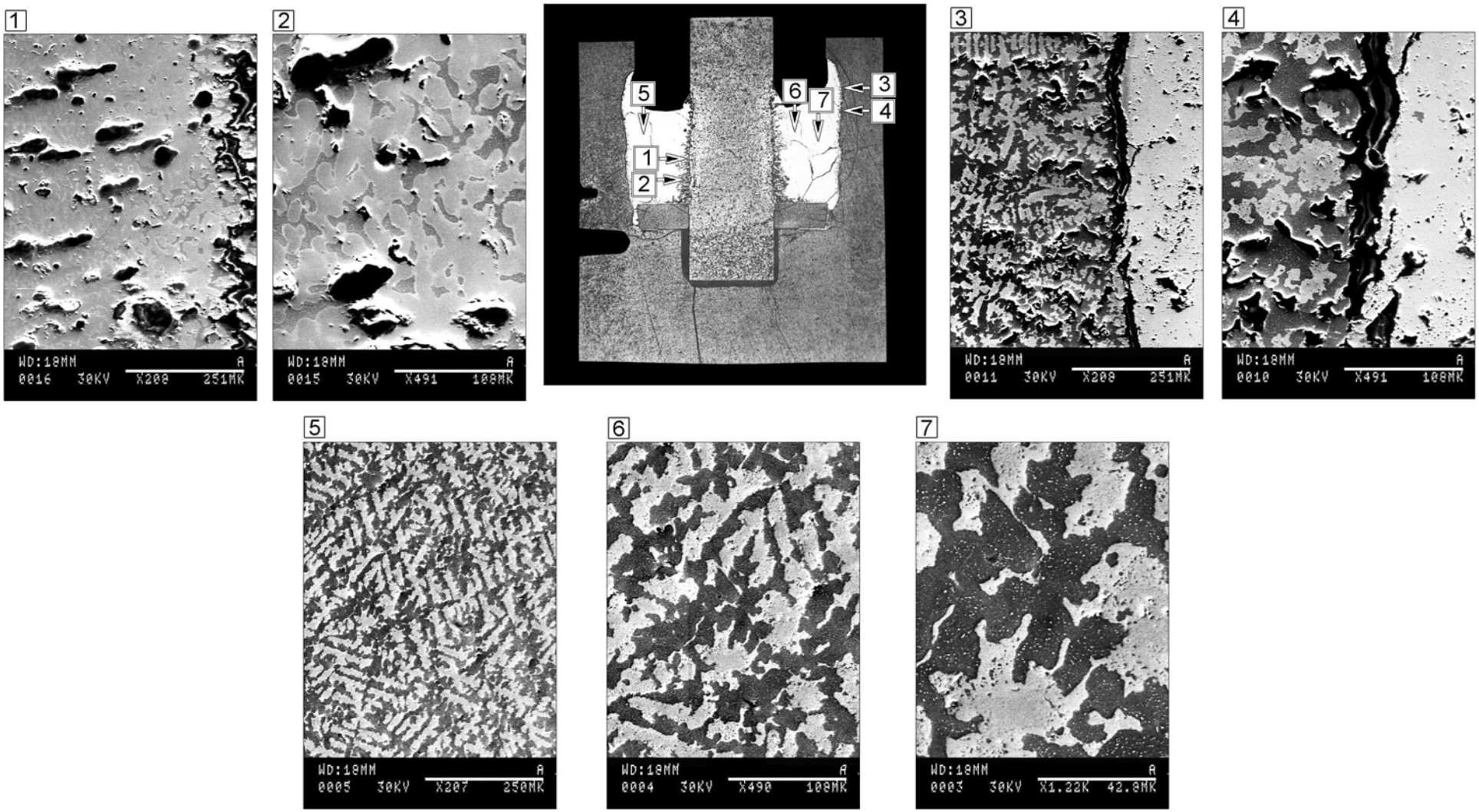

Fig. I - 54. Test 2100 °C, 400 s (with heat insulation). Structure of melt (SEM)

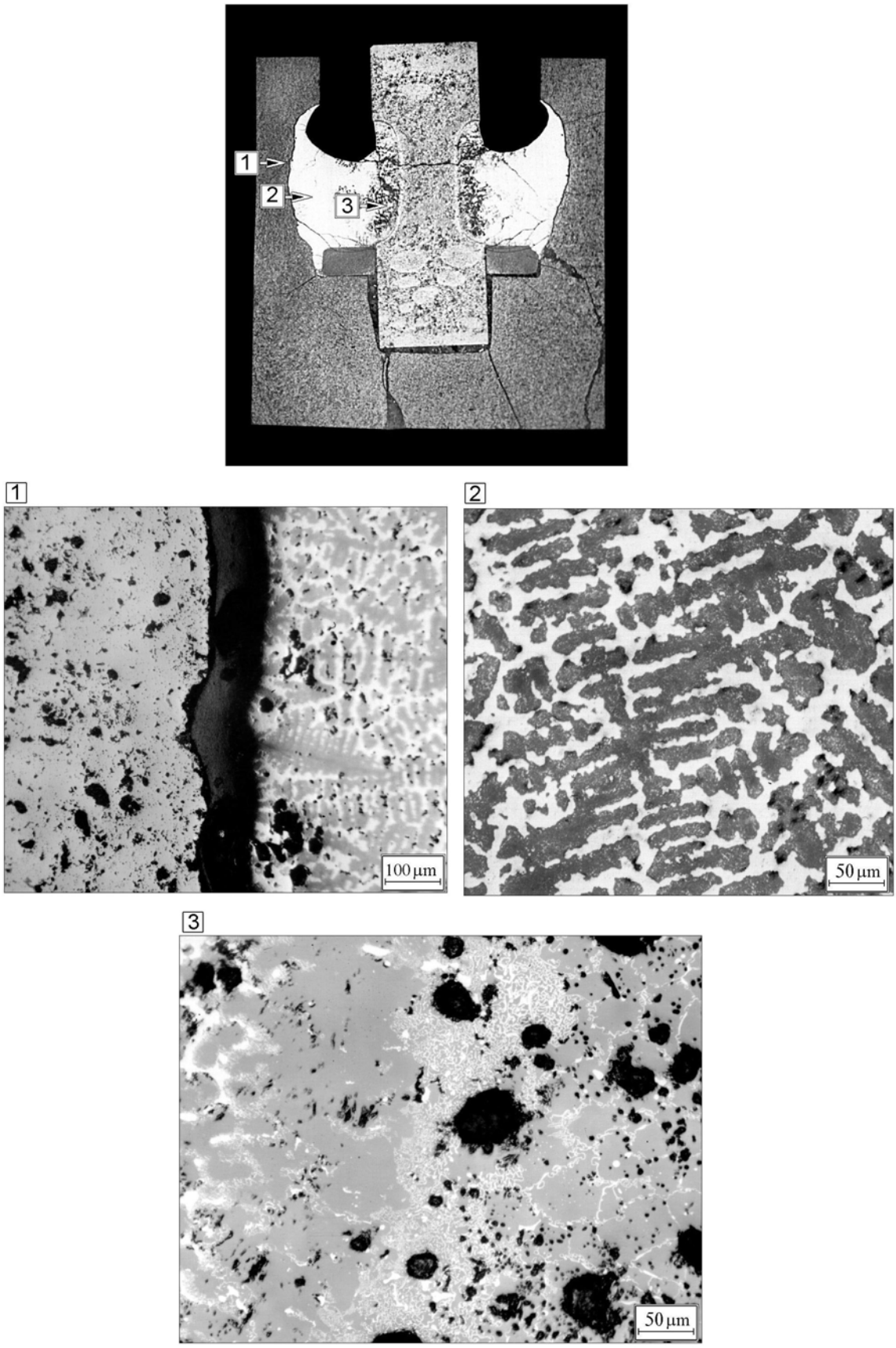

Fig. I - 55. Test 2200 °C, 180 s (with heat insulation). Structure of melt

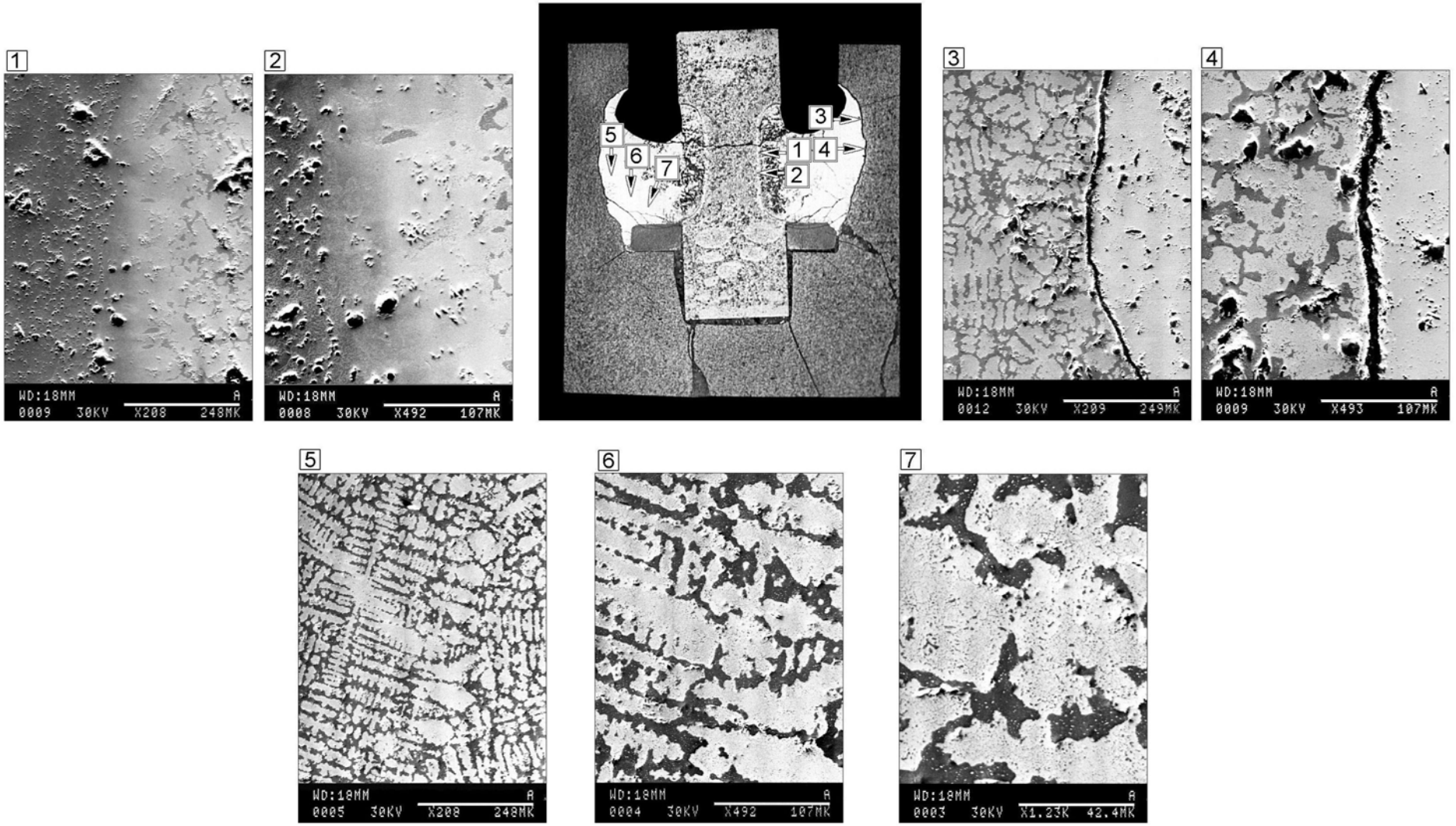

Fig. I - 56. Test 2200 °C, 180 s (with heat insulation). Structure of melt (SEM)

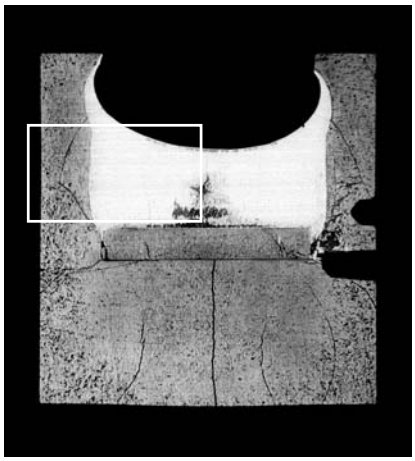

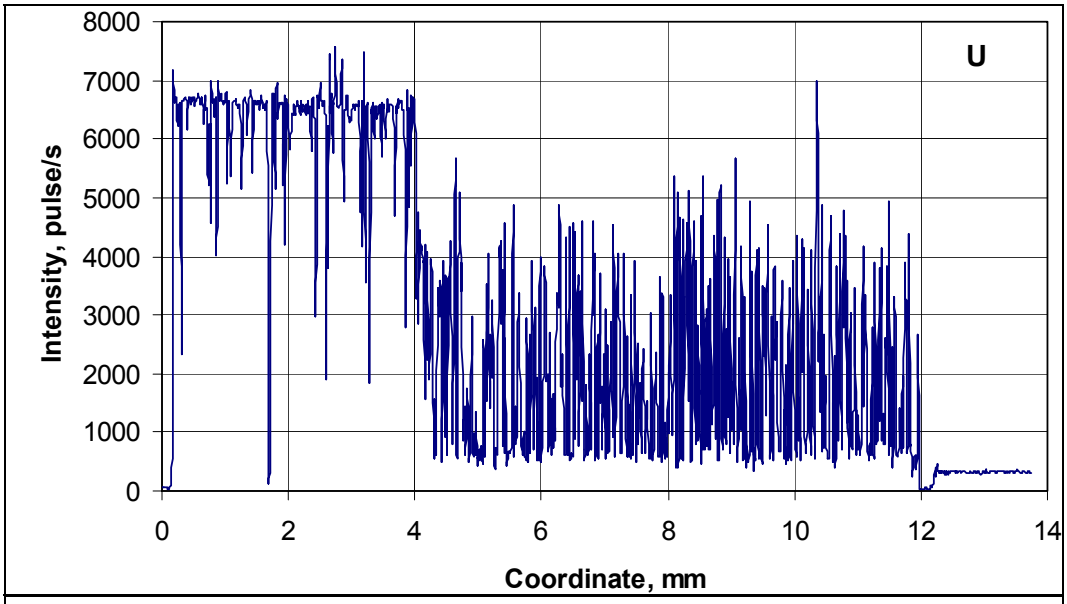

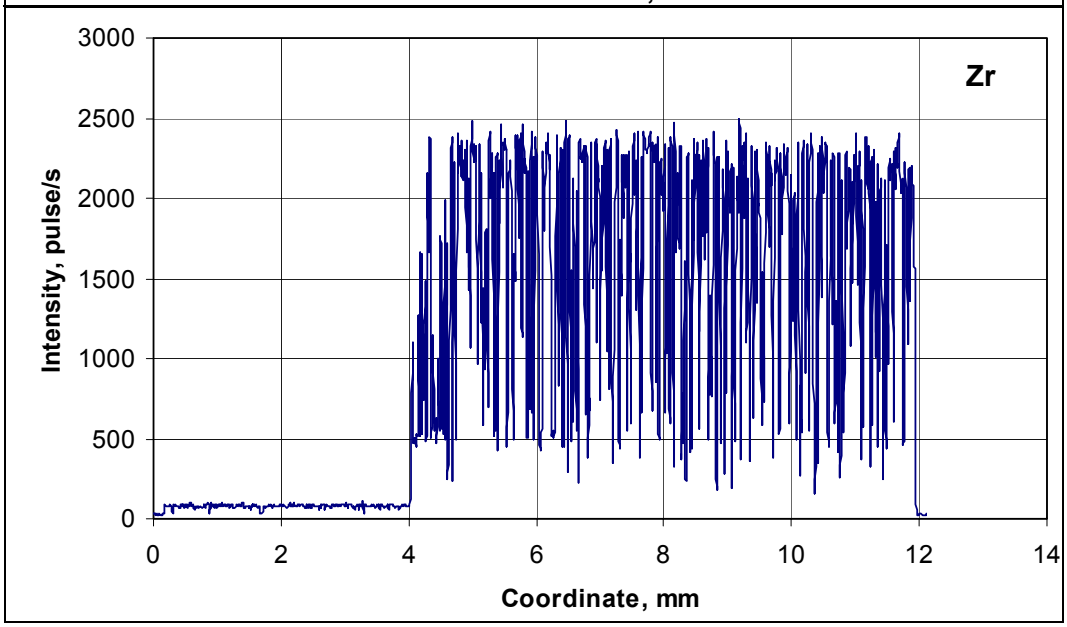

Fig. I - 57. Calibrating test 2100 °C, 600 s (with heat-insulation). Distribution of uranium and zirconium concentration in the melt

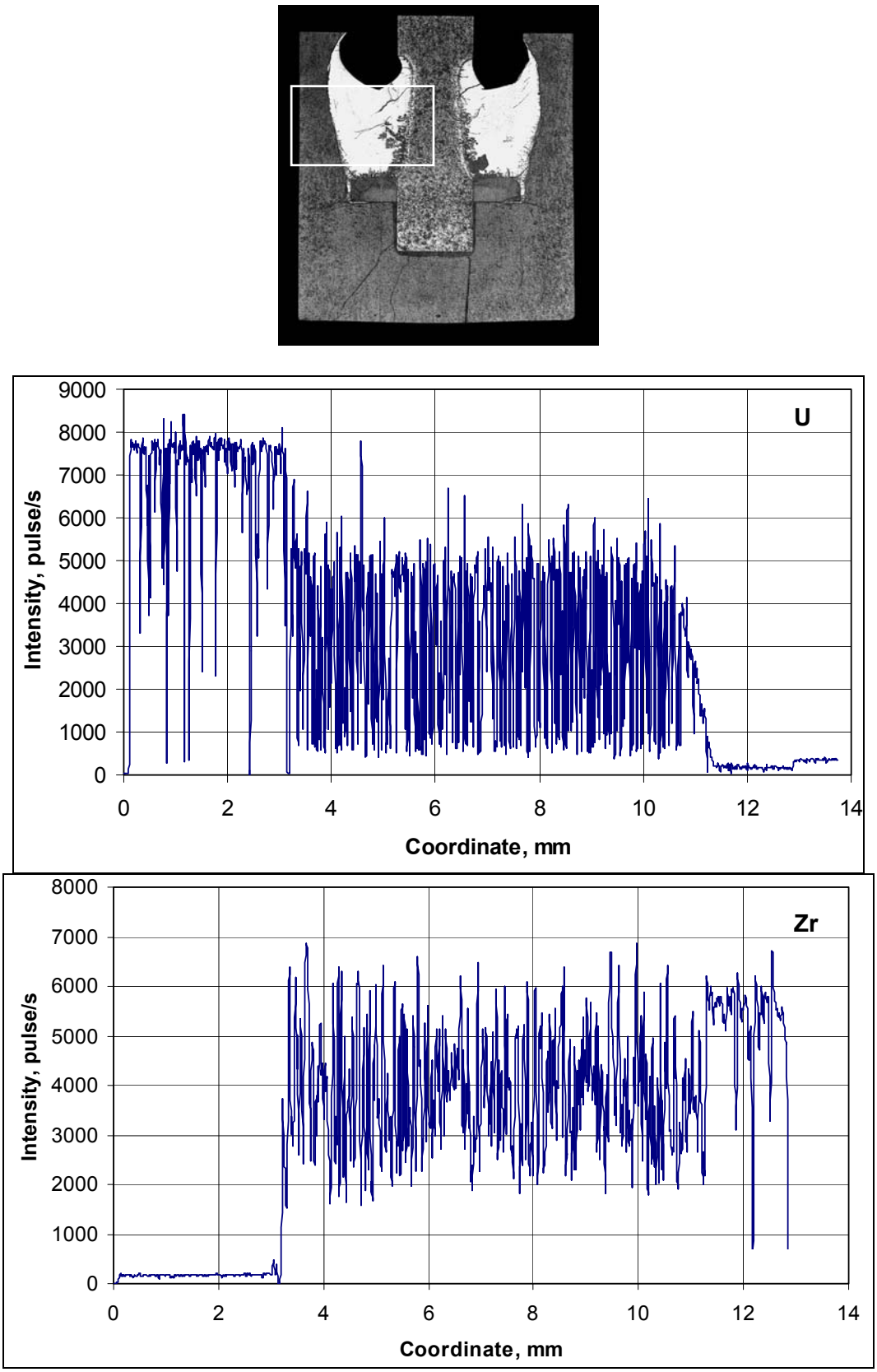

Fig. I - 58. Test 2100 °C, 200 s (with "deep" thermocouple). Distribution of uranium and zirconium concentration in the melt

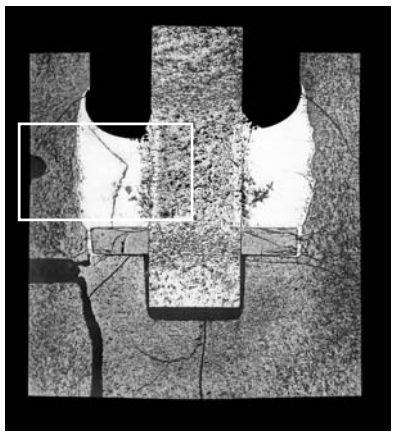

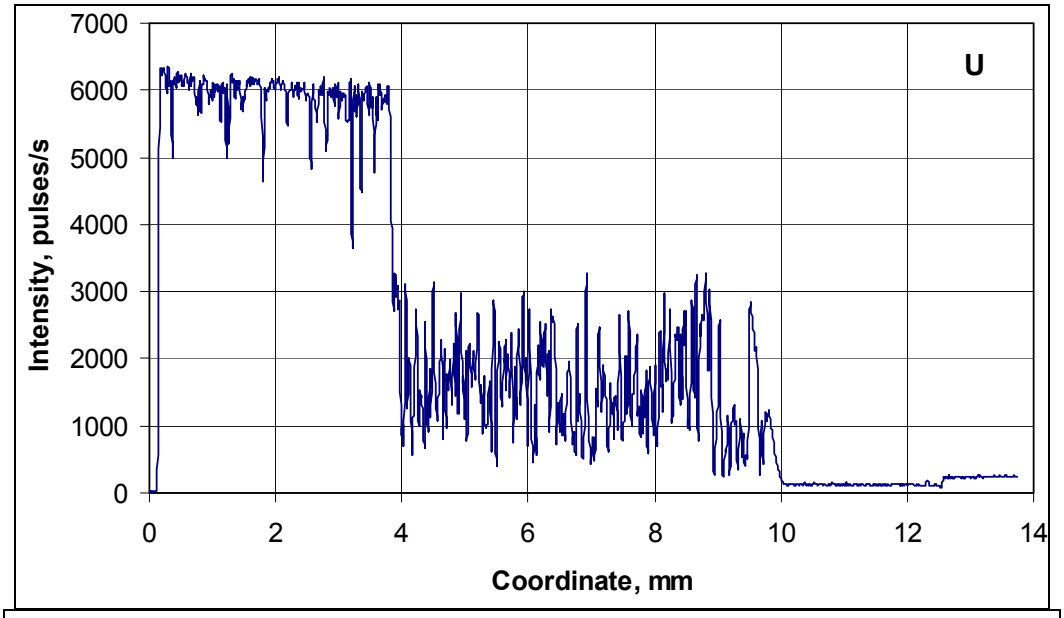

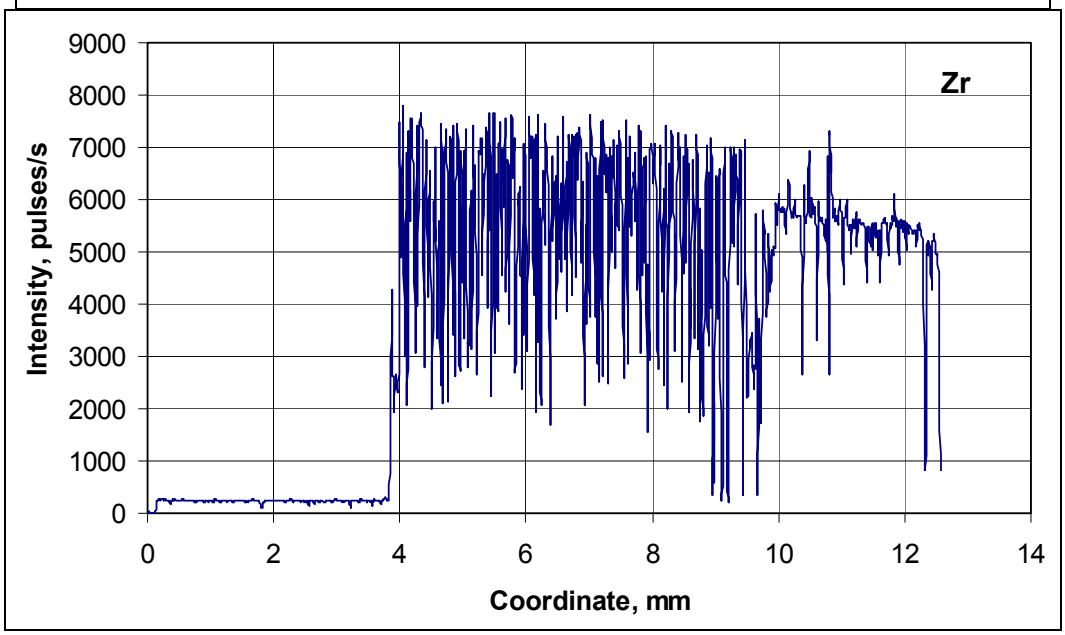

Fig. I - 59. Test 2100 °C, 200 s (with heat-insulation). Distribution of uranium and zirconium concentration in the melt

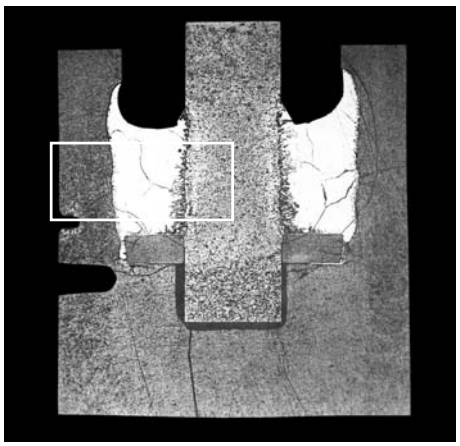

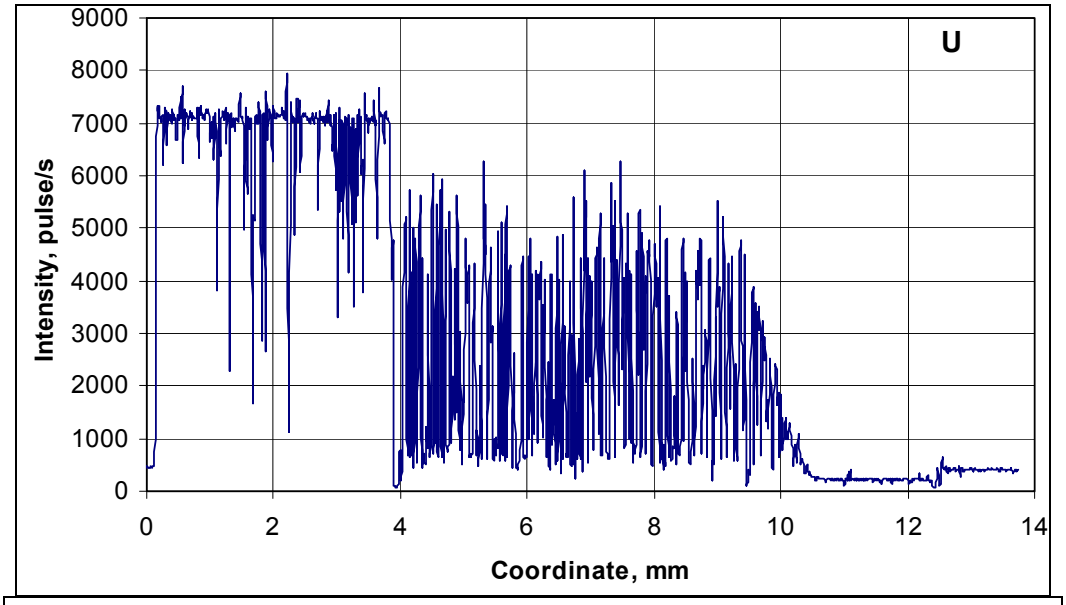

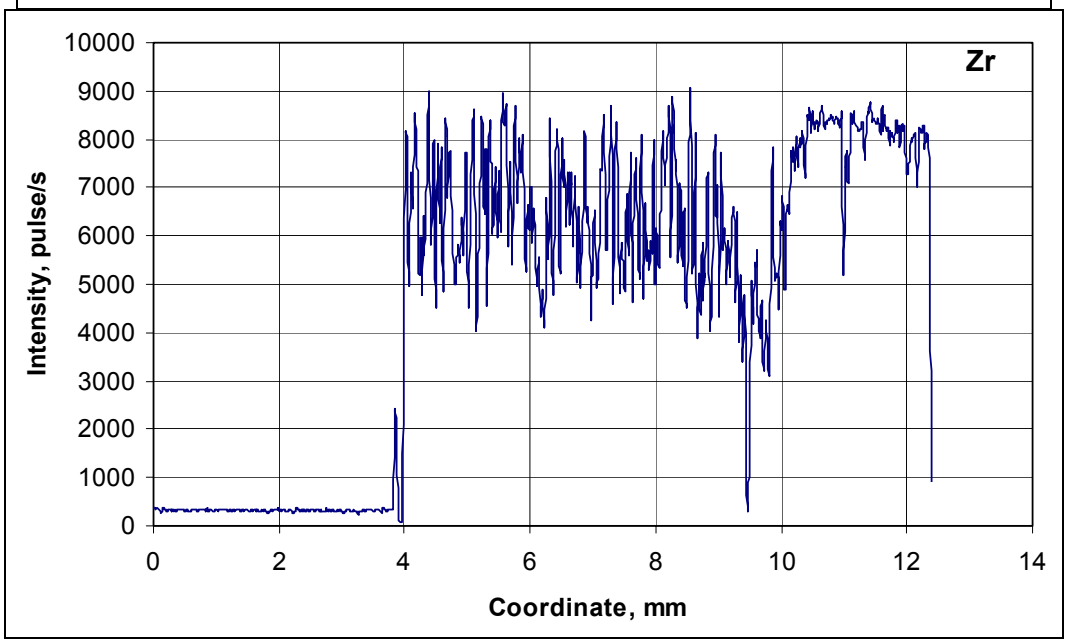

Fig. I - 60. Test 2100 °C, 400 s (with heat-insulation). Distribution of uranium and zirconium concentration in the melt

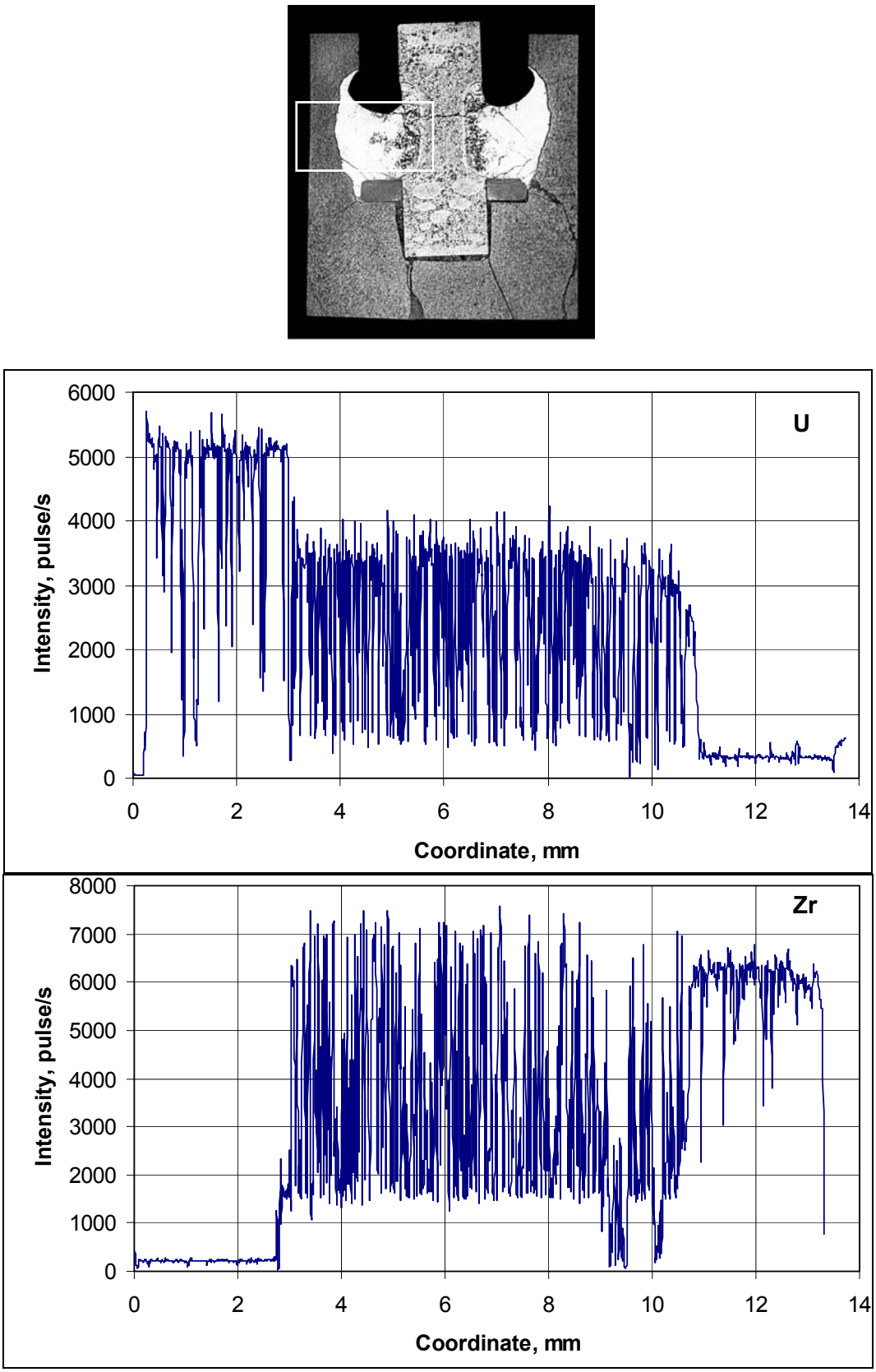

Fig. I - 61. Test 2200 °C, 180 s (with heat-insulation). Distribution of uranium and zirconium concentration in the melt

Part II. Modelling of simultaneous dissolution of UO_2 and ZrO_2 by molten Zry

1. Introduction

Existing models of separate dissolution of UO_2 and ZrO_2 are not able to calculate correctly the simultaneous dissolution of UO_2 and ZrO_2 by molten Zr. The main objective of the IBRAE subcontract in the COLOSS Project Task WP7.3 is to develop a model in the Russian code SVECHA (mechanistic code to study a single rod behaviour) able to take into account these phenomena. The model will be developed in order to be applicable in Severe Accident codes used for plant calculations such as ICARE. The work involves two activities:

1/ The interpretation of separate-effect tests results carried out by RIAR-Dimitrovgrad using UO_2 crucibles (WP2.1). This activity will enable the understanding of physical processes involved during simultaneous dissolution.

2/ The analytic support to the experimental team in order to define the experimental procedure, the instrumentation and post-test examinations required for modelling needs.

A preliminary work has been already fulfilled by IBRAE within CIT Project (4^{th} FP) where the first scoping tests on simultaneous dissolution were analysed on the base of available models for separate dissolution of UO_2 and ZrO_2 by molten Zr [1]. In the subsequent work of IBRAE on SVECHA code development, a new model for simultaneous dissolution of UO_2 and ZrO_2 by molten Zr was proposed [2].

In the current Report development of the new mechanistic model for simultaneous dissolution of UO_2 and ZrO_2 by molten Zr and its validation against full set of RIAR experimental data, is presented.

2. Model description

The updated version of the IBRAE model on simultaneous dissolution of UO_2 and ZrO_2 by molten Zr is presented in the current section.

In order to consider simultaneous dissolution of UO_2 and ZrO_2 by molten Zr, one should consider a ternary U-Zr-O system at test temperatures. The melt in crucible and bundle tests has rather homogeneous composition due to the convective stirring, and for this reason, concentration changes from the interface to bulk values occur in a thin transition layer δ in the melt at the interface.

The interface concentrations in the melt $c_O(I)$, $c_{Zr}(I)$ and $c_U(I)$ sustain in equilibrium with solid phase and, thus, belong to the liquidus line:

$$F_{liq}\left(c_O(I), c_U(I), c_{Zr}(I)\right) = F_{liq}\left(c_O^*, c_U^*, c_{Zr}^*\right) = 0\,. \tag{1}$$

In the simplest approximation this equation can be linearised:

$$c_O(I) = g_1 + g_2 c_U(I)\,, \tag{2}$$

where temperature dependent parameters $g_1(T)$ and $g_2(T)$ determine position of a straight (liquidus) line in the ternary phase diagram, Fig. 1.

The molar density of the melt is assumed independent of the dissolved oxygen and is denoted by $c_M \approx 0.068$ mol/cm^3 on an oxygen-free basis [3]:

$$c_U + c_{Zr} = c_M\,. \tag{3}$$

The solidus line:

$$F_{sol}\left(\rho_O^*, \rho_U^*, \rho_{Zr}^*\right) = 0\,, \tag{4}$$

can be represented with a good accuracy by a straight line parallel to the U-Zr axis [1,2] in the ternary phase diagram (Fig. 1), and thus can be described by relationships:

$$\rho_U^* + \rho_{Zr}^* = \rho_S = const.\,, \qquad \rho_O^* = const.\,, \tag{5}$$

where ρ_S and ρ_O^* coincide with the corresponding values $\rho_{Zr(U)}$ and $\varphi_O(I_2) \equiv \varphi_O$ ($\rho_O(I_1) \equiv \rho_O$) in pure ZrO_{2-x} (UO_{2-x}) .

The equilibrium tie-lines in the phase diagram connect points in the liquidus and solidus lines, therefore, they relate also the interface concentrations in the melt and solid phase. This means that composition of the solid ceramic phase near the interface can be different from pure ZrO_{2-x} (or UO_{2-x}) and contains an admixture of U (or Zr) cations, i.e. corresponds to the mixed ceramic phase $(U,Zr)O_{2-x}$.

It is straightforward to show that in the case of the UO_2 or ZrO_2 layer dissolution, the thickness of the interface boundary layer in the solid phase with the mixed composition $(U,Zr)O_{2-x}$ is extremely small (owing to a rather small diffusivity of cations in the ceramic phase which prevent them from deep penetration in the solid bulk), and therefore can be neglected in the mass balance and flux matching equations. In this case an "effective" boundary concentration $\widetilde{\rho}_{U(Zr)}$, which corresponds to the bulk solid layer composition, i.e. pure UO_2 (ZrO_2) phase, should be used: $\widetilde{\rho}_U = \widetilde{\rho}_{Zr} = \rho_S$.

Conversely, in the case of the oxide (UO_2 or ZrO_2) layer growth this boundary layer is not anymore small, since the oxide layer grows with the mixed composition $(U,Zr)O_{2-x}$ that is in equilibrium with the U-Zr-O melt at the interface. In this case the real boundary concentration which is determined by intersection of the equilibrium tie-lines with the solidus line, should be used in the mass transfer equations: $\widetilde{\rho}_U = \rho_U^*$, and $\widetilde{\rho}_{Zr} = \rho_{Zr}^*$.

On the other hand, in accordance with numerous observations in the crucible tests, it is additionally assumed for the UO_2 layer that only dissolution of this layer (and no growth) can occur in the course of its interactions with the U-Zr-O melt, whereas either dissolution or growth of the ZrO_2 layer (i.e. “erosion” and “corrosion” stages [2,4]) were observed in the tests and will be considered in the current model.

The tie-lines that connect equilibrium concentrations at the interface, for simplicity, can be considered as straight lines starting from the O apex in the ternary phase diagram, as shown in Fig. II - 1 by dotted lines, i.e.

$$\frac{\rho_U^*}{\rho_S} = \frac{c_U^*}{c_m}, \qquad \frac{\rho_{Zr}^*}{\rho_S} = \frac{c_{Zr}^*}{c_m}. \tag{6}$$

Such a simplification can be easily avoided if more accurate equations for the tie-lines are available.

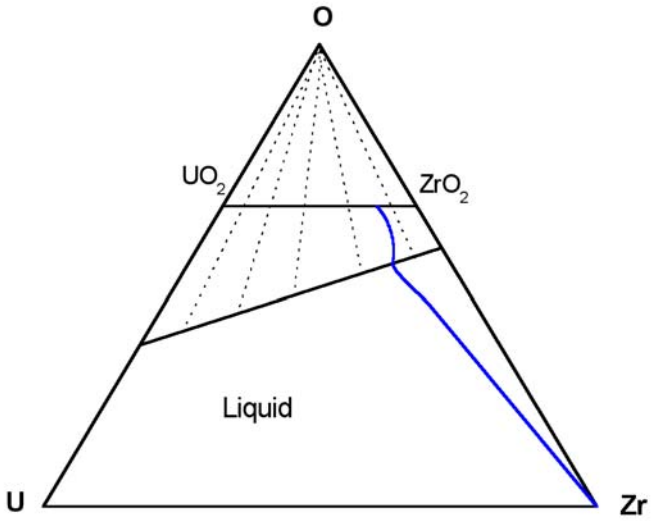

Fig. II - 1. Schematic representation of the ternary U-Zr-O phase diagram with equilibrium tie-lines (*dotted lines*)

2.1. Saturation stage

In this approximation for the tie-lines, the system of equations for the mass transfer in the first, saturation stage in a general formulation (applicable either to plane, *L* =1, or to cylindrical, *L* =2, geometry) takes the form:

- Mass balances

$$-D_O^{UO_2}\frac{\partial\rho_O}{\partial r}\bigg|_{I_1} r_1^{L-1} - \rho_O(I_1)r_1^{L-1}\frac{dr_1}{dt} + D_O^{ZrO_2}\frac{\partial\varphi_o}{\partial r}\bigg|_{I_2} r_2^{L-1} - \varphi_O(I_2)\left[r_3^{L-1}\frac{dr_3}{dt} - r_2^{L-1}\frac{dr_2}{dt}\right]$$

$$= \frac{1}{L}\frac{d}{dt}\left[c_O(B)(r_2^L - r_1^L)\right], \quad (7)$$

$$-\rho_S r_1^{L-1}\frac{dr_1}{dt} - \tilde{\rho}_U(I_2)\left[r_3^{L-1}\frac{dr_3}{dt} - r_2^{L-1}\frac{dr_2}{dt}\right] = \frac{1}{L}\frac{d}{dt}\left[c_U(B)(r_2^L - r_1^L)\right], \quad (8)$$

$$-\rho_S\left[r_1^{L-1}\frac{dr_1}{dt} + r_3^{L-1}\frac{dr_3}{dt} - r_2^{L-1}\frac{dr_2}{dt}\right] = \frac{c_M}{L}\frac{d}{dt}\left[r_2^L - r_1^L\right], \quad (9)$$

where r_1, r_2 and r_3 are positions of the boundaries of the solid UO_2 and ZrO_2 layers, as schematically shown in Fig. II - 2.

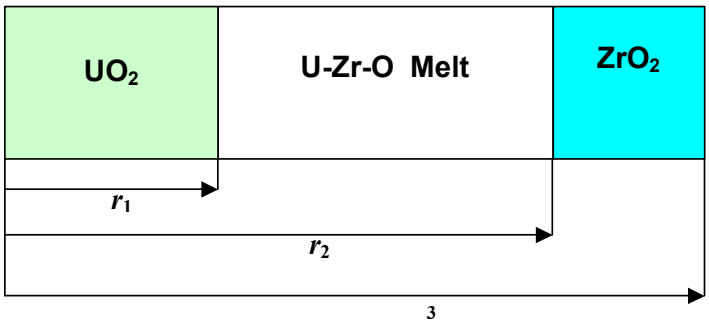

Fig. II - 2. Schematic representation of the cylindrical model geometry

In accordance with the above presented explanation, the "effective" interface boundary concentration in the ZrO_2 phase is different for various regimes and can be represented in the form:

$$\tilde{\rho}_U(I_2) = \left[\varphi_U - \left(\varphi_U - \rho_S\frac{c_U(I_2)}{c_M}\right)\theta\left(\frac{d(r_3^L - r_2^L)}{dt}\right)\right], \quad (10)$$

which corresponds to $\tilde{\rho}_U(I_2) = \varphi_U$ (φ_U is uranium molar concentration in zirconia at internal interface, for instance, $\varphi_U = 0$ at the beginning of dissolution process) in the cases of the ZrO_2 layer dissolution, and to the mixed composition determined by Eq. (6), $\tilde{\rho}_U(I_2) = \rho_S\frac{c_U(I_2)}{c_M}$, in the case of the ZrO_2 layer growth.

- Flux matches

$$-D_O^{UO_2}\left.\frac{\partial\rho_O}{\partial r}\right|_{I_1}-\rho_O(I_1)\frac{dr_1}{dt}=k_O(I_1)\left[c_O(I_1)-c_O(B)\right]+c_O(I_1)\left[v_1(I_1)-\frac{dr_1}{dt}\right], \quad (11)$$

$$-\rho_S\frac{dr_1}{dt}=k_U(I_1)\left[c_U(I_1)-c_U(B)\right]+c_U(I_1)\left[v_1(I_1)-\frac{dr_1}{dt}\right], \quad (12)$$

$$-\rho_S\frac{dr_1}{dt}=c_M\left[v_1(I_1)-\frac{dr_1}{dt}\right], \quad (13)$$

$$c_O(I_1)=g_1(T)+g_2(T)c_U(I_1), \quad (14)$$

and

$$k_O(I_2)\left[c_O(B)-c_O(I_2)\right]+c_O(I_2)\left[v_1(I_1)\left(\frac{r_1}{r_2}\right)^{L-1}-\frac{dr_2}{dt}\right]$$
$$=-D_O^{ZrO_2}\left.\frac{\partial\varphi_O}{\partial r}\right|_{I_2}+\varphi_O(I_2)\left[\frac{dr_3}{dt}\left(\frac{r_3}{r_2}\right)^{L-1}-\frac{dr_2}{dt}\right], \quad (15)$$

$$k_U(I_2)\left[c_U(B)-c_U(I_2)\right]+c_U(I_2)\left[v_1(I_1)\left(\frac{r_1}{r_2}\right)^{L-1}-\frac{dr_2}{dt}\right]=\tilde{\rho}_U(I_2)\left[\frac{dr_3}{dt}\left(\frac{r_3}{r_2}\right)^{L-1}-\frac{dr_2}{dt}\right], \quad (16)$$

$$c_M\left[v_1(I_1)\left(\frac{r_1}{r_2}\right)^{L-1}-\frac{dr_2}{dt}\right]=\rho_S\left[\frac{dr_3}{dt}\left(\frac{r_3}{r_2}\right)^{L-1}-\frac{dr_2}{dt}\right], \quad (17)$$

$$c_O(I_2)=g_1(T)+g_2(T)c_U(I_2), \quad (18)$$

where $\rho_O\,(\varphi_O)$ – oxygen molar density in the UO_2 (ZrO_2) layer,

$c_{O(U,Zr)}$ – oxygen (uranium, zirconium) molar density in the melt,

$D_O^{UO_2(ZrO_2)}$ – oxygen diffusion coefficient in the UO_2 (ZrO_2) layer,

v_1 – net velocity of the melt, due to density difference between liquid and solid phases,

$k_O(I_i)$ – oxygen mass transfer coefficient in the melt at *i*-th interface, *i* =1,2;

$k_{U(Zr)}(I_i)$ – uranium (zirconium) mass transfer coefficients in the melt that, due to Eq. (3) obey an additional relationship:

$k_{Zr}\left(c_{Zr}(I)-c_{Zr}(B)\right)=-k_U\left(c_U(I)-c_U(B)\right)$.

In the melt stirred by natural convection, mass transfer coefficients are calculated as

$$k_O=\frac{D_O^{liq}}{\delta}, \quad k_U=\frac{D_U^{liq}}{\delta}\approx k_O/2, \quad (19)$$

where δ is the thickness of the transition boundary layer,

$\delta\approx d/Sh^{1/4}=d/\left(0.54Gr^{1/4}Sc^{1/4}\right)$, if $Gr\cdot Sc > 10^3$, (19a)

$Gr=g\left(\Delta\rho/\rho\right)d^3/\nu^2$ is the Grashoff number,

$Sc=\nu/D_U^{liq}$ is the Schmidt number,

d is characteristic dimension of the melt (i.e. in the considered cylindrical geometry $d=r_2-r_1$).

Similarly to [5], this can be written in the form:

$$k_O^*(I_i) \approx 0.54\left(\frac{g(D_U^{liq})^3}{\nu dc_M}\right)^{1/4}\left[\frac{(M_U - M_{Zr})(c_U(I_i) - c_U(B)) + M_O(c_O(I_i) - c_O(B))}{M_{Zr}}\right]^{1/4}, \qquad (20)$$

where

D_U^{liq} – uranium diffusion coefficient in the melt,

ν – viscosity of the melt,

$M_{U(Zr)}$ – atomic weight of U (Zr).

In the diffusion regime when $Gr \cdot Sc$ < 10^3, mass transfer by molecular diffusion in the melt should be considered. For simplicity of numerical calculations, the convection equations will be applied to the diffusion regime by formal extension of Eq. (19a) to the limit $Sh \to 1$, i.e. $\delta \approx d$ (also in the following consideration of the precipitation stage).

An additional assumption $k_O = k_U$ (instead of Eq. (19)) can significantly simplify calculations. Sensitivity of calculation results to this simplification is demonstrated in Fig. II - 3 for UO_2/melt interaction and in Fig. II - 4 for the UO_2/melt/ZrO_2 simultaneous dissolution. Analytical transformation of Eqs. (11)-(18) under such a simplification allows explicit representation of the interface velocities, taking into account the above-mentioned prevention of the UO_2 layer growth and, according to Eq. (20), weak dependence of mass transfer coefficients on melt composition:

$$\left.\frac{dr_1}{dt}\right|_{T=T_{UO_2},I_1} = \begin{cases} \dfrac{-D_O^{UO_2}\left.\dfrac{\partial \rho_O}{\partial r}\right|_{I_1} - k_O(I_1)\left[c_O^{\max} - c_O(B)\right]}{\rho_O - (g_1 + c_m g_2)\dfrac{\rho_S}{c_M}}, & \dfrac{dr_1}{dt} \le 0 \\ 0, & \dfrac{dr_1}{dt} > 0 \end{cases}, \qquad (21)$$

$$\left.\left(r_3^{L-1}\frac{dr_3}{dt} - r_2^{L-1}\frac{dr_2}{dt}\right)\right|_{T=T_{ZrO_2},I_2}$$

$$= \begin{cases} r_2^{L-1}\dfrac{D_O^{ZrO_2}\left.\dfrac{\partial \varphi_O}{\partial r}\right|_{I_2} - k_O(I_2)\left[c_O^{\max} - c_O(B)\right]}{\varphi_O - g_1\dfrac{\rho_S}{c_M}}, & r_3^{L-1}\dfrac{dr_3}{dt} - r_2^{L-1}\dfrac{dr_2}{dt} \le 0 \\ r_2^{L-1}\dfrac{D_O^{ZrO_2}\left.\dfrac{\partial \varphi_O}{\partial r}\right|_{I_2} - k_O(I_2)\left[c_O^{\max} - c_O(B)\right]}{\varphi_O - c_O^{\max}\dfrac{\rho_S}{c_M}}, & r_3^{L-1}\dfrac{dr_3}{dt} - r_2^{L-1}\dfrac{dr_2}{dt} > 0 \end{cases}, \qquad (22)$$

where $c_O^{\max} = \left[g_1(T) + c_U(B)g_2(T)\right]$. (23)

Therefore, Eqs. (21)-(23) can be directly used instead of Eqs. (15)-(17) in the following calculations.

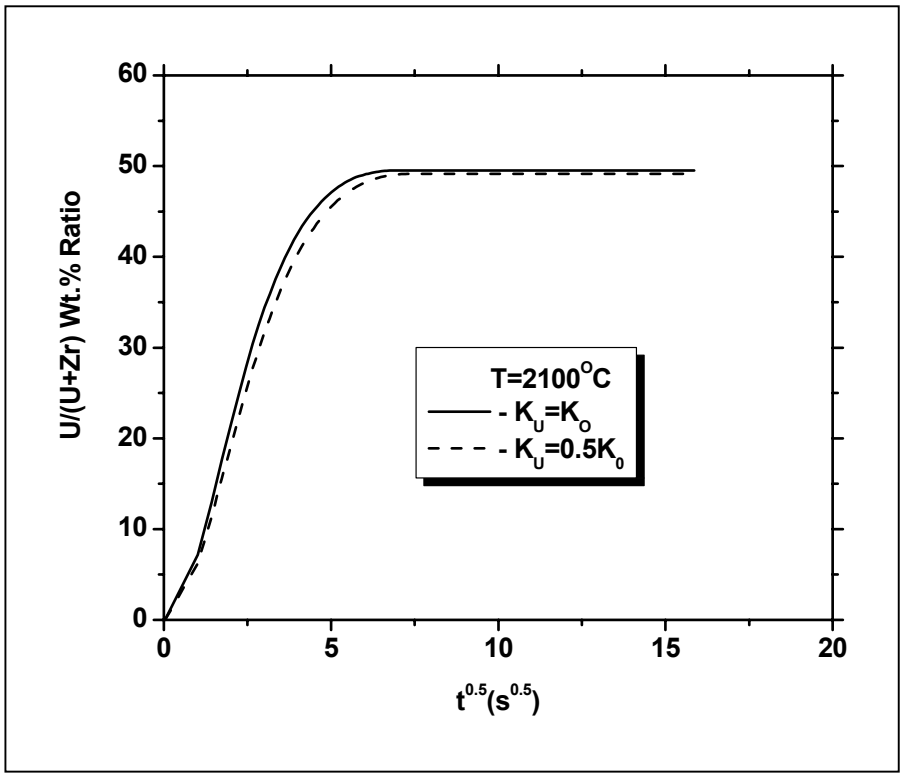

Fig. II - 3. Comparison of models with different mass transfer coefficients in the melt for the case of UO_2/melt interaction

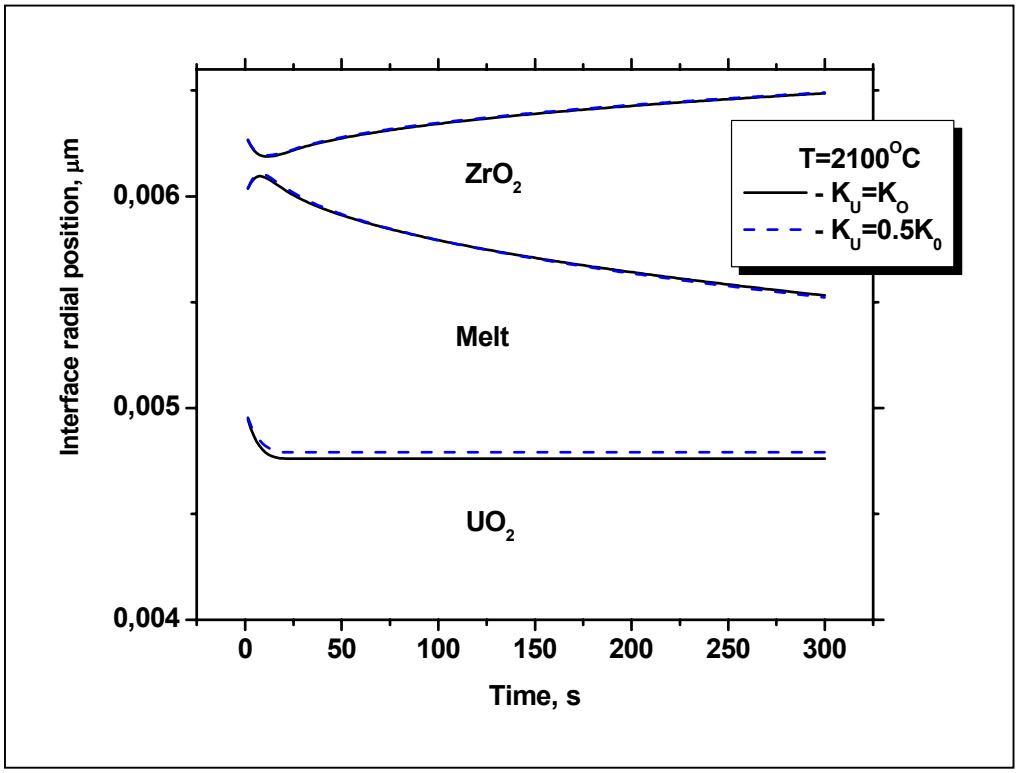

Fig. II - 4. Comparison of models with different mass transfer coefficients in the melt for the case of UO_2/melt/ZrO_2 interaction

2.2. Precipitation stage

The saturation stage of the interactions proceeds until saturation of the melt is reached. In the precipitation stage the oxygen flux to the melt continues, this leads to oversaturation of the melt and onset of precipitation.

The $(U,Zr)O_2$ precipitates are in a local thermodynamic equilibrium with the surrounding melt, therefore, their composition belongs to the solidus line, Eqs. (5), and relates to the bulk composition of the melt by the equilibrium tie-line equation, Eq. (6).

In this case the system of governing equations takes the form:

- Mass balances

$$-D_O^{UO_2}\frac{\partial\rho_O}{\partial r}\bigg|_{I_1} r_1^{L-1} - \rho_O r_1^{L-1}\frac{dr_1}{dt} + D_O^{ZrO_2}\frac{\partial\varphi_o}{\partial r}\bigg|_{I_2} r_2^{L-1} - \varphi_O\left[r_3^{L-1}\frac{dr_3}{dt} - r_2^{L-1}\frac{dr_2}{dt}\right] = \frac{1}{L}\frac{d}{dt}\left[\left(c_O^*(1-f)+f\rho_O^*\right)\left(r_2^L - r_1^L\right)\right], \quad (24)$$

$$-\rho_S r_1^{L-1}\frac{dr_1}{dt} - \widetilde{\rho}_U(I_2)\left[r_3^{L-1}\frac{dr_3}{dt} - r_2^{L-1}\frac{dr_2}{dt}\right] = \frac{1}{L}\frac{d}{dt}\left[c_U^*\left(1-f\cdot\left(1-\frac{\rho_S}{c_M}\right)\right)\left(r_2^L - r_1^L\right)\right], \quad (25)$$

$$-\rho_S\left[r_1^{L-1}\frac{dr_1}{dt} + r_3^{L-1}\frac{dr_3}{dt} - r_2^{L-1}\frac{dr_2}{dt}\right] = \frac{1}{L}\frac{d}{dt}\left[\left(c_M(1-f)+f\rho_S\right)\left(r_2^L - r_1^L\right)\right], \quad (26)$$

where f is the volume fraction of the ceramic precipitates in the uniformly stirred melt in the bulk region. In the mass balances a thin transition layer is neglected due to its small thickness, $\delta << L, M$.

It can be shown that considering flux matching equations one can neglect formation of precipitates in the transition boundary layer in the melt, i.e. $f = 0$ in this layer. In such an approximation one obtains:

- Flux matches

$$-D_O^{UO_2}\frac{\partial\rho_O}{\partial r}\bigg|_{I_1} - \rho_O(I_1)\frac{dr_1}{dt} = \widetilde{k}_O(I_1)\left[c_O(I_1) - c_O^*\right] + c_O(I_1)\left[v_1(I_1) - \frac{dr_1}{dt}\right], \quad (27)$$

$$0 = \widetilde{k}_U(I_1)\left[c_U(I_1) - c_U^*\right] + c_U(I_1)\left[v_1(I_1) - \frac{dr_1}{dt}\right], \quad (28)$$

$$-\rho_S\frac{dr_1}{dt} = c_M\left[v_1(I_1) - \frac{dr_1}{dt}\right], \quad (29)$$

$$c_O(I_1) = g_1(T) + g_2(T)c_U(I_1), \quad (30)$$

$$\widetilde{k}_O(I_2)\left[c_O^* - c_O(I_2)\right] + c_O(I_2)\left[v_1(I_2) - \frac{dr_2}{dt}\right] = -D_O^{ZrO_2}\frac{\partial\varphi_O}{\partial r}\bigg|_{I_2} + \varphi_O(I_2)\left[\left(\frac{r_3}{r_2}\right)^{L-1}\frac{dr_3}{dt} - \frac{dr_2}{dt}\right], \quad (31)$$

$$\widetilde{k}_U(I_2)\left[c_U^* - c_U(I_2)\right] + c_U(I_2)\left[v_1(I_1)\left(\frac{r_1}{r_2}\right)^{L-1} - \frac{dr_2}{dt}\right] = \widetilde{\rho}_U\left[\frac{dr_3}{dt}\left(\frac{r_3}{r_2}\right)^{L-1} - \frac{dr_2}{dt}\right], \quad (32)$$

$$c_M\left[v_1(I_2) - \frac{dr_2}{dt}\right] = \rho_S\left[\left(\frac{r_3}{r_2}\right)^{L-1}\frac{dr_3}{dt} - \frac{dr_2}{dt}\right], \quad (33)$$

$$c_O(I_2) = g_1(T) + g_2(T)c_U(I_2), \tag{34}$$

where the bulk values c_O^*, c_U^*, c_{Zr}^* and ρ_O^*, ρ_U^*, ρ_{Zr}^* obey Eqs. (2), (5) and (6).

The value of mass transfer coefficient $k_{O(U)}$ slowly decreases with growth of precipitates in the melt, $k_{O(U)} \propto Sh \propto \nu^{-1/4}$, due to increase of the apparent viscosity ν of the solid-liquid mixture with the increase of the volume fraction f of solid precipitates. In accordance with a recommendation of [6] for corium in the solidification range, the Arrhenius law can be used for the apparent viscosity: $\nu = \nu_{liq}\exp(2.5Cf)$, where ν_{liq} is the liquid phase viscosity, C is an adjustable coefficient in the range 4–4.8. Therefore, a new value

$$\widetilde{k}_{O(U)}(I_i) = k_{O(U)}(I_i)\cdot\exp(-2.5Cf/4) \approx k_{O(U)}(I_i)\cdot\exp(-2.5f), \tag{35}$$

with $k_{O(U)}$ determined in Eq. (20), is introduced in Eq. (27)-(34) to consider increase of viscosity due to precipitation of the ceramic phase in the melt.

Correspondingly, equations similar to Eqs. (21)-(23) with c_O^* and c_U^* standing for $c_O(B)$ and $c_U(B)$, respectively, and $k_{O(U)} \to \widetilde{k}_{O(U)}$, can be derived from the flux matching equations, Eqs. (27)-(34).

2.3. General system of equations (for both stages)

As a result, the systems of equations for both stages can be finally represented in the unified form:

- Mass balances

$$-D_O^{UO_2}\frac{\partial\rho_O}{\partial r}\bigg|_{I_1} r_1^{L-1} - \rho_O(I_1)r_1^{L-1}\frac{dr_1}{dt} + D_O^{ZrO_2}\frac{\partial\varphi_o}{\partial r}\bigg|_{I_2} r_2^{L-1} - \varphi_O(I_2)\left[r_3^{L-1}\frac{dr_3}{dt} - r_2^{L-1}\frac{dr_2}{dt}\right]$$

$$= \frac{1}{L}\frac{d}{dt}[Y_O], \tag{36}$$

$$-\rho_S r_1^{L-1}\frac{dr_1}{dt} - \widetilde{\rho}_U(I_2)\left[r_3^{L-1}\frac{dr_3}{dt} - r_2^{L-1}\frac{dr_2}{dt}\right] = \frac{1}{L}\frac{d}{dt}[Y_U], \tag{37}$$

$$-\rho_S\left[r_1^{L-1}\frac{dr_1}{dt} + r_3^{L-1}\frac{dr_3}{dt} - r_2^{L-1}\frac{dr_2}{dt}\right] = \frac{1}{L}\frac{d}{dt}[Y_{UZ}], \tag{38}$$

where

$$Y_O = c_O(B)(r_2^L - r_1^L),\ Y_U = c_U(B)(r_2^L - r_1^L),\ Y_{UZ} = c_M(r_2^L - r_1^L), \tag{39}$$

during saturation stage, and

$$Y_O = \left(c_O^*(1-f) + f\rho_O^*\right)(r_2^L - r_1^L),\ Y_U = c_U^*\left(1 - f\cdot\left(1 - \frac{\rho_S}{c_M}\right)\right)(r_2^L - r_1^L),$$

$$Y_{UZ} = \left(c_M(1-f) + f\rho_S\right)(r_2^L - r_1^L), \quad c_O^* = (g_1 + c_U^* g_2), \tag{40}$$

during the precipitation stage.

- Flux matches:

$$-D_O^{UO_2}\left.\frac{\partial \rho_O}{\partial r}\right|_{I_1}-\rho_O(I_1)\frac{dr_1}{dt}=\widetilde{k}_O(I_1)\left[c_O(I_1)-\widetilde{c}_O\right]+c_O(I_1)\left[v_1(I_1)-\frac{dr_1}{dt}\right], \tag{41}$$

$$-\rho_S\frac{dr_1}{dt}=\widetilde{k}_U(I_1)\left[c_U(I_1)-\widetilde{c}_U\right]+c_U(I_1)\left[v_1(I_1)-\frac{dr_1}{dt}\right], \tag{42}$$

$$-\rho_S\frac{dr_1}{dt}=c_M\left[v_1(I_1)-\frac{dr_1}{dt}\right], \tag{43}$$

$$c_O(I_1)=g_1(T)+g_2(T)c_U(I_1), \tag{44}$$

$$\widetilde{k}_O(I_2)\left[\widetilde{c}_O-c_O(I_2)\right]+c_O(I_2)\left[v_1(I_2)-\frac{dr_2}{dt}\right]=-D_O^{ZrO_2}\left.\frac{\partial \varphi_O}{\partial r}\right|_{I_2}+\varphi_O(I_2)\left[\left(\frac{r_3}{r_2}\right)^{L-1}\frac{dr_3}{dt}-\frac{dr_2}{dt}\right], \tag{45}$$

$$\widetilde{k}_U(I_2)\left[\widetilde{c}_U-c_U(I_2)\right]+c_U(I_2)\left[v_1(I_1)\left(\frac{r_1}{r_2}\right)^{L-1}-\frac{dr_2}{dt}\right]=\widetilde{\rho}_U\left[\frac{dr_3}{dt}\left(\frac{r_3}{r_2}\right)^{L-1}-\frac{dr_2}{dt}\right], \tag{46}$$

$$c_M\left[v_1(I_2)-\frac{dr_2}{dt}\right]=\rho_S\left[\left(\frac{r_3}{r_2}\right)^{L-1}\frac{dr_3}{dt}-\frac{dr_2}{dt}\right], \tag{47}$$

$$c_O(I_2)=g_1(T)+g_2(T)c_U(I_2), \tag{48}$$

where

$$\widetilde{c}_{O(U)}=c_{O(U)}(B),\ \text{during saturation stage,} \tag{49}$$

and

$$\widetilde{c}_{O(U)}=c^*_{O(U)},\ \text{during precipitation stage.} \tag{50}$$

From flux matches one can derive:

$$\left.\frac{dr_1}{dt}\right|_{T=T_{UO_2},I_1}=\begin{cases}\dfrac{-D_O^{UO_2}\left.\dfrac{\partial \rho_O}{\partial r}\right|_{I_1}-\widetilde{k}_O(I_1)\left[c_O^{\max}-\widetilde{c}_O\right]}{\rho_O-(g_1+c_m g_2)\dfrac{\rho_U}{c_M}}, & \dfrac{dr_1}{dt}\le 0\\ 0, & \dfrac{dr_1}{dt}>0\end{cases}, \tag{51}$$

$$\left(r_3^{L-1}\frac{dr_3}{dt}-r_2^{L-1}\frac{dr_2}{dt}\right)\Bigg|_{T=T_{ZrO_2},I_2}$$

$$=\begin{cases}r_2^{L-1}\dfrac{D_O^{ZrO_2}\left.\dfrac{\partial \varphi_O}{\partial r}\right|_{I_2}-\widetilde{k}_O(I_2)\left[c_O^{\max}-\widetilde{c}_O\right]}{\varphi_O-g_1\dfrac{\rho_S}{c_M}}, & r_3^{L-1}\dfrac{dr_3}{dt}-r_2^{L-1}\dfrac{dr_2}{dt}\le 0\\ r_2^{L-1}\dfrac{D_O^{ZrO_2}\left.\dfrac{\partial \varphi_O}{\partial r}\right|_{I_2}-\widetilde{k}_O(I_2)\left[c_O^{\max}-\widetilde{c}_O\right]}{\varphi_O-c_O^{\max}\dfrac{\rho_S}{c_M}}, & r_3^{L-1}\dfrac{dr_3}{dt}-r_2^{L-1}\dfrac{dr_2}{dt}>0\end{cases}, \tag{52}$$

where

$$c_O^{\max} = \left[g_1(T) + c_U(B) g_2(T)\right]. \tag{53}$$

The two stages can be separated by parameter

$$S_{dir} = (P_y^2 - P_y^1)(P_x - P_x^1) - (P_x^2 - P_x^1)(P_y - P_y^1),$$

$$P = (P_x, P_y) = (1 - x_U - \frac{1}{2} x_O, \frac{\sqrt{3}}{2} x_O),$$

$$P^1: \; x_O = \frac{g_1 / c_M + g_2}{1 + g_1 / c_M + g_2}, \; x_U = \frac{1}{1 + g_1 / c_M + g_2}, \qquad P^2: \; x_O = \frac{g_1 / c_M}{1 + g_1 / c_M}, \; x_U = 0,$$

$$P: \; x_O = \frac{Y_O}{Y_O + Y_{UZ}}, \; x_U = \frac{Y_U}{Y_O + Y_{UZ}}, \tag{54}$$

which determines a normal distance in the ternary phase diagram, Fig. II - 1, from the current point determining composition of the melt bulk, to the liquidus line (or more exactly, is equal to the square of a triangle formed by connection of the current point with terminal points of the liquidus line).

In the saturation stage when composition of melt is in the one-phase (Liquid) region of the phase diagram, this value is positive, $S_{dir} > 0$, and Eq. (39) should be used for Y_O, Y_U, Y_{UZ} and Eq. (49) for $\widetilde{c}_{O(U)}$. In the precipitation stage when composition of melt is in the two-phase (Liquid + Solid) region of the phase diagram, $S_{dir} < 0$, and Eqs. (40) and (50) should be used.

The system of Eqs. (36)–(50) completely determines interactions behavior in the both stages and can be analyzed numerically.

2.4. Discussion

During the precipitation stage

$$c_O^{\max} = \left(g_1 + \widetilde{c}_U g_2\right) = \left(g_1 + c_U^* g_2\right) = c_O^* = \widetilde{c}_O, \tag{55}$$

and Eqs. (51)-(52) are significantly simplified due to disappearance of the term $\widetilde{k}_O\left(c_O^{\max} - \widetilde{c}_O\right)$ in these equations.

It is worthwhile to note that such a simplification concerns only explicit Eqs. (51)-(52), whereas flux matching equations Eqs. (36)-(38) (from which Eqs. (51)-(52) are derived) still contain non-vanishing term $\widetilde{k}_O\left[c_O(I_1) - \widetilde{c}_O\right] = \widetilde{k}_O\left[c_O(I_1) - c_O^*\right]$ that describes oxygen flux in the melt. Indeed, it is straightforward to show that

$$c_O(I_1) = \frac{\left[g_1 + c_U^* g_2\right] c_M \rho_O(I_1) - \left[g_1 + c_M g_2\right] c_O^* \rho_U + \left[g_1 + c_M g_2\right] \rho_U \left. \frac{D_O^{UO_2}}{k_O} \frac{\partial \rho_O}{\partial r} \right|_{I_1}}{c_M \rho_O(I_1) - (c_O^* + \left[c_M - c_U^*\right] g_2) \rho_U + \rho_U \left. \frac{D_O^{UO_2}}{k_O} \frac{\partial \rho_O}{\partial r} \right|_{I_1}}, \tag{56}$$

which is generally not equal to $\widetilde{c}_O = c_O^* = \left(g_1 + c_U^* g_2\right)$ during precipitation stage. Therefore, the non-zero oxygen flux from UO_2 into the melt is sustained also during precipitation stage that results in precipitation of the ceramic $(U,Zr)O_{2-x}$ phase in the oversaturated melt, in correspondence with simplified consideration of the dissolution process in [7,8].

Composition of the melt at the interface with the oxide layer is also not equal to $\widetilde{c}_O = c_O^* = \left(g_1 + c_U^* g_2\right)$, if dissolution of this layer takes place:

$$c_O(I_2) = \frac{\left[g_1 + c_U(B) g_2\right] c_M \rho_O(I) - g_1 c_O(B) \rho_U - \rho_U g_1 \dfrac{D_O^{ZrO_2}}{k_O} \dfrac{\partial \varphi_O}{\partial r}\Big|_{I_2}}{c_M \rho_O(I) - (c_O(B) - c_U(B) g_2)\rho_U - \rho_U \dfrac{D_O^{ZrO_2}}{k_O} \dfrac{\partial \varphi_O}{\partial r}\Big|_{I_2}}, \quad r_3^{L-1} \frac{dr_3}{dt} - r_2^{L-1} \frac{dr_2}{dt} \le 0$$

however, coincides with the melt bulk concentration in the case of oxide layer growth during precipitation stage:

$$c_O(I_2) = \left[g_1 + c_U(B) g_2\right], \quad r_3^{L-1} \frac{dr_3}{dt} - r_2^{L-1} \frac{dr_2}{dt} > 0 .$$

Correspondingly, U composition of growing oxide layer smoothly varies in the course of this layer growth.

2.5. Numerical model

As above explained, the model can be formulated using mass balances, Eqs. (36)-(38), and explicit equations for geometrical variations of solid layers, Eqs. (51)-(53), instead of flux matches. Finally, the complete system of equations for the case of cylindrical geometry to be numerically solved takes the form:

$$\frac{1}{2}\frac{d}{dt}\left[Y_O\right] = -D_O^{UO_2} \frac{\partial \rho_O}{\partial r}\Big|_{I_1} r_1 - \rho_O(I_1) r_1 \frac{dr_1}{dt} + D_O^{ZrO_2} \frac{\partial \varphi_o}{\partial r}\Big|_{I_2} r_2 - \varphi_O \frac{dS}{dt}, \tag{57}$$

$$\frac{1}{2}\frac{d}{dt}\left[Y_U\right] = -\rho_S r_1 \frac{dr_1}{dt} - \widetilde{\rho}_U(I_2)\frac{dS}{dt}, \tag{58}$$

$$\frac{d}{dt}\left[Y_{UZ}\right] = -2\rho_S\left[r_1 \frac{dr_1}{dt} + \frac{dS}{dt}\right], \tag{59}$$

$$\frac{d}{dt}\left[Y_F\right] = -2\widetilde{\rho}_U(I_2)\frac{dS}{dt}, \tag{60}$$

$$\frac{dr_1}{dt} = \frac{-D_O^{UO_2}\dfrac{\partial \rho_O}{\partial r}\Big|_{I_1} - \widetilde{k}_O(I_1)\left[c_O^{\max} - \widetilde{c}_O\right]}{\rho_O - (g_1 + c_m g_2)\dfrac{\rho_U}{c_M}}, \tag{61}$$

$$\frac{dS}{dt} = r_2 \frac{D_O^{ZrO_2} \left.\frac{\partial \varphi_O}{\partial r}\right|_{I_2} - \widetilde{k}_O(I_2)\left[c_O^{\max} - \widetilde{c}_O\right]}{\varphi_O - G_S \frac{\rho_S}{c_M}} \quad , \tag{62}$$

where $S = r_3^2 - r_2^2$; $G_S = \begin{cases} g_1, & dS/dt \geq 0 \\ c_O^{\max}, & dS/dt < 0 \end{cases}$; $Y_F = \varphi_U S$ and fuel layer growth is forbidden in the equation system, i.e. $dr_1/dt = 0$, if $dr_1/dt > 0$. Variable Y_F in Eq. (60) represents an average molar content of uranium in initially pure zirconia layer. In reality uranium is confined within adjacent to the melt intermediate layer with variable mixed composition $(U,Zr)O_{2-x}$, as explained in section 2.1 of the report. The averaging procedure applied in the model allows avoiding introduction of such an intermediate layer and simplifies handling of the layer structure for the cases of complicated temperature transients.

Diffusion fluxes entering Eqs. (57), (61) and (62) have to be determined by the solution of partial derivative oxygen diffusion equations in relative solid layers with moving boundaries (detailed description see, e.g., in [1,2]).

The system of differential equations, Eqs. (1)-(6), is effectively solved by the explicit Euler method with variable time step providing required accuracy.

3. Main results of new RIAR experiments

Main conclusions from temperature measurements in the second series of RIAR tests on simultaneous dissolution of UO_2 crucible and ZrO_2 cylinder presented in Part I of this Report can be briefly formulated as follows:

- temperature gradient in crucible walls was not really large (as assumed in the first test series) and practically disappeared within first ~ 100 s of annealing stage (either in the tests with isolating coverplate or without);
- pyrometer data are not reliable and should be removed from consideration;
- surface thermocouple data fairly determine temperature conditions of melt in both (1^{st} and 2^{nd}) test series;
- therefore, results of the first test series should be reconsidered as conducted at higher temperatures than ascribed before (by pyrometer).

These conclusions can be derived from comparison of temperature measurements by two thermocouples (surface and “deep”) and pyrometer in tests with and without insulating coverplates (over the crucible) presented in Fig. II - 5 and Fig. II - 6, respectively.

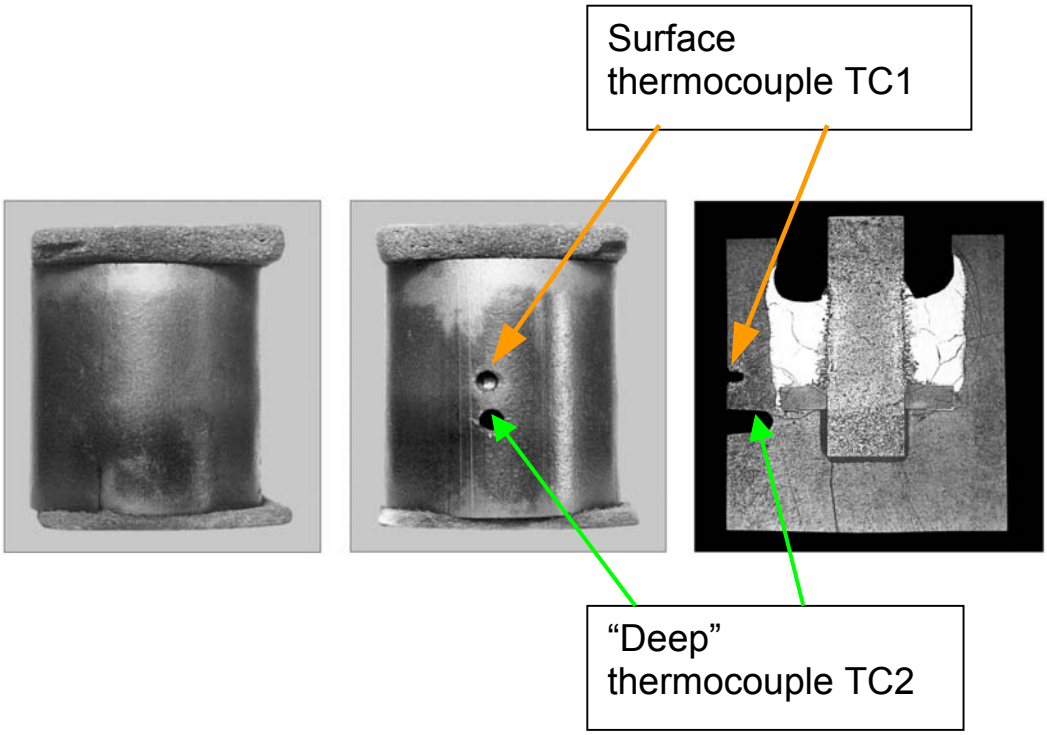

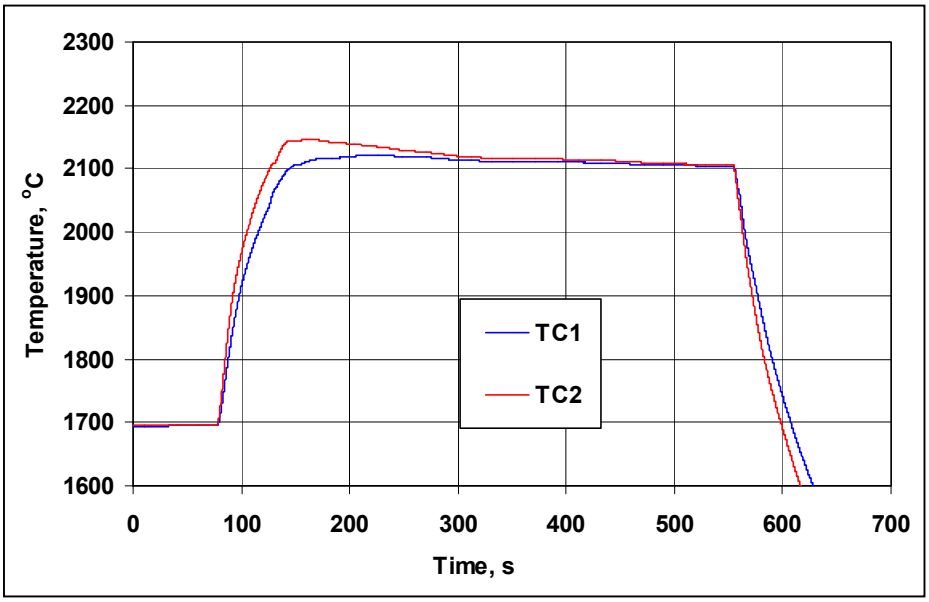

Fig. II - 5. Results of RIAR tests with "deep" thermocouple and with coverplate (2^{nd} test series, T=2100 ^{0}C, t=400 s)

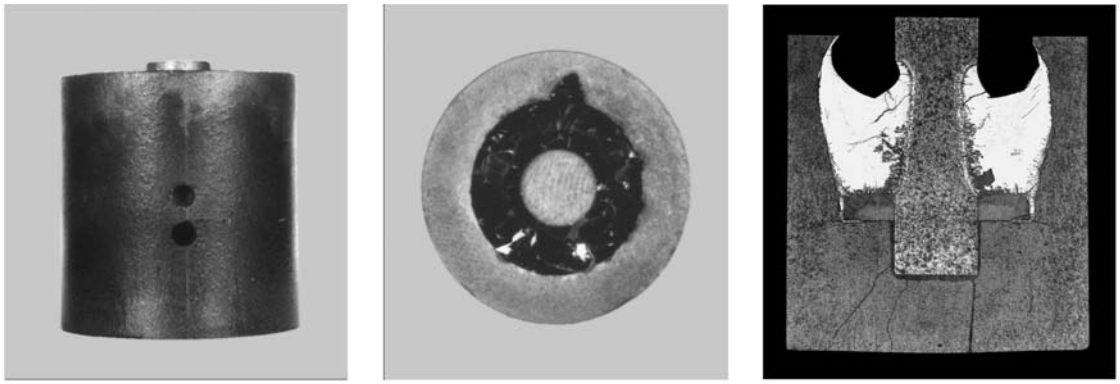

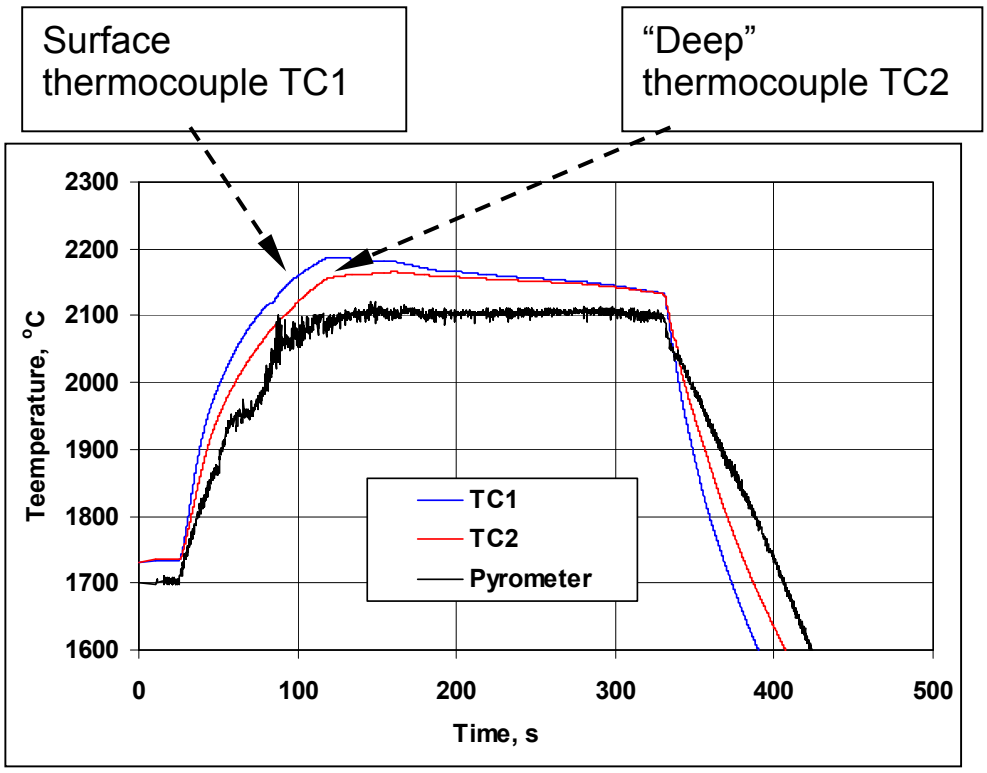

Fig. II - 6. Results of RIAR test with “deep” thermocouple and without coverplate (2nd test series, T=2100 ^{0}C, t=200 s)

4. Simulation of RIAR tests

4.1. Adjustment of model parameters

Before starting simulation of RIAR tests, a preliminary procedure of the main model parameters tuning was performed. For this purpose, the model was validated against previous AECL test series on UO_2 crucible wall dissolution by molten Zry [9]. In this test series either pure or pre-oxidised (with 25 at.% of oxygen) Zry charge were used at the same test temperatures 2100 and 2200°C. This allows to fix unambiguously model parameters g_1 and g_2 determining position of the liquidus line at the test temperatures. Results of such fitting are presented in Fig. II - 7. In all subsequent calculations of the RIAR tests these fitted parameters will be fixed and invariable.

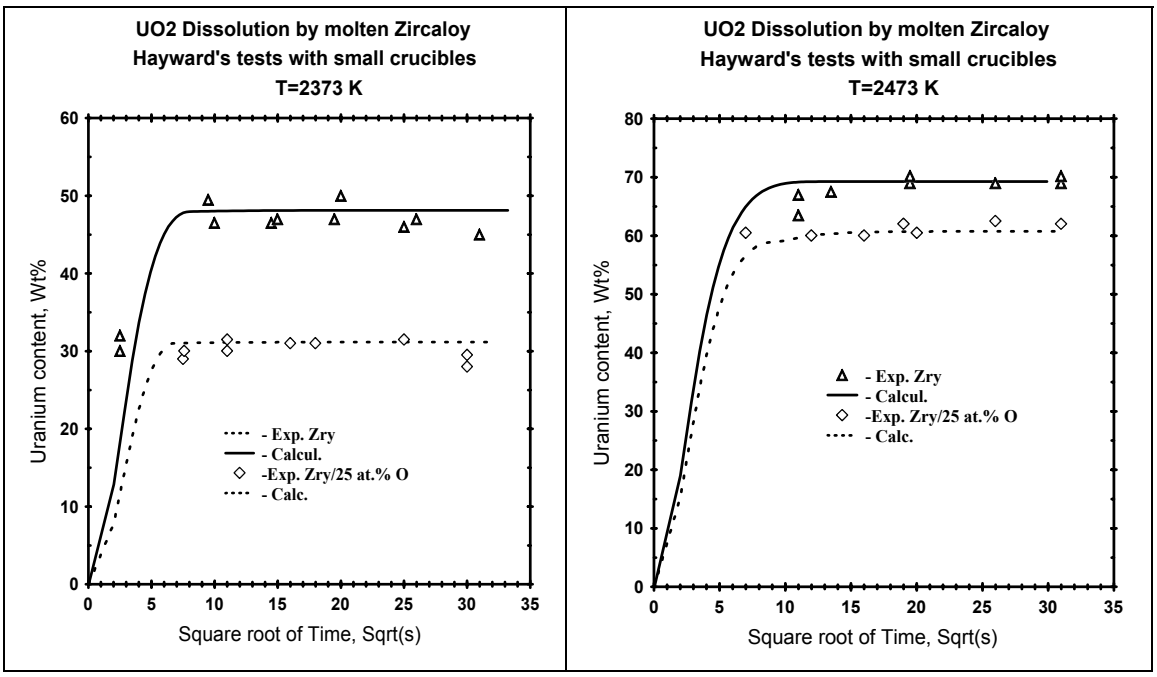

Fig. II - 7. Uranium weight content in the melt in the two tests at 2373K and 2473K with pure and pre-oxidised Zry charges [9]

4.2. Simulation of the 2nd test series (crucibles with isolating coverplates)

The second series of RIAR tests performed with isolating coverplates, consists of three tests: two tests at 2100°C with duration 200 and 400 s, and one test at 2200°C with duration 180 s. The uranium weight content in the melt was measured along with image analysis of dissolved volumes of UO_2 and ZrO_2 materials. As demonstrated in Part I, these results are in a fair consistence with each other, i.e. uranium weight content recalculated from dissolved UO_2 and ZrO_2 volumes satisfactory fits to the directly measured value. This allows an advanced validation of the model by comparison of calculated dissolution rates with measured ones independently for each solid material.

Results of simulation of the 2nd series of RIAR tests are presented in Fig. II - 8 and Fig. II - 9.

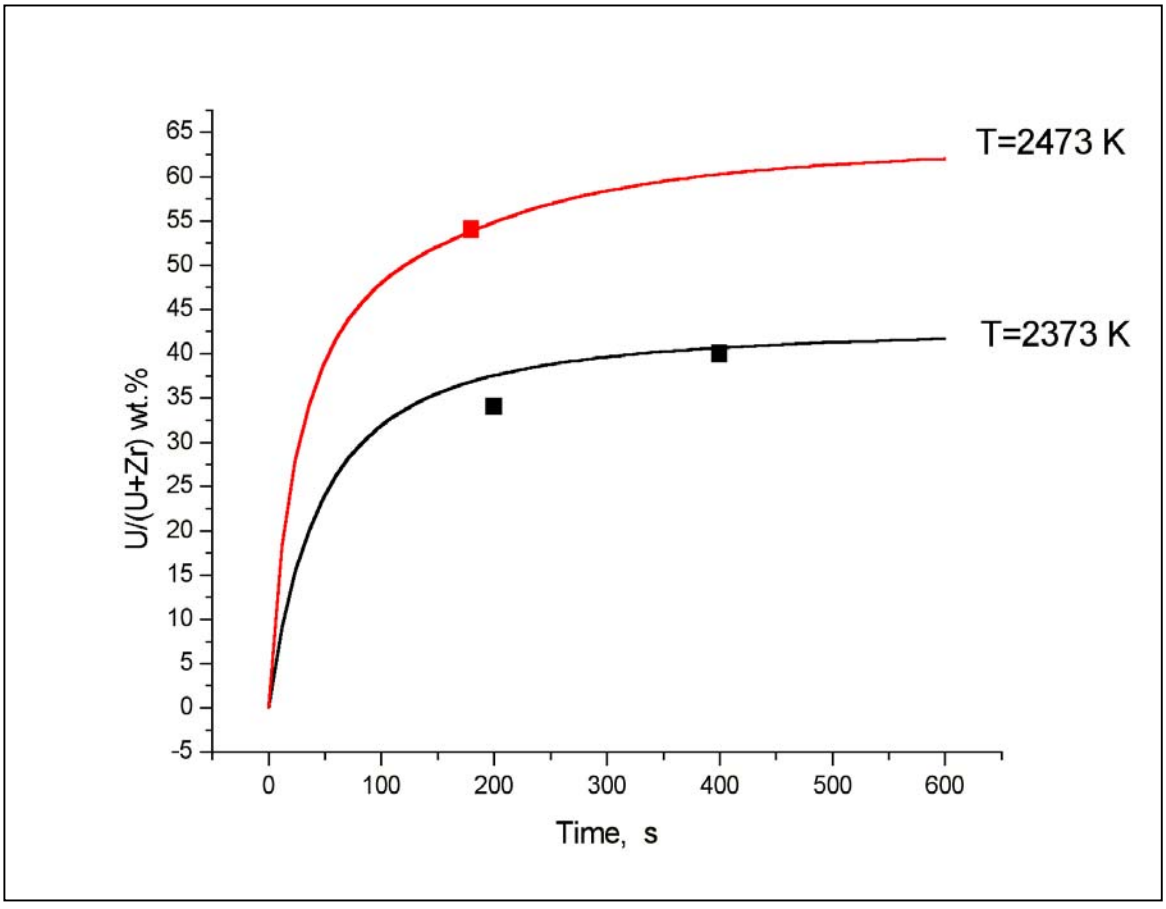

Fig. II - 8. Comparison of calculated and measured uranium weight content in the melt in the 2nd series of RIAR tests performed at 2100 and 2200°C

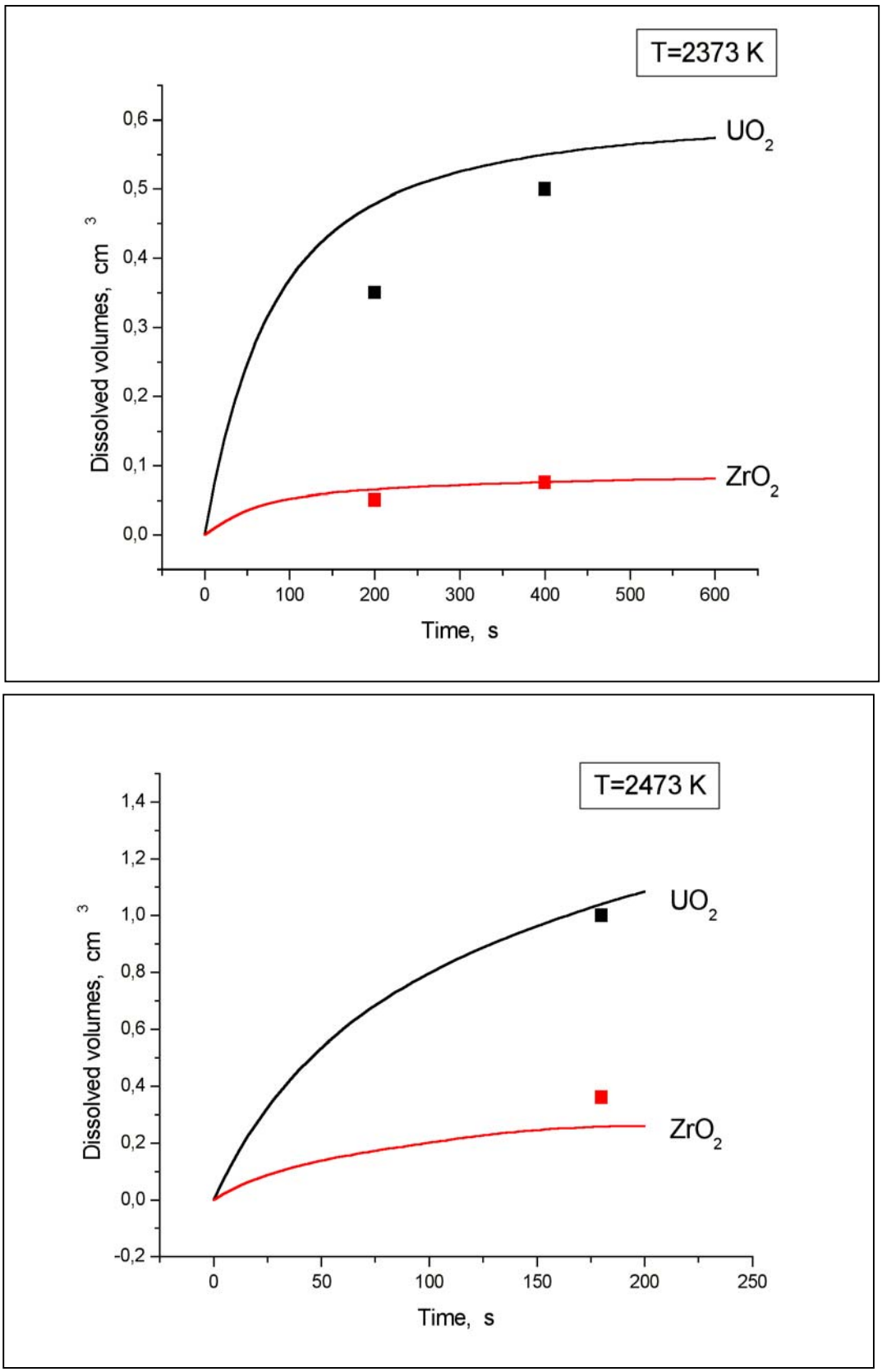

Fig. II - 9. Comparison of calculated and measured dissolved volumes of UO_2 and ZrO_2 in the melt in the 2nd series of RIAR tests performed at 2100 and 2200°C

4.3. Simulation of the 1st test series (crucibles without isolating coverplates)

On the base of above presented (in section 3) conclusions from the new test observations, re-interpretation of test conditions in the 1st test series has been done. Namely, it was assumed that the surface thermocouple data rather than pyrometer ones determine temperature of the melt during annealing. This results in a significant shift for the test temperature in the range 50-100 K (from test to test) in comparison with the temperatures initially ascribed from pyrometer data. Therefore, simulation of the 1st series of RIAR tests (conducted without coverplates) was carried out for temperature conditions determined by surface thermocouples. Results of these calculations performed with the same set of model parameters as in simulation of the 2nd test series, are in a reasonable agreement with measurements, Fig. II - 10.

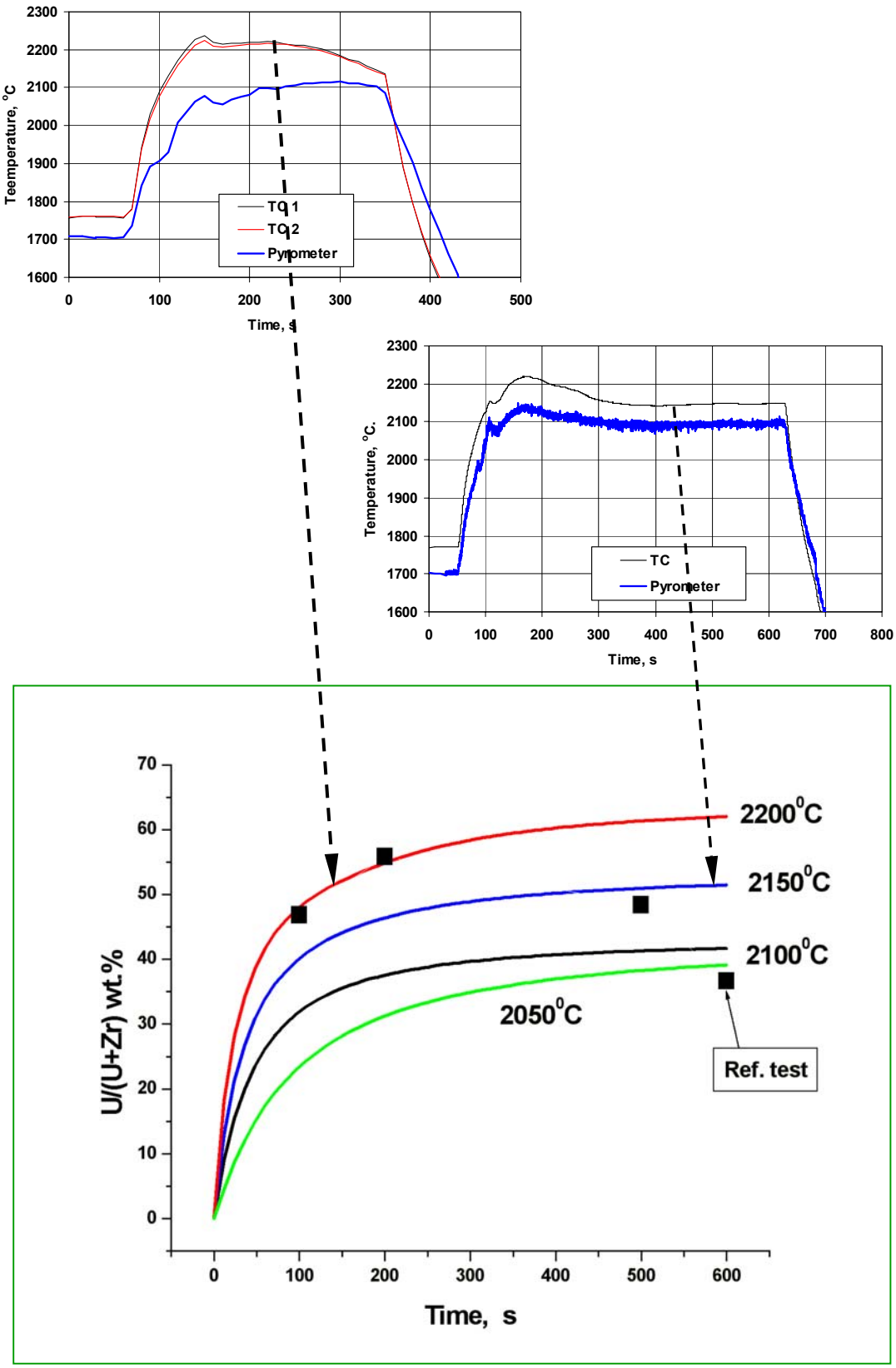

Fig. II - 10. Comparison of calculated and measured uranium weight content in the melt in the 1st series of RIAR tests performed at 2100 and 2200°C

5. Modelling conclusions

- On the base of the previously developed (within CIT Project, 4th FP) models for separate dissolution of UO_2 and ZrO_2 by molten Zr, a new model for simultaneous dissolution of these materials was developed in the SVECHA code. The updated version of the numerical model is formulated in the current report. The model considers interactions of solid materials with convectively stirred melt during the two stages: saturation and precipitation. The system of equations includes mass balances for three components (U,Zr,O) and flux matches at two solid/melt interfaces.
- The model was used for pre-test calculations and analytical support of the RIAR tests. A set of modellers' recommendations for test design and conduction (e.g. additional tests with insulating coverplate and "deep" thermocouples) was realised by RIAR experimentalists in the second test series.
- Results of the second test series (either uranium melt content or dissolved volumes of solid UO_2 and ZrO_2 materials) were self-consistently simulated by the new model without tuning of model parameters.
- Analysis of temperature measurements by "deep" thermocouples allowed re-interpretation of test conditions in the first test series. Recalculation of the first test series with corrected melt temperatures resulted in a satisfactory agreement with measured dissolution kinetics.
- Being implemented in the SVECHA code, the model was also used for further validation against AEKI (Atomic Energy Research Institute, Hungary) tests in a more prototypic fuel rod geometry [10] and is foreseen for further implementation in the SA codes such as ICARE2.

References

1. P.J. Hayward, P. Hofmann, J. Stuckert, M.S. Veshchunov, A.V. Berdyshev, "UO_2 Dissolution by Molten Zircaloy. New Experimental Results and Modelling", Wissenschaftliche Berichte FZKA 6379, INV-CIT(99)-P029, Karlsruhe, Germany, 1999.
2. M.S. Veshchunov, A.V. Berdyshev, "Modeling of chemical interactions of fuel rod materials at high temperatures. Part 1: Simultaneous dissolution of UO_2 and ZrO_2 by molten Zircaloy in an oxidizing atmosphere", J. Nucl. Mater. 252 (1997) 98-109.
3. D.R. Olander, Nucl. Eng. Des. 148 (1994) 253.
4. P. Hofmann, J. Stuckert, A. Miassoedov, M.S. Veshchunov, A.V. Berdyshev, A.V. Boldyrev, "ZrO_2 Dissolution by Molten Zircaloy and Cladding Oxide Shell Failure. New Experimental Results and Modelling", Wissenschaftliche Berichte FZKA 6383, INV-CIT(98)-P026, Karlsruhe, Germany, 1999.
5. K.T.Kim and D.R.Olander, J.Nucl.Mater. 154 (1988) 85, 102.
6. B. Adroguer et al., "Corium Interactions and Thermochemistry (CIT)", FISA 99, EU Research in Reactor Safety, Luxembourg, November 29 – December 1st, 1999.
7. M.S. Veshchunov and P. Hofmann, J. Nucl. Mater. 209 (1994) 27.
8. M.S. Veshchunov, P. Hofmann, A.V. Berdyshev, "Critical evaluation of UO_2 dissolution by molten Zircaloy in different crucible tests", - J. Nucl. Mater. 231 (1996) 1-19.
9. P.J. Hayward and I.M. George, "Dissolution of ZrO_2 in Molten Zry-4", J. Nucl. Mater. 265 (1999) 69.
10. A.V. Berdyshev, A.V. Boldyrev, M.S. Veshchunov, ICARE/COLOSS-IBRAE Final Report, NSI–SARR–150–03, February 2003.